Electromagnetically Induced Transparency in Terahertz Metamaterials and Planar Plasmonic Waveguide Structures

by

Koijam Monika Devi

A thesis submitted
in Partial Fulfillment of the Requirements
for the Degree of

DOCTOR OF PHILOSOPHY.

Department of Physics
Indian Institute of Technology Guwahati
Guwahati 781039, India.

March 2019


भारतीय प्रौद्योगिकी संस्थान गुवाहाटी
Indian Institute of Technology Guwahati

Electromagnetically Induced Transparency in Terahertz Metamaterials and Planar Plasmonic Waveguide Structures

by

Koijam Monika Devi
146121002

A thesis submitted
in Partial Fulfillment of the Requirements
for the Degree of

DOCTOR OF PHILOSOPHY.

Supervisors
Prof. Amarendra Kumar Sarma
Dr. Gagan Kumar

Department of Physics
Indian Institute of Technology Guwahati
Guwahati 781039, India.

March 2019

CERTIFICATE

It is certified that the work contained in the thesis entitled "*Electromagnetically induced transparency in terahertz metamaterials and planar plasmonic waveguide structures*" by Ms. Koijam Monika Devi, a student of the Department of Physics, IIT Guwahati was carried out under our supervision and has not been submitted elsewhere for award of any degree.

Prof. Amarendra Kumar Sarma,
Department of Physics, IIT Guwahati,
Guwahati-781039, Assam, India.
DATE: ....

Dr. Gagan Kumar,
Department of Physics, IIT Guwahati,
Guwahati-781039, Assam, India.
DATE: ....

Dedicated to my beloved parents

Koijam Nabakumar Singh

and

Koijam Kunje Devi

ACKNOWLEDGMENTS

First and foremost, I would like to express my sincere gratitude towards my Ph.D. supervisors, Prof. Amarendra Kumar Sarma and Dr. Gagan Kumar for giving me the opportunity to carry out research under their guidance. Their doors were always open for discussions and their valuable feedbacks helped me understand many things in a better way. Their words of encouragement and their unwavering faith in me has always been a source of motivation for me to work hard. Their enthusiasm and outlook towards research and in life, has always inspired me a great deal to consider every difficulty as an opportunity to learn and to grow as a researcher. I am grateful to both of them for their patience and their consistent support throughout the course of my PhD years.

My sincere gratitude also goes to our collaborator, Dr. Dibakar Roy Chowdhury for all his engaging discussions and immense support regarding my research work. His useful suggestions and insightful comments has also helped me improve my understanding of the field. His words of encouragement has played a great part in motivating me to work harder.

I would like to express my gratitude towards my Doctoral Committee Members, Prof. Pravat Kumar Giri, Dr. Tarak Nath Dey and Dr. Dipankar Bandyopadhyay for their valuable inputs and insightful comments which helped improve the quality of my research work.

I am also thankful to the current and the former Heads of the department of Physics, Prof. Subhradip Ghosh, Prof. P. Poulose and Prof. Saurabh Basu, for providing all the resources needed for my research, and also all other faculty members of the department, the technical stuff and office members, who provided me help whenever I needed. Without their support it would not have been possible to conduct my research.

I would like to thank my groupmates: Maidul, Subhodeep, Jagan, Jyoti, Rakesh, Dipti, Abdel, Dhriti and Angana for the stimulating discussions and for creating a great working environment. I would also like to thank all my 2014 batchmates, seniors and juniors in the department for their company and help in any direct or indirect ways.

I would like to thank all the inspiring people who have motivated me in one way or another in my life. I am thankful to my best friend and my confidant, Kshetrimayum Thoi, for being my greatest emotional support and for always being there for me throughout my journey. I am thankful to my friends: Priti, Sunayana, Sasmita, Eshita Di, Priyadarshini for being their constant moral support throughout my PhD years. My sincere thanks also goes to my cousin Dr. Bijaya and my brother-in-law Dr. Mohan for always being there for me and for being my home away from home during my studies in Hyderabad. I would also like to thank all my teachers, who have inspired me in any direct and indirect ways throughout my life, which has led me towards pursuing science as a career.

Last, but not the least, I would like to express heartfelt gratitude to my family for their role in my life. My parents have always been a source of inspiration to me. Their discipline and values have molded me to the person that I am today. Their unconditional love, support and faith in me are the most precious gifts that I cherish. I am thankful to my younger siblings, Benao and Naoba, for always being my moral support and for always being there for me throughout my life.

LIST OF PUBLICATIONS

Journal Publications

1. **K. Monika Devi**, Amarendra K. Sarma, D. R. Chowdhury, and Gagan Kumar, "Plasmon induced transparency effect through alternately coupled resonators in terahertz metamaterial," *Opt. Express*, **25**(9), 10484-10493, 2017.

2. **K. Monika Devi**, M. Islam, D. R. Chowdhury, Amarendra K. Sarma, and Gagan Kumar, "Plasmon-induced transparency in graphene-based terahertz metamaterials,"*EPL*, **120**(2), 27005, 2018.

3. **K. Monika Devi**, D. R. Chowdhury, Gagan Kumar, and Amarendra K. Sarma, "Dual-band electromagnetically induced transparency effect in a concentrically coupled asymmetric terahertz metamaterial," *J. Appl. Phys.*, **124**(6), 063106, 2018.

4. **K. Monika Devi**, K. Porsezian, and Amaremdra K. Sarma, "Surface plasmon polariton Akhmediev Breather in a dielectric-metal-dielectric geometry with subwavelength thickness," *Superlattices and Microstructures*, **117**, 392-398, 2018.

5. **K. Monika Devi**, Gagan Kumar, and Amarendra K. Sarma, "Surface polaritonic solitons and breathers in a planar plasmonic waveguide structure via electromagnetically induced transparency", *J. Opt. Soc. Am. B*, **36**(8), 2160-2166, 2019.

6. Rakesh Sarkar, **K. Monika Devi**, Dipa Ghindani, Ravikumar Jain, Arnab Pattanayak, S. S. Prabhu, Dibakar Roy Chowdhury, and Gagan Kumar, "Polarization independent dual-band electromagnetically induced transparency effect in terahertz metamaterials", (*under review*).

7. Angana Bhattacharyaa, **K. Monika Devi**, Tho Nguyen, Gagan Kumar, "Actively tunable toroidal excitations in graphene based terahertz metamaterials", (*under review*).

8. Rakesh Sarkar, Dipa Gindhani, **K. Monika Devi**, Shriganesh Prabhu and Gagan Kumar, "Independently tunable dual-band electromagnetically induced transparency in planar terahertz metamaterials", (*submitted*).


भारतीय प्रौद्योगिकी संस्थान गुवाहाटी
Indian Institute of Technology Guwahati

LIST OF PUBLICATIONS

Conference Proceedings

1. **K. Monika Devi**, Amarendra K. Sarma, and Gagan Kumar, "Enhanced terahertz transmission through a periodic array of tapered rectangular apertures", *Journal of Physics: Conference Series (IOP)* **759**(1), 012052, (2016).

2. **Koijam Monika Devi**, Gagan Kumar, and Amarendra K. Sarma, "Surface Plasmon Polariton Akhmediev Breather in a dielectric-metal-dielectric multilayer structure," in 13th International Conference on Fiber Optics and Photonics, *OSA Technical Digest* (online) (Optical Society of America, 2016), pp W3A-29.

3. **Koijam Monika Devi**, M. Islam, D. R. Chowdhury, Amarendra K. Sarma, and Gagan Kumar, "Exploring Plasmon Induced Transparency in Graphene Based Terahertz Metamaterials", *IEEE Workshop on Recent Advances in Photonics (WRAP)*,pp 1-3, (2017), IEEE.

ABSTRACT

The concept of attaining a controlled optical response of a material lies at the core of many of the advances in the field of optics. In the subwavelength regime, an effective control of the interaction between light and matter has become possible with the advent of metamaterials (MMs) and plasmonics. Over the years, MMs and plasmonics have revolutionized the entire field of optics and photonics by challenging well-established technological restrictions such as the diffraction limit of light. Recently, MMs and plasmonic structures have been used to explore quantum phenomenon such as electromagnetically induced transparency (EIT), in which a medium opaque to a resonant field is rendered transparent by applying another field of similar resonant frequency. In this thesis, we explore the different aspects of the EIT phenomenon such as: tunable transparency window, steep dispersion and enhanced nonlinearity in the context of terahertz MMs and planar plasmonic waveguide structures. The thesis is divided into two parts. In the first part, we discuss the analogue of the quantum EIT phenomenon in terahertz MMs. Here, we propose a terahertz MM geometry comprising an array of two C shaped resonators placed alternately on both sides of a metal strip exhibiting the plasmon induced transparency (PIT) effect. We have further examined a polarization independent PIT response for two orthogonal direction of incident polarization in a symmetric MM structure comprising of an array of a cross structure and four C shaped resonators. Next, the modulation of the PIT effect is explored in a graphene based terahertz MM by varying the vertical and horizontal distances between the resonators. The dynamic tuning capability of the PIT effect is also examined by varying the Fermi energy of the graphene layer. Further, dual-band EIT effect is examined in a concentrically coupled asymmetric terahertz MM structure in which two tunable transparency windows are achieved. In the second part, the excitation and propagation of surface polaritonic solitons and breathers in a planar plasmonic waveguide structure via the quantum EIT effect is discussed. Our study has significant potential in the realization of devices for polarization

independent broadband applications, dynamically tunable devices, slow light systems, narrowband absorbers, highly compact ultrafast optical devices, and many more.

TABLE OF CONTENTS

LIST OF FIGURES

CHAPTER 1

INTRODUCTION

The notion of controlling the optical response of a material has always intrigued the scientific community. Advances in the field of optics have led to the development of various ways for achieving a controlled optical response of materials in the subwavelength regime. In modern technology, the ability to effectively control and manipulate light confined to small length scales serves a multitude of applications [1–7]. However, a fundamental incompatibility exists in controlling light of microscale wavelength with photonic structures of nanoscale dimension. In fact, the light-matter interactions are significantly diminished when the dimension of a structure is much smaller than the dimension of the guided wavelength [7, 8]. The advent of metamaterials (MMs) and plasmonics challenged these well-established technological restrictions and revolutionized the entire field of optics and photonics by offering the possibility of effectively controlling the light-matter interaction in the subwavelength scale [9–12].

MMs are broadly defined as artificially engineered materials [9, 10], having unusual optical properties not readily available in naturally occurring materials [13, 14]. MMs usually comprises of an array of artificial atoms (meta-atoms or meta-molecules) of subwavelength dimension. These artificial structures gain their electrical properties from the shape, dimension and arrangements of the meta-atoms rather than the bulk material comprising the structure [15, 16]. MMs, thus provide the flexibility of controlling the permittivity and permeability by merely altering the structure of the meta-atoms.

The early concept of MM was pioneered by the Russian physicist Victor Veselago, in 1967 with the idea of negative refractive index [17]. In his paper, Veselago hypothesized the existence of a material with simultaneously negative values of electric permittivity, ϵ and magnetic permeability, μ. However, the existence of materials with negative permittivity and permeability was considered impossible for a long time. It was only in 2000, that Pendry proposed the recipe for obtaining negative refractive index by constructing a subwavelength structure comprising of split ring resonators (SRRs) [18]. It was followed by experiments by Smith and coworkers [19, 20], in which they demonstrated the possibility of fabricating an artificial material whose electromagnetic characteristics can be described by a negative index of refraction. In addition to the SRRs, other subwavelength periodic structures such as photonic crystals [21], nano-strips, nano-rods, nano-rings [22–26], have also been examined for the realization of applications in diverse areas including super-lensing [18, 27, 28], optical cloaking [15, 29, 30], sensing [31–33], high-temperature superconductors [34–36], etc.

Apart from MMs, plasmonic structures have also been implemented for the modulation of light beyond the diffraction limit [1, 11]. Plasmonics deal with surface plasmon polaritons (SPPs) and its applications [12]. SPPs are electromagnetic surface modes that propagate at the interface of a conductor and a dielectric. These surface modes enable effective localization of light over subwavelength dimensions and allow an efficient control of light [12, 37]. Numerous experimental and theoretical studies investigating the importance of SPPs in various structures such as metal-dielectric interface [37], metal with corrugations or holes [38–42], hybrid planar waveguides [43–45] and planar waveguide structures [46–48] have been performed. These structures enable the tight confinement of light and allow advanced control and manipulation of light in miniaturized photonic circuits [49]. Recently, plasmonic waveguide structures have been studied to explore the nonlinear behavior of the surface electromagnetic waves by incorporating a nonlinear medium in the structure [50]. The study of such nonlinear plasmonic structure revealed the possibility of a myriad of interesting phenomena such as modulation instability [51–53], generation of plasmon-soliton [54–57], etc. Consequently, MMs and plasmonic structures have managed to attract significant interest owing to its potential in developing highly miniaturized photonic devices. These devices have practical applications in various disciplines of science and technology such as imaging [58–61], sensing [62–64], solar cells [65–68], SPP amplifiers and lasers [69–72], etc.

Over the past decade, MMs and plasmonic structures have been associated with a quantum phenomenon called electromagnetically induced transparency (EIT). MMs have been found to mimic EIT in the classical regime [73, 74], through careful arrangements of the structures. In EIT, a medium opaque to a resonant field is rendered transparent by applying another field of similar resonant frequency [75]. In the context of plasmonic structures, the quantum EIT phenomenon has been recently implemented to investigate the excitation of surface plasmon (SP) resonances in these structures [76–78]. EIT was first proposed by Harris et al. [79] in the year 1989, followed by experimental demonstrations by Boller et al. [80] in Strontium vapor and by Field et al. [81] in lead vapor, in 1991. Other studies of modified dispersive properties of EIT in Rubidium and Sodium atoms has also been investigated [82, 83]. The essence of EIT phenomenon is the modified refractive index of the medium that comes along with a low absorption and a steep dispersion within the transparency region. It should also be emphasized that the nonlinear optical response of the medium is greatly enhanced within the transparency region [84]. Numerous interesting studies have been performed to realize a wide range of phenomenon such as highly efficient nonlinear mixing [85–87], slow light phenomenon [88–91] and lasing without inversion [92, 93].

The unification of MMs and plasmonic structures with the EIT effect opened up a new area of research that remains to be explored and understood. The study of EIT phenomenon in MMs and plasmonic structures is driven by the many fascinating aspects of the effect. Firstly, the occurrence of a steep dispersion within the EIT transparency window leads to a group velocity reduction of the impinging light, thus enabling the tailoring of slow light in different frequency regimes [73, 94]. Secondly, the modified nonlinear response associated with the EIT phenomenon could be exploited to generate nonlinear polaritonic waves in plasmonic structures [95, 96]. It is worthwhile to note that, of late, most studies on EIT in MMs and plasmonic waveguide structures are mainly confined to the linear propagation regime, barring few studies [95–98]. In the nonlinear regime, it is very natural to explore solitonic phenomena, soliton being considered as a kind of nonlinear mode. EIT induced solitons, breathers and rogue waves are expected to find immense applications in optical communication and related devices. Furthermore, in the case of MMs, EIT can be achieved at room temperature unlike EIT in a quantum system where the sample has to be kept in a cryogenic environment throughout the experiment [99]. This makes EIT in MMs favorable when it comes to practical applications. Currently, EIT in MMs and plasmonic structures has seen a rapid surge of interests owing to its abundant prospective applications in the actualization of devices for polarization independent broadband applications [100–104], dynamically tunable devices [105–108], slow light systems [109, 110], sensing applications [111–113], narrowband absorbers [114, 115], highly compact ultrafast optical devices [95], and many more.

1.1 EIT in a three-level atomic system

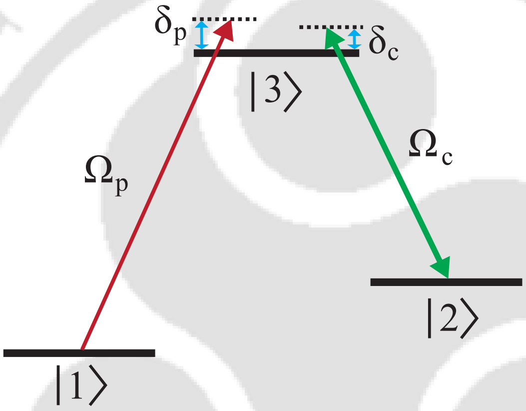

Figure 1.1: Energy level diagram of a three level lambda-type atomic system.

In this section, the underlying physical mechanisms of EIT phenomenon in a quantum system is discussed. The simplest form of atomic system exhibiting the EIT phenomenon is a three-level atomic system [116]. The prototype of a lambda-type atomic system is illustrated in Fig. 1.1. Here, the levels $|1\rangle$, $|2\rangle$ and $|3\rangle$ are the energy levels of the lambda type atomic system, where the transition between the levels $|1\rangle$ and $|3\rangle$ is driven by a weak probe field of angular frequency, ω_p, the transition between the levels $|2\rangle$ and $|3\rangle$ is driven by a strong coupling field of angular frequency, ω_c and the transition between $|1\rangle$ and $|2\rangle$ is forbidden. Then, the density matrix equation of the system can be obtained by using the time-dependent Schrödinger equation of the form

$$\frac{d\,|\psi\rangle}{dt} = (H_0 + V)\,|\psi\rangle \tag{1.1}$$

where $|\psi\rangle = a_1|1\rangle + a_2|2\rangle + a_3|3\rangle$. Since the transitions between $|1\rangle$ and $|2\rangle$ is not allowed, the potential which is given by the expression $V_{ij} = -ex_{ij}.E(t)$, vanishes for V_{12}

or V_{21}.The diagonal matrix element $V_{ii} = 0$. We define $\omega_{ij} = (E_j - E_i)/\hbar$ where the electric field, $E(t) = \frac{1}{2}\hat{\epsilon}_p E_p e^{-i\omega_p t} + \frac{1}{2}\hat{\epsilon}_c E_c e^{-i\omega_c t} + c.c.$. Then, by assuming $\omega_p \approx \omega_{31}$ and $\omega_c \approx \omega_{32}$ and applying the rotating wave approximation, Eq. (1.1) reduces to the form:

$$\frac{da_1}{dt} = i\Omega_p^* e^{i\omega_p t} a_3 \tag{1.2a}$$

$$\frac{da_2}{dt} = -i\omega_{21} a_2 + i\Omega_c^* e^{i\omega_c t} a_3 \tag{1.2b}$$

$$\frac{da_2}{dt} = -i\omega_{31} a_3 + i\Omega_p e^{-i\omega_p t} a_1 + i\Omega_c e^{-i\omega_c t} a_2 \tag{1.2c}$$

where $\Omega_p = \frac{e x_{ij}.\hat{\epsilon}_p E_p}{2\hbar}$ and $\Omega_c = \frac{e x_{ij}.\hat{\epsilon}_c E_c}{2\hbar}$ are the Rabi frequencies of the probe and the coupling field. With the introduction of slowly varying amplitudes of the form: $a_1 = c_1(t)$, $a_2 = c_2(t)e^{-i(\omega_p - \omega_c)t}$, $a_3 = c_3(t)e^{-i\omega_p t}$ and by substituting the amplitudes in Eq. (1.2), we get

$$\frac{dc_1}{dt} = i\Omega_p^* c_3 \tag{1.3a}$$

$$\frac{dc_2}{dt} = -i\delta_p c_2 + i\Omega_c^* c_3 \tag{1.3b}$$

$$\frac{dc_3}{dt} = -i\delta_c c_3 + i\Omega_p c_1 + i\Omega_c c_2 \tag{1.3c}$$

where $\delta_p = \omega_{31} - \omega_p$ and $\delta_c = \omega_{32} - \omega_c$ are frequency detunings of the probe and the coupling field, respectively. Then, the density matrix equation can be derived in a straightforward manner using the relation, $\rho_{ij} = c_i c_j^*$ for $i, j = 1, 2, 3$. For a sufficiently weak probe field, the probability amplitude is assumed to be close to unity i.e., $|c1(t)|^2 \approxeq 1$. Under this assumption, we have the density matrix elements, $\rho_{11}(t) = 1$, $\rho_{23}(t) = \rho_{32}(t) = \rho_{22}(t) = \rho_{33}(t) = 0$. If the damping due to collision and spontaneous emission, described by the relaxation rates γ_{12} and γ_{13} is considered, then Eq. (1.3) reduces to

$$\frac{d\rho_{12}}{dt} = i(\delta_p + i\gamma_{12})\rho_{12} - i\Omega_c \rho_{13} \tag{1.4a}$$

$$\frac{d\rho_{13}}{dt} = i(\delta_c + i\gamma_{13})\rho_3 - i\Omega_p^* - i\Omega_c^* \rho_2 \tag{1.4b}$$

By solving Eq. (1.4) under the steady state condition, one can arrive at the expression for the density matrix element ρ_{13} as follows

$$\rho_{13} = \frac{i\Omega_p^*(\delta_p + i\gamma_{12})}{(\delta_p + i\gamma_{12})(\delta_c + i\gamma_{13}) - |\Omega_c|^2} \tag{1.5}$$

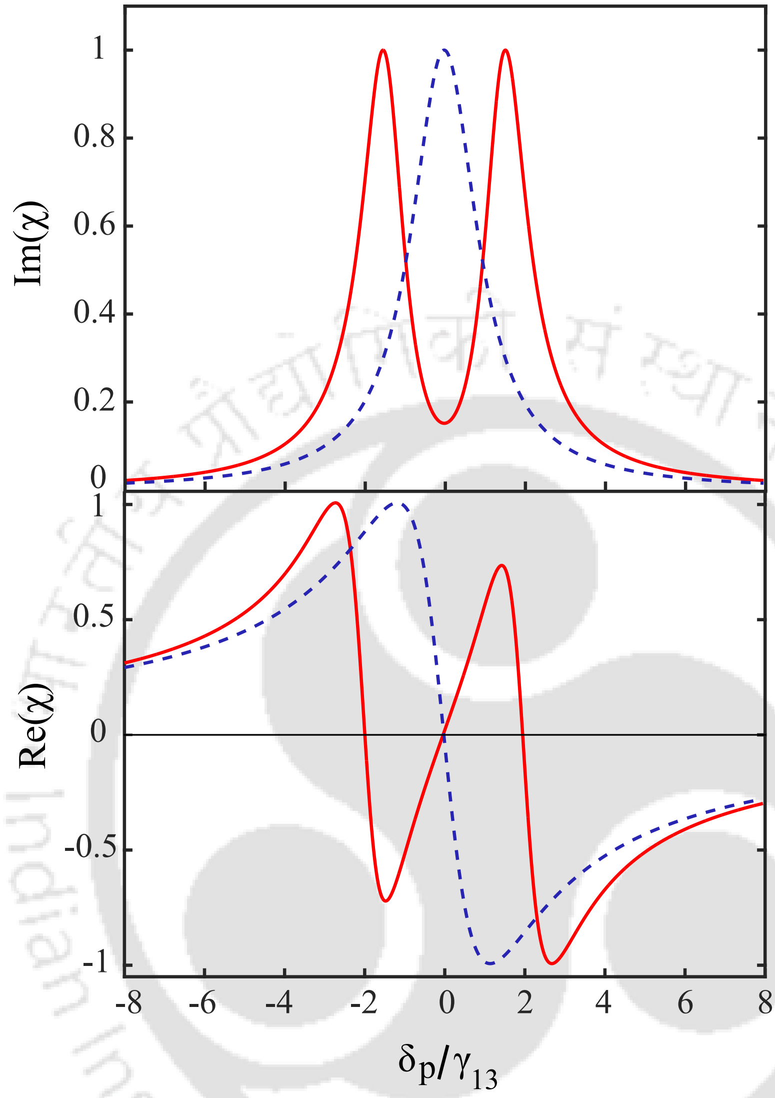

Figure 1.2: Susceptibility, χ as a function of the probe detuning δ_p/γ_{13} for a radiative two-level system (blue dashed line) and an EIT system with resonant coupling field (red solid line).

Using the relation $\chi = \frac{iN|\mu_{13}|^2}{\epsilon_0\hbar}\rho_{13}$, where N is the number density, μ_{13} is the dipole moment, ϵ_0 is the vacuum permittivity, the linear susceptibility of the three-level atomic system is given by the expression:

$$\chi = \frac{iN|\mu_{13}|^2}{\epsilon_0\hbar}\frac{\Omega_p^*(\delta_p + i\gamma_{12})}{(\delta_p + i\gamma_{12})(\delta_c + i\gamma_{13}) - |\Omega_c|^2} \tag{1.6}$$

The important information about the EIT phenomenon can be retrieved by examining the linear susceptibility, given in Eq. (1.6). A more elaborate derivation of the optical parameters can be found in Ref [116]. Figure 1.2 shows the linear susceptibility, χ as a function of the probe detuning δ_p with damping rates γ_{13}. The linear susceptibility describes the optical response of the atomic medium to an incident applied field. The imaginary part of χ (top) characterizes absorption while the real part of χ (bottom) denotes the refractive index of the medium. In the figure, the blue dashed line depicts the susceptibility of a two-level atomic medium. For the two-level atomic medium, the applied weak probe field drives the population transfer between the states of the atomic medium. This medium behaves as a radiative system and exhibits a Lorentzian spectral response. However, with the application of a coupling laser field, the initially radiative system now becomes transparent to the probe field. The modified dispersive response of the system as a result of the EIT phenomenon is represented by the red solid lines in Fig. 1.2. For a detuning $\delta_p = 0$, an elimination of absorption takes place in the system due to the interference between two transition pathways of the three-level atomic medium [79–81]. At the position of minimum absorption, the dispersion is steep, thus giving rise to the slowing of group velocities. As a direct consequence of this aspect, EIT has been associated with slow light phenomena [75, 81, 91], storage of light [88, 89], etc.

In this thesis, the modified optical properties of the EIT effect is exploited in the context of terahertz MMs and planar plasmonic waveguide structure. Different aspects of the EIT effect such as the tunable transparency window, steep dispersion and greatly enhanced Kerr nonlinearity are explored in the terahertz frequency and the optical frequency regimes. In the following sections, we shall briefly discuss the underlying mechanism of EIT phenomenon in terahertz MMs and planar plasmonic waveguide structures.

1.2 EIT in terahertz metamaterials

A terahertz MM is a type of composite MM designed in such a way that it operates and interacts in the terahertz frequency regime. The terahertz regime is a very narrow spectral region of frequencies ranging from 0.1 THz to 10 THz, which falls between the microwave and infrared regions of the electromagnetic spectrum [117]. In the electromagnetic spectrum, a radiation having a frequency of 1 THz corresponds to a time period of 1ps and has a wavelength of 300 μm with a photon energy of 4.1 meV. Terahertz radiation has the potential to penetrate most dry dielectric materials such as clothing,

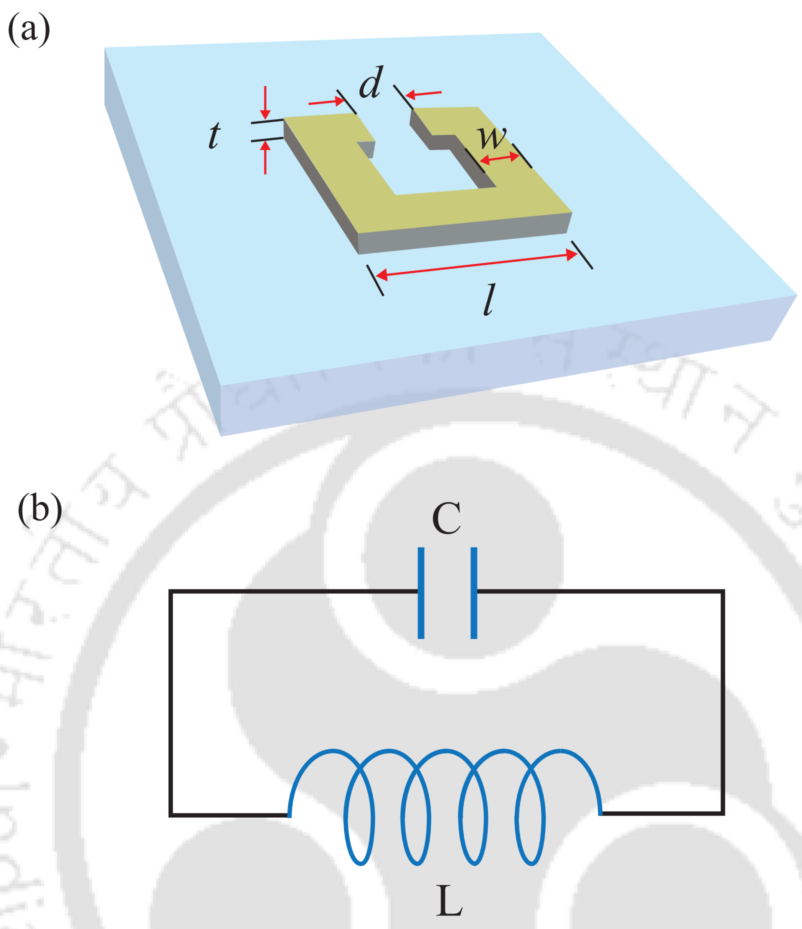

Figure 1.3: (a) A prototype of a single split ring resonator and (b) its equivalent LC circuit [129].

paper, cardboard, plastics, etc. and are non-ionizing in character. Terahertz radiations also have the ability to provide the physical insights of a material that is not accessible by using X-ray or infrared radiation. As a result, terahertz radiation has been explored for its applications and significance in various applied fields such as security purposes [118–120], imaging [121–124], medicine [125, 126], sensing of chemical and biological agents [127, 128].

Until recently, this portion of the electromagnetic spectrum was not particularly useful due to lack of suitable devices that could emit and detect the terahertz signals, since most of the natural materials do not respond to terahertz radiation [117]. In order to overcome this limitation, artificially designed materials have been employed. MMs enable interaction with the terahertz radiation leading to the realization of the many devices and ultimately filling the technological void in this regime. One of the most common MM structure, is the metallic split ring resonator (SRR), shown in Fig. 1.3(a), purposely engineered with subwavelength dimensions to exhibit a resonant response in the terahertz regime [129, 130]. Intuitively, an SRR can be thought of as a metallic ring structure having a purely inductive response to the external field, in which the formation of a complete circular current is prevented with the introduction of a gap in the ring, resulting in the accumulation of charges across the gaps. Then, the SRR finally behaves as a resonant element with both capacitance and inductance, ultimately enhancing the magnetic response of the structure. From an equivalent circuit point of view, an SRR behaves as an LC oscillator in response to an applied external field [130]. According to the simple circuit model, shown in Fig. 1.3(b), the frequency of the magnetic resonance in an SRR, given by the expression $\omega_R = 1/\sqrt{LC}$, can be approximately evaluated through a careful estimation of the equivalent inductance L and capacitance C [129, 130]. The inductance of the conducting ring is given by the expression:

$$L = \frac{\mu_0 l^2}{t} \tag{1.7}$$

while the capacitance of the gap can be obtained using the expression

$$C = \frac{\epsilon_0 w t}{d} \tag{1.8}$$

where μ_0 and ϵ_0 are the magnetic permeability and electric permittivity of free space, respectively. l denotes the length of the SRR side, t is the metal thickness, w is its width and d represents size of the gap. Then, the resonance frequency can be expressed as $\omega_R = 1/\sqrt{d/wl^2} \propto 1/A$, where A is the size of the meta-atom and is directly proportional to all the geometrical parameters i.e., l, t, w, d. Hence, A acts as a scaling factor for the SRR structures. Therefore, the resonance of the SRR can be shifted to higher frequencies by shrinking the dimensions of the structures [130]. In Ref [131], a resonance was achieved at frequencies ranging from 0.8 to 1.2 THz in an array of SRRs made of 3 μm thick copper by scaling the size of the SRRs. These experimental demonstrations further paved the way for exploring metamaterials for various different applications in the terahertz frequency region [130–136].

Following similar scaling rules, various other structures such as cut-wires, circular or square rings, symmetric and asymmetric SRRs, etc. can also be tailored to exhibit resonances at the terahertz frequency regime. With strategic use of a combination of these structures, the EIT effect can be achieved in terahertz MMs. The first analogue of EIT effect was achieved in 2008, by Zhang *et al.,* in a MM structure comprising of cut-wire structures made of silver metal on a dielectric substrate [73]. In their work, this analogue of the EIT effect was termed as plasmon induced transparency (PIT). In the same year, a similar kind of study was carried out by Papasimakis [74] and his coworkers, where they investigated EIT effect in a MM structure whose meta-atom comprises of bi-layered fish-scale structures that are etched in the top and bottom face of a 1.5 mm thick dielectric material. In MMs, the EIT effect usually occurs as a result of interference between the bright and the dark modes. The bright mode strongly couples with the incident light and has a broader spectral response while the dark mode couples weakly or not at all to the incident light [137–139]. For EIT to occur, both the bright and the dark modes should have similar resonant frequencies with a very little deviation. In such a situation, the destructive interference of these modes induces a narrow transparency region in the otherwise absorptive spectrum. Within this region all the incident radiation gets transmitted through the medium and the dispersive properties of the medium gets strongly modified [73].

Since the detection of the EIT effect in 2008, a variety of metamaterial configurations comprising of metal strips, coupled SRRs, slot waveguides have been investigated for the realization of the effect in gigahertz [97, 98], terahertz [99, 103, 140–142] as well as the infrared regime [105, 107] of the electromagnetic spectrum. Numerous experimental demonstration in this area have been supported by the well-defined theories such as equivalent circuit [143, 144] and coupled Lorentz oscillator models [73, 99]. However, for most of the metal based metamaterials, tuning of the EIT effect limited by the scaling constraints of the MM structures. In this context, active tuning of the EIT [97, 99, 106] effect is explored in MMs by incorporating nonlinear media or semiconductor material in the structure. Even so, only limited tuning could be achieved in case of the metal structures. The pursuit for the efficient tuning of the EIT effect led to the study of this effect using graphene based metamaterials. Recently, the dynamic tunabilty of the effect in graphene metamaterials has been rigorously investigated in the mid-infrared [105, 107, 145–149] as well as terahertz frequency regions [150, 151]. MM structures such as metal split ring resonators (SRRs) coupled to a graphene strip [147], Comb like structure [148] as well as dipole-dipole coupling [149], a graphene ring coupled to a graphene strip [152] are some configurations that has been investigated. Considerable interest has also been given to realize dual-band EIT effect in terahertz MMs, in which two transparency windows are induced, through the careful arrangements of the resonators. MM configurations comprising of metal strips, split ring resonators, hybrid structures, [115, 153–155] etc. have been investigated for the realization of this effect. The investigations in this area of research is influenced by its potential in the realization of applications such as slow light devices [94, 109, 156–158], frequency agile devices [99, 105, 150, 159], sensors [111, 112, 143], etc.

1.3 EIT in planar plasmonic waveguide structures

Over the recent years, the quantum EIT phenomenon has also been associated with the generation of surface plasmon (SP) resonances in planar plasmonic waveguide structures [76, 77]. Theoretical studies have suggested the possibility of exciting SP resonances in a prism coupler system with an EIT medium [76]. Excitation of SP resonances has also been examined in an experimentally feasible prism coupler system with the help of EIT in a semiconductor-quantum-dot system [77]. This section gives a brief description of SPs and its excitation by employing the quantum EIT phenomenon in a prism coupler system.

1.3.1 Surface plasmons

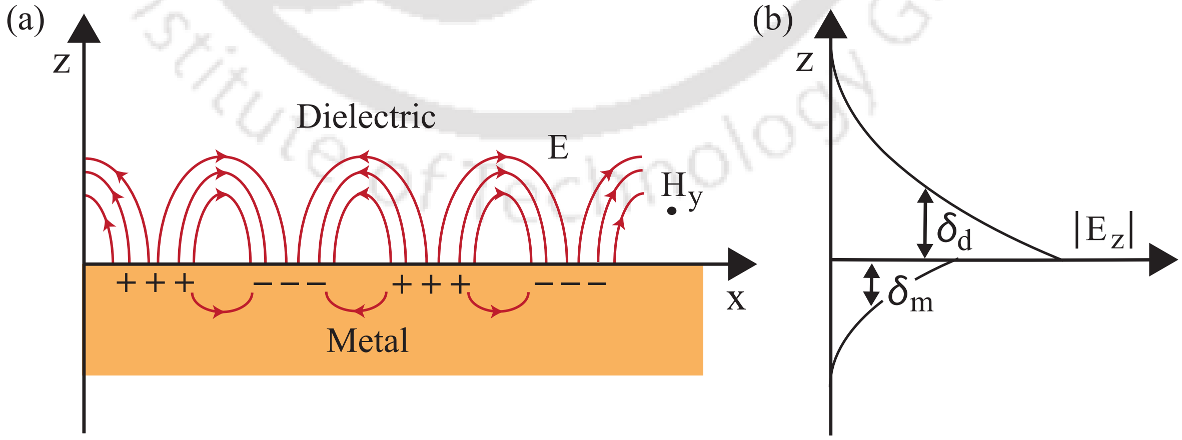

Figure 1.4: Schematic illustration of electromagnetic wave and surface charges at the interface between a conductor and dielectric, (b) the local electric field component is enhanced near the surface and decay exponentially with distance in a direction normal to the interface.

Surface plasmons (SPs) are electromagnetic surface modes that enable effective localization of light over subwavelength dimensions allowing the efficient control of light [12]. These surface waves arise when incident laser fields couple with the collective electron oscillations in the metal. The physical properties of SPs can be investigated by applying the Maxwell's equations to a flat interface between a conductor and a dielectric.

The simplest geometry sustaining SPs is a single, flat interface between a dielectric and an adjacent conducting media (shown in Fig. 1.4). The dielectric is described by a positive real dielectric constant, ϵ_d and the conductor is described by a dielectric function, $\epsilon_m(\omega)$. For an electric field propagating in the x-direction with no spatial variation in the in-plane y-direction, the plane $z = 0$ coincides with the interface. This interface sustains the propagating waves, described as $E(x,y,z) = E(z)e^{i(\beta x-\omega t)}$, where β is the propagation constant of the surface wave and correspond to the component of wave-vector in the direction of propagation. For TM mode, the Maxwell's equation reduces to a set of equations in both half spaces as follows:

$$H_y(z) = Ae^{i\beta x}e^{-k_d z} \tag{1.9}$$

$$E_x(z) = iA\frac{1}{\omega\epsilon_0\epsilon_d}k_d e^{i\beta x}e^{-k_d z} \tag{1.10}$$

$$E_z(z) = -A\frac{\beta}{\omega\epsilon_0\epsilon_d}k_d e^{i\beta x}e^{-k_d z} \tag{1.11}$$

for $z > 0$, and

$$H_y(z) = Be^{i\beta x}e^{-k_m z} \tag{1.12}$$

$$E_x(z) = -iB\frac{1}{\omega\epsilon_0\epsilon_m}k_m e^{i\beta x}e^{-k_m z} \tag{1.13}$$

$$E_z(z) = -B\frac{\beta}{\omega\epsilon_0\epsilon_m}k_m e^{i\beta x}e^{-k_m z} \tag{1.14}$$

for $z < 0$, where $k_d = \sqrt{\beta^2 - {k_0}^2\epsilon_d}$ and $k_m = \sqrt{\beta^2 - {k_0}^2\epsilon_m}$ is the component of the wavevector perpendicular to the interface between the two media, whose reciprocal value $\delta_d = 1/|k_d|$ and $\delta_m = 1/|k_m|$ defines the exponential decay length of the fields perpendicular to the interface, which quantifies the confinement of the wave [12]. Applying the appropriate boundary conditions for continuity of H_y and $\epsilon_i E_z$ at the interface, yields $A = B$ and $k_d/k_m = -\epsilon_d/\epsilon_m$. Substituting the values for k_m and k_d yields the dispersion

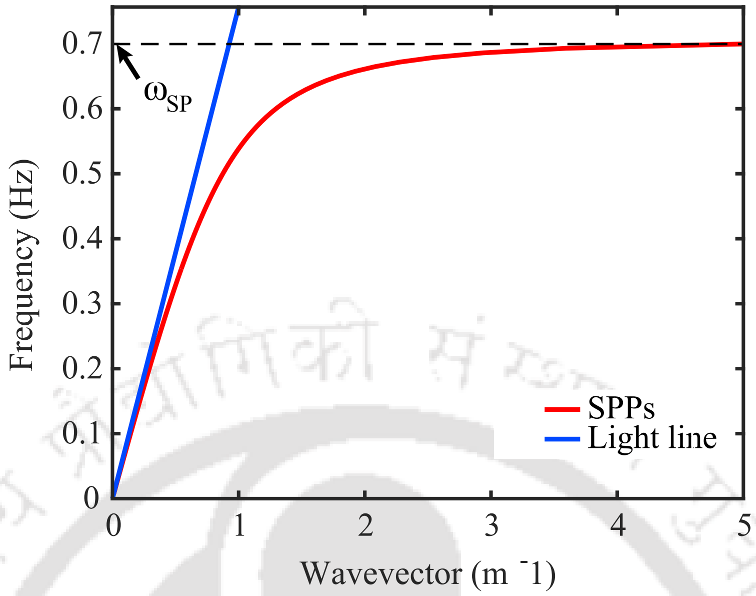

Figure 1.5: The wavevector *vs* frequency representation of SPs along with that of the incident light.

relation of the SPs propagating at the interface between the two media having relative permittivity, ϵ_m and ϵ_d, respectively, is given by the expression

$$\beta = k_0\sqrt{\frac{\epsilon_m\epsilon_d}{\epsilon_m+\epsilon_d}} \tag{1.15}$$

where β is the wavevector of the surface plasmon waves and k_0 is the wave vector of the incident light in free space. A more rigorous derivation is given in ref [12]. Figure 1.5 shows the dispersion characteristics of the SPs along with that of light. It is evident from the figure that the wave vector of SPs is always larger than that of light in free space and the wavelength of SPs is always smaller than the light wavelength. The fact that a wave with a shorter wavelength would suffer less diffraction can be enough to break the diffraction limit of light. This makes SPs attractive for various applications in the subwavelength scale. Further, in the dispersion relation of SPs, it is observed that in the low frequency region, the SP wavevector is small and is close to that of the light line. For larger wavevector, the frequency approaches a characteristic surface plasmon frequency $\omega_{SP} = \omega_p/\sqrt{1+\epsilon_d}$. It can be observed that the wavevector β goes to infinity as the frequency approaches ω_{SP} and group velocity tends to 0. At this limit the field is squeezed at the interface and hence allows tight localization of the electromagnetic fields.

If the metal loss is considered, the dielectric properties of metal are described by a complex dielectric function $\epsilon_m = \epsilon_m^{'} + i\epsilon_m^{''}$. The propagation constant is expressed as $\beta(\omega) = \beta^{'}(\omega) + i\beta^{''}(\omega)$, where the real part represents the phase shift rate due to propagation and the imaginary part accounts for absorption. The travelling SPs are damped with an attenuation length, $L = [2\beta^{''}(\omega)]^{-1}$, typically between 10 and 100 μm in the visible regime, depending upon the geometry of the metal-dielectric concerned [12]. From the dispersion relation, it is evident that both the attenuation length and the confinement in the dielectric medium are strongly dependent on frequency. At frequencies close to ω_{SP}, SPs exhibit large field confinement to the interface and subsequent small propagation distance due to increased damping. This characteristic trade-off between the confinement and loss is typical for plasmonic structures.

Since the wave vector of SP is always greater than that of light in free space i.e., $\beta > k_0$ the projection of the light momentum along the interface is always smaller than the SP's propagation constant, prohibiting phase matching. Hence, the SPs on a flat metal/dielectric surface cannot be excited directly by light beams. Special techniques have been introduced for the excitation of SPs such as the prism coupler technique [160], grating technique [161], to impart the extra momentum to the light wave vector in order to match that of the SPs.

1.3.2 Excitation of surface plasmon via EIT

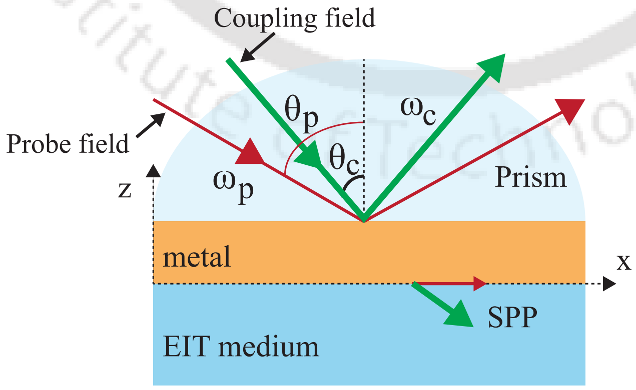

Figure 1.6: Schematic diagram of the prism coupler system for the excitation of SP resonance. The system is composed of a cylindrical prism, a metal film, and an atomic EIT medium with permittivities ϵ_t, ϵ_m and ϵ_d, respectively.

The schematic of the prism coupler system for the excitation of SPs is illustrated in Fig. 1.6. Consider a planar waveguide structure consisting of a prism, a thin metal film and a bottom layer. The bottom medium is considered to be a lambda-type atomic medium, described in section 1.1. Then, the dielectric constant of the EIT medium is related to the susceptibility of the medium $\epsilon_d = 1 + \frac{\chi}{1-\frac{\chi}{3}}$ where χ is the susceptibility of the EIT medium given by the expression in Eq. (1.6).

For the given system, the three layer reflection and transmission coefficient is given by the Fresnel equations as follows:

$$r_{tmd} = \frac{r_{tm} + r_{md} e^{i2k_{mz}l}}{1 + r_{tm} r_{md} e^{i2k_{mz}l}} \tag{1.16}$$

and

$$t_{tmd} = \frac{t_{tm} t_{md} e^{ik_{mz}l}}{1 + r_{tm} r_{md} e^{ik_{mz}l}} \tag{1.17}$$

with $r_{tm} = \frac{\epsilon_m k_{tz} - \epsilon_t k_{mz}}{\epsilon_m k_{tz} + \epsilon_t k_{mz}}$ and $r_{md} = \frac{\epsilon_d k_{mz} - \epsilon_m k_{dz}}{\epsilon_d k_{tz} + \epsilon_m k_{dz}}$ as the reflection coefficient of the top-middle and middle-bottom interface, respectively. The transmission coefficient of the top-middle and the middle-bottom interface is expressed as $t_{tm} = 1 + r_{tm}$ and $t_{md} = 1 + r_{md}$, respectively. The transmittance and the total reflection is given by the expressions, $T = |t_{tmd}|^2$ and $R = |r_{tmd}|^2$, respectively. The normal wavevectors can be given by $k_{jz}{}^2 = k_0{}^2 \epsilon_j - k_x{}^2$ where $j = t, m, d$ and the parallel wave vector is given by $k_x = k_0 n_t \sin\theta_p$, where $k_0 = \omega/c$ is the vacuum wave number and θ_p is the incident angle of the probe field. An elaborate analysis for the generation of SPs in the system is given in Ref [76]. For a particular value of the angle of incidence of the probe and the coupling field, the parallel wave vector of the incident light satisfies the phase matching condition, $\beta = k_0 n_t \sin\theta_p$. At this position, the total transmission T increases to a large value and the reflection R drops to a small value such that $R << T$. This indicates the excitation of the SP resonance in the prism coupler system. The excitation of the SP resonance can be controlled by modulating the field parameters of the probe and the coupling field as well.

The drawback of the prism coupler system, however, is that it cannot be used for applications in highly compact nano-optical devices, since the dimension of the prism cannot be less than the wavelength of the incident light. In this context, the possibility of exciting SP resonances without the use of any coupling mechanism in a multilayer planar waveguide structure via EIT has been recently explored [78, 95]. Within the transparency window, a giant Kerr nonlinearity is achieved, which in turn, could be exploited to generate nonlinear waves in these structures [95, 96]. Novel theories have also been proposed where an incident light is transversely tightly guided at a metal-dielectric interface with the help of EIT phenomenon, and laterally self-trapped by the inherent nonlinear Kerr effect to yield a plasmon-soliton [95]. Plasmon-solitons are basically electromagnetic surface waves confined at the interface inheriting the shape preserving properties of solitons [54]. Subsequently, the EIT phenomenon could be employed as a means to compensate the propagation loss of the SPs in planar plasmonic waveguide structures.

1.4 Outline of the thesis

In the following, we present the plan of the thesis by including a brief description of the various problems that have been tackled in the form of different chapters. The thesis is primarily divided into two parts: The first part of the thesis discusses the analogue of the electromagnetically induced transparency effect in different terahertz metamaterials. Part I of the thesis comprises of chapter 2, chapter 3 and chapter 4. In the second part of the thesis, we study the excitation of surface polaritonic solitons and Akhmediev breather in a planar plasmonic waveguide structure based on the effect of electromagnetically induced transparency (described in Chapter 5). Finally, we provide the summary of the thesis in chapter 6, followed by a future scope of the work.

In Chapter 2, we discuss the numerical and theoretical analysis of plasmon induced transparency (PIT) in a planar terahertz metamaterial comprising of two C-shaped resonators and a cut-wire structure, placed alternately on both sides of the cut-wire. We show that the PIT window is modulated by displacing the C shaped resonators with respect to (w.r.t.) the cut-wire. An equivalent circuit model is provided to explain the numerical observations for different coupling configurations. We further show that a polarization independent response PIT response can be achieved in a terahertz metamaterial configuration that comprises of a cross wire and four C-shaped (4C) resonators. For two orthogonal polarizations of the incident terahertz beam, an identical transmission response is achieved indicating a polarization independent PIT behavior. This study could be significant in the realization of terahertz devices such as tunable switches, modulators and polarization independent slow light systems.

Chapter 3 discusses the PIT effect in a novel graphene metamaterial comprising of a pair of graphene SRRs placed alternately on both sides of the graphene strip. The PIT effect is modulated by varying the vertical displacement as well as horizontal displacement of the split ring resonators w.r.t. the graphene strip. The PIT effect is also examined for different values of Fermi energy of the graphene material. Finally, we validate our numerical findings by employing a theoretical model based on the three-level plasmonic system. The theoretical results are in good agreement with the numerical results. The dynamic tuning achieved in our study could be significant in designing frequency tunable, active and reconfigurable terahertz metamaterials in near future.

In Chapter 4, we discuss a scheme to achieve dual-band EIT effect in a planar terahertz metamaterial, comprising of an inner circular split ring resonator (CSRR) concentrically coupled to an outer asymmetric two-gap circular split ring resonator (ASRR). We show the modulation of dual-band EIT effect by rotating the inner CSRR. Modulation of the effect is further achieved by varying the asymmetry in the ASRR and the size of the CSRR in the proposed metamaterial. A theoretical model based upon the four-level tripod (FLT)-system provides an intuitive explanation about the underlying coupling mechanism responsible for dual-band EIT effect in the proposed metamaterial structure. The study is significant in the development of multi-band slow light devices, narrowband absorbers, etc. in the terahertz regime.

Chapter 5 discusses the coupler-free excitation of polaritonic solitons and breathers in a planar plasmonic waveguide structure comprising of a transparent layer, a metal layer and a layer of three-level lambda-type atomic medium. A coupler-free excitation of SP resonances is achieved via EIT in the proposed system. The EIT phenomenon gives rise to Kerr nonlinearity in the system which balances the dispersion in the system, providing the necessary condition for the excitation of polaritonic solitons in the system. The generation and evolution of the bright and dark polaritonic solitons in the system is investigated. Further, we examine the excitation of surface polaritonic Akhmediev breathers in the proposed system. We show that a stable propagation of the polaritonic solitons and breathers is achieved in the proposed system. This experimentally feasible scheme could be significant in the development of highly compact nano-photonic devices in the optical regime.

Chapter 6 provides the conclusion of the thesis along with a summary of the major findings of the research work carried out followed by a brief outline on the scope for future studies.

Part-I

CHAPTER 2

PLASMON INDUCED TRANSPARENCY THROUGH ALTERNATELY COUPLED RESONATORS IN A TERAHERTZ METAMATERIAL

2.1 Introduction

Plasmon induced transparency (PIT) effect in MMs has garnered a lot of interest over the past decade. The PIT effect and its occurrence in MMs have been discussed in detail in the previous chapter. The effect has been realized in a variety of MM configurations such as metal strips and coupled split ring resonators in the gigahertz as well as the terahertz regimes [73, 74, 140–142, 162–165]. In recent times, strategically designed MM structures have been examined in the pursuit of a polarization independent PIT response [100–102]. Research in this area is presently driven by the prospect of realizing potential applications of the effect such as sensors [111–113, 143, 166, 167], slow light systems [94, 109, 156–158], broadband applications [103, 104], modulators [168, 169], etc. in the terahertz regime. In this context, we examine PIT effect in a coupled resonator terahertz MM configuration comprising of two C-shaped (2C) resonators and a cut-wire (CW) like structure. The PIT in the proposed

---

The results of the work reported in this chapter has been published in *Opt. Express*, vol. **25**, year 2017, pages 10484-10493; title:"Plasmon induced transparency effect through alternately coupled resonators in a terahertz metamaterial"; authors: Koijam Monika Devi, Amarendra K. Sarma, Dibakar Roy Chowdhury, and Gagan Kumar.

model occurs due to the destructive interference between the CW and the 2C resonators. Although, the displacement of the C-shaped resonators in the vertical direction has been studied in earlier works [106, 141], the novelty of our work stems from the investigation of the coupling mechanism in the horizontal direction which results in transition from a strongly coupled system to a weakly coupled system. When the C-shaped resonators are displaced in the vertical direction, the dark mode excitation in the PIT MM is achieved through both electric and magnetic fields of the CW. As the C-shaped resonator pair is translated along the CW starting from the bottom, the coupling mechanism switches from being capacitive in nature via the electric field to being inductive via the magnetic field of the CW [141]. However, in our case, the dark mode is excited only through the electric field of the CW as the C-shaped resonators are translated in the horizontal direction, resulting in a capacitive coupling between the C-shaped resonator pair and the CW.

In this chapter, we first discuss the design and numerical simulations of the PIT effect with alternately placed C-shaped structures w.r.t. the cut wire. It is observed that the transparency window can be broadened by increasing the coupling between the CW and the two C resonators. A simple lumped element equivalent circuit model using coupled oscillator theory is provided to corroborate the numerical observations. In exploring PIT, the studies largely have focused to examine this effect for a specific polarization of the incident light for which the effect is prominent. As we switch to the different polarization, the effect becomes either weaker or completely vanishes. This may limit the use of PIT effect for development of sensing applications. In order to overcome this, we introduce two C and a CW structure in the perpendicular orientation in our MM geometry so that the new meta-molecule consists of a cross wire and four C (4C) resonators. Finally, we examine the PIT effect from this new meta-atom for two orthogonal directions of polarization of the incident radiation to establish the polarization independent response.

2.2 Design and numerical simulations

The schematic diagram of the proposed MM geometry is shown in Fig. 2.1(a).The meta-molecule of the proposed structure comprises of a CW and two C shaped resonators and is designed in a way that they can exhibit PIT effect with the CW as the bright resonator. In the proposed geometry, the quantity $'L'$ represents the length of the CW,

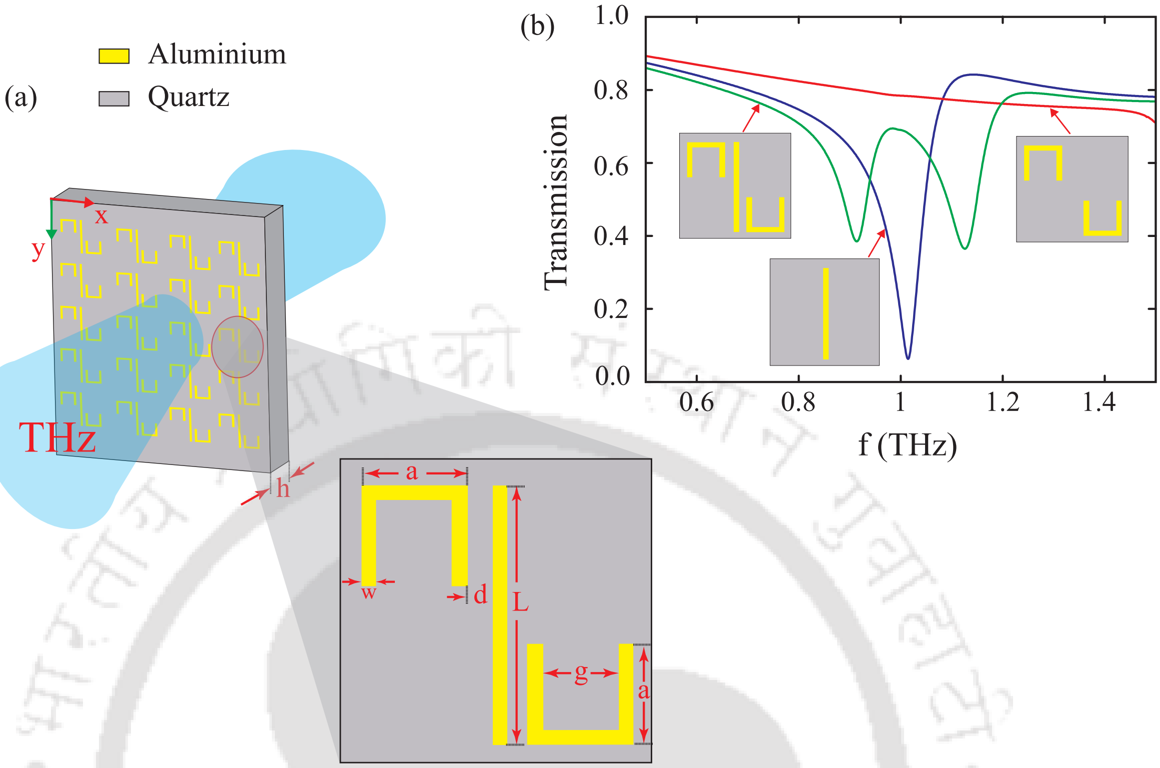

Figure 2.1: (a) Schematic diagram for the study of the PIT effect through the planar MM geometry comprising of a cut-wire and two C shaped resonators. (b) Transmission response for CW, 2C and the PIT effect for the y-polarized incident light.

$'a'$ represents the dimension of each of the C shaped resonator, $'w'$ denotes the width of the CW as well as the C resonators and $'g'$stands for the gap of the C shaped resonators. The periodicity of the meta-molecule is denoted by $'p'$ and is taken to be 140 μm in our simulations. For our simulations, we have taken $L = 84$ μm, $a = 35$ μm, $w = 4$ μm and $g = 27$ μm. The distance $'d'$ between the CW and the 2C structures is varied in our numerical simulations to examine the modulation response of the PIT effect. The CW and the 2C are assumed to be made up of aluminium having thickness, $t = 200$ nm on a quartz substrate of thickness, $h = 25$ μm, with a relative permittivity $\epsilon_r = 3.75$. It may be noted that in the simulation model, we have considered dc conductivity to model aluminium. The numerical simulations are performed using the technique of frequency domain solver in CST Microwave Studio. The MM geometry is simulated under the unit cell boundary conditions in the x-y plane. We set open boundary conditions along the direction of light propagation and chose a mesh size of the order of $\lambda/10$, where λ is the wavelength of the incident radiation. The simulation is performed for the y linearly polarized light under the normal incidence.

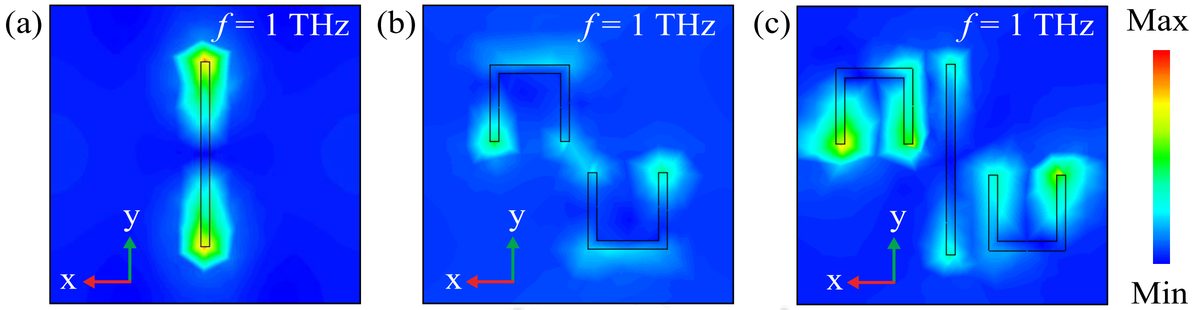

Figure 2.2: Electric field profiles of (a) the CW structures, (b) the 2C structures and (c) the proposed PIT MM. The green arrow signifies the direction of incident polarization of the electric field.

The terahertz transmission response through the proposed MM configuration for the y- polarized incident terahertz radiation id depicted in Fig. 2.1(b). The blue traces represent the bright mode while the red traces represent the dark mode. The green traces signify the PIT effect from the proposed terahertz MM geometry. It may be noted that the array of CWs exhibit a typical localized surface plasmon resonance at f = 1.0 THz while the two C structures support an LC resonance at the same frequency. The CWs couple directly to the incident light and has a broad spectral response. On the other hand, the 2 C structures result in a weakly coupled response to the incident terahertz beam. The resonances from the CWs and 2 C structures behave like a bright mode and dark mode respectively. The interference of these two modes induces a narrow transparency window in the transmission spectrum represented by green traces in the figure. In order to further understand the bright and dark modes as well as the PIT effect, we observe the induced electric field profiles in the transparency region i.e. at 1.0 THz. The results are shown in Fig. 2.2. We may note that the CW structure gets directly excited by the incident light resulting in a bright mode (Fig. 2.2(a)), while the 2 C shaped resonators are weakly excited by the incident field resulting in a dark mode (Fig. 2.2(b)). When these two modes are allowed to couple with each other, a narrow transparency window is induced due to the destructive interference of the modes (Fig. 2.2(c)). In this transparency window, the imaginary part of the field becomes negligible and the structure becomes highly dispersive. This results in the significant reduction of the velocity of the incident light.

We further examine the displacement of C-shaped resonators w.r.t. the CW which is responsible for a coupling between the resonator and hence a modulation of transparency

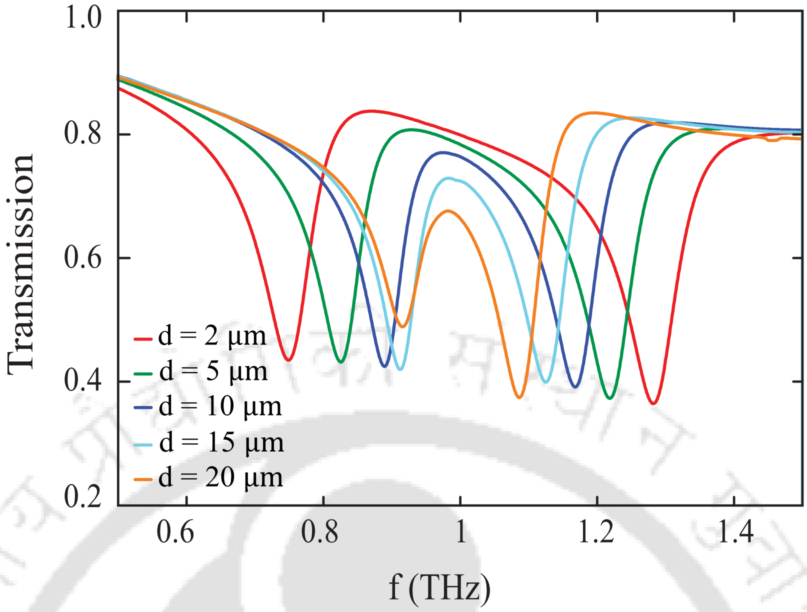

Figure 2.3: Electric field profiles of (a) the CW structures, (b) the 2C structures and (c) the proposed PIT MM structure. The green arrow signifies the direction of incident polarization of the electric field.

window is possible. This modulation is achieved by varying distance $'d'$ from 2 μm to 20 μm in the MM structure. The transmission response for different values of $'d'$ is shown in Fig. 2.3. The red traces represent the PIT effect for $d = 2$ μm of the PIT MM geometry. For this configuration, a broad transparency window is achieved owing to the strong coupling between the CW and 2C resonators. The green, blue and cyan traces represent the PIT effect for $d = 5$ μm, $d = 10$ μm and $d = 15$ μm respectively. The orange traces represent the case of $d = 20$ μm and contribute to the weakest coupling. It is evident from the figure that the PIT window gets narrower as we increase the distance $'d'$ between the CW and the 2C resonators. The narrowing of the PIT window occurs due to a reduction in the coupling of CW with the C-shaped resonators. Such behavior suggests an efficient modulation of the PIT effect by varying the coupling between the bright and the dark modes in the MM structure.

2.3 Semi-analytical model elaborating the PIT effect

In order to elucidate our numerical findings on the PIT effect as observed in this work, we use an equivalent RLC circuit model [143, 165], which is shown in Fig. 2.4. In the

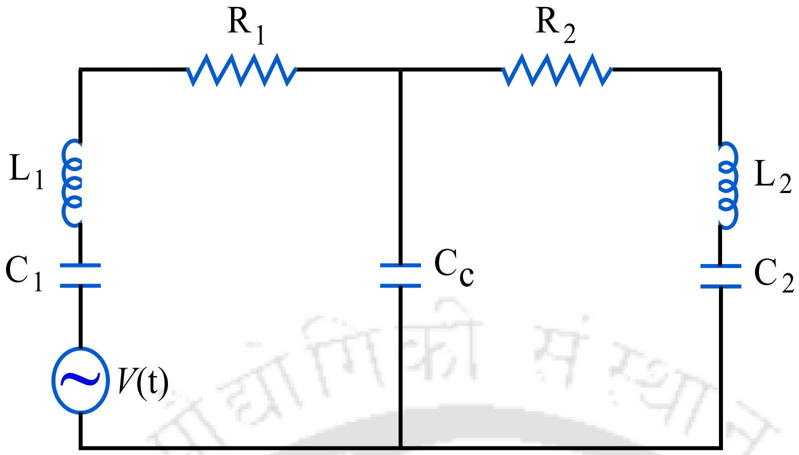

Figure 2.4: An equivalent circuit model for the proposed PIT MM structure is shown in Fig. 2.1(a).

model, both the left hand loop consisting of R_1, L_1, C_1 and the right hand loop consisting of R_2, L_2, C_2 constitutes a resonant circuit having resonance at f = 1.0 THz. The left hand loop represents the bright mode or the CW resonator, while the dark mode or 2C resonator is represented by the right hand loop. The capacitance C_c in the circuit accounts for the coupling between the bright and the dark modes. The incident terahertz field is represented by $V(t)$ in the model. The bright mode is directly excited by the incident terahertz radiation while the dark mode is excited through coupling with the bright mode.

The circuit model shown in Fig. 2.4 can be considered as a two-port system with input voltage V_1 and V_2. Then, for currents I_1 and I_2 flowing through the left and the right hand loop, the Z matrix equations is expressed as follows

$$\begin{pmatrix} V_1 \\ V_2 \end{pmatrix} = \begin{pmatrix} Z_{11} & Z_{12} \\ Z_{21} & Z_{22} \end{pmatrix} \begin{pmatrix} I_1 \\ I_2 \end{pmatrix}. \tag{2.1}$$

By following the standard circuit analysis, we get

$$\begin{pmatrix} V(t) \\ 0 \end{pmatrix} = \begin{pmatrix} -j\omega L_1 + R_1 + \frac{1}{-j\omega C_1} & \frac{1}{-j\omega C_c} \\ \frac{1}{-j\omega C_c} & -j\omega L_2 + R_2 + \frac{1}{-j\omega C_2} \end{pmatrix} \begin{pmatrix} I_1 \\ I_2 \end{pmatrix}. \tag{2.2}$$

For a general two port system, the Z parameters can be transformed into the S-parameters with the help of the standard conversion formula [170, 171], which is given below

$$S_{11} = \frac{(Z_{11} - Z_1^*)(Z_{22} + Z_2) - Z_{12}Z_{21}}{(Z_{11} + Z_1)(Z_{22} + Z_2) - Z_{12}Z_{21}}, \tag{2.3a}$$

$$S_{12} = \frac{2Z_{12}\sqrt{Z_1 Z_2}}{(Z_{11} + Z_1)(Z_{22} + Z_2) - Z_{12}Z_{21}}, \tag{2.3b}$$

$$S_{21} = \frac{2Z_{21}\sqrt{Z_1 Z_2}}{(Z_{11} + Z_1)(Z_{22} + Z_2) - Z_{12}Z_{21}}, \tag{2.3c}$$

$$S_{22} = \frac{(Z_{11} + Z_1)(Z_{22} - Z_2^*) - Z_{12}Z_{21}}{(Z_{11} + Z_1)(Z_{22} + Z_2) - Z_{12}Z_{21}}, \tag{2.3d}$$

where Z_1 and Z_2 are the source and the load impedances of the system. A detailed derivation for the conversion of parameters of a two-port system can be found in [170, 171]. By using the relations in Eq. (2.3), and by substituting the corresponding Z parameter values, the transmission coefficient is calculated as $t(\omega) = S_{21}$. For $Z_1 = Z_2 = Z_0$, where Z_0 is the vacuum impedance, we get the transmission coefficient as follows

$$t(\omega) = \frac{2j\omega Z_0 C_c}{\left[1 - \left(j\omega L_1 - R_1 + \frac{1}{j\omega C_1} - Z_0\right)\left(j\omega L_2 - R_2 + \frac{1}{j\omega C_2} - Z_0\right)\left(\omega C_c\right)^2\right]}. \tag{2.4}$$

Using Eq.(2.4), we can obtain the transmission response of the MM structure corresponding to a specific set of parameters used in our numerical simulations of the PIT effect. The transmission is calculated for different values of $'d'$ which causes a varying coupling between the CW and the two C-shaped resonators as discussed in section 2.1. Figure 2.5 depicts the theoretical fit of the transmission by using the semi-analytical model, for different values of d. It is worth mentioning that the provided circuit model uses a capacitive coupling, represented by C_c, to explain the PIT response in the proposed MM structure. This coupling could be modulated by varying the value of the capacitance C_c used in the model. It is observed that the inductance parameters (L_1 and L_2) and the capacitance parameters (C_1 and C_2) does not change significantly while the coupling strength in the model decreases with the increase of the horizontal distance, resulting in the narrowing of the PIT window. As such, this model can be used to predict the near field coupling in MM systems where capacitive coupling is dominant. It is evident that the results from semi-analytical approach (shown in Fig. 2.5) are in good agreement with the numerical observations of Fig. 2.3.

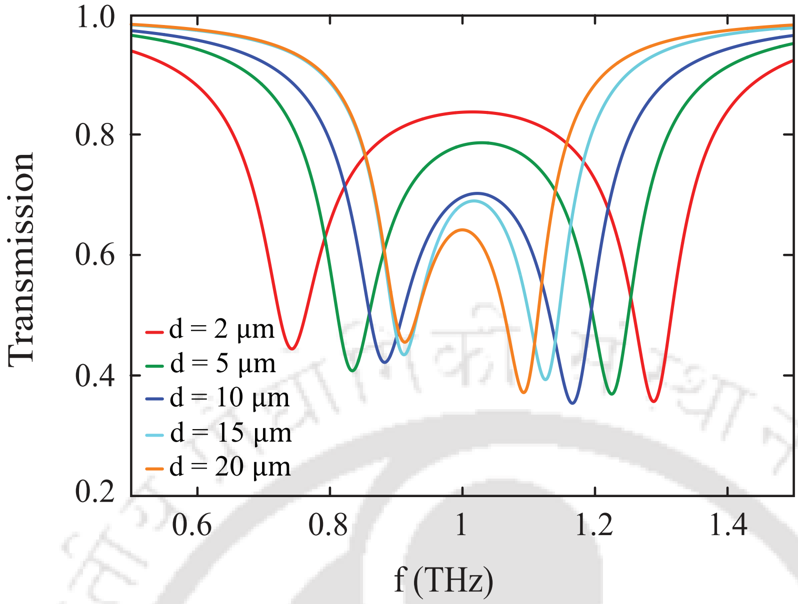

Figure 2.5: Transmission plot for the proposed MM structure obtained using the semi-analytical model. The value of the vacuum impedance is taken as $Z_0 = 377\ \Omega$ while the resistance parameters R_1 and R_2 are taken as 300 Ω and 5 $k\Omega$, respectively throughout the fitting. The PIT transparency window is modulated by varying the value of the capacitance C_c used in the model.

2.4 Polarization independent plasmon induced transparency

In the MM configuration proposed above, the PIT effect occurs only when the incident polarization is parallel to the longitudinal direction of the CW. However, for certain applications, a polarization independent response may be desirable. In order to achieve a polarization independent PIT effect, we introduce two more C structures and one CW structure after being rotated orthogonally in the same plane, in the above MM geometry. The schematic of this new meta-atom, now comprising of a cross and four C resonators is shown in Fig. 2.6, along with the transmission results. We examine the transmission response through this new design for the x and y-linearly polarized lights so as to elucidate our impression of a polarization independent response. We observe that the design exhibits equally strong PIT effect for both the polarizations which is explained through several steps in Figs. 2.6(a)-(f). In the figure, green arrow indicates the direction of incident polarization. The red traces signify the transmission for x-polarized light while the blue traces represent the transmission for the y-polarized

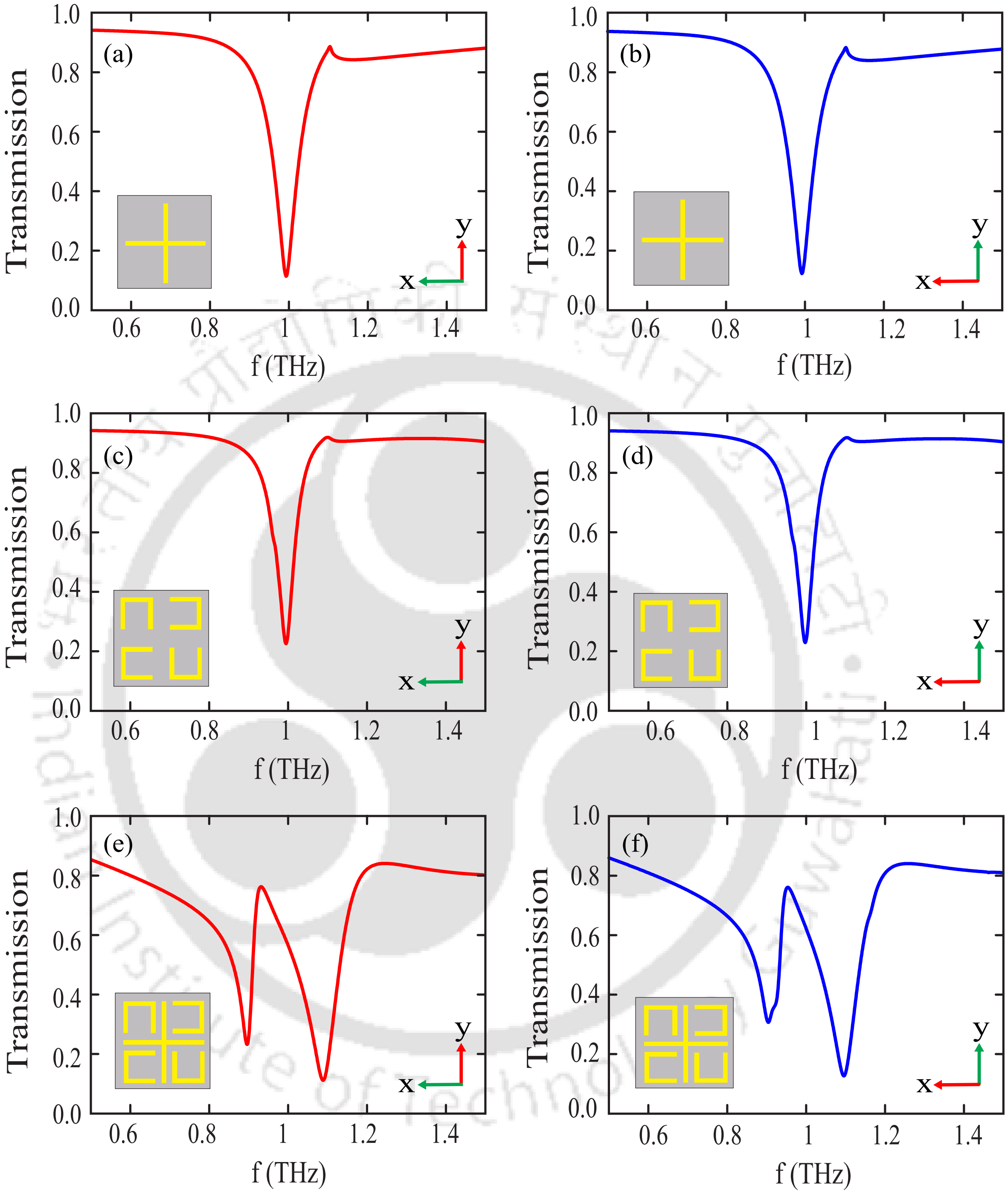

Figure 2.6: Terahertz transmission through CW structure for the (a) x-polarized and (b) y-polarized incident terahertz light. The green arrow indicates the direction of electric field polarization of incident light. (c) and (d) represent the terahertz transmission for the 4C structure for the two polarizations. (e) and (f) correspond to the PIT effect for both the polarizations. The inset in the figures show the corresponding MM geometry.

light. The transmission for the cross structure is shown in Figs. 2.6(a) and 2.6(b) while the transmission for the four C structures is represented by Figs. 2.6(c) and 2.6(d). The cross structures show a typical localized surface plasmon resonance at f = 1.0 THz while the 4C supports an LC resonance at the same frequency i.e. f = 1.0 THz. It is clearly observed from the Figs. 2.6(a)-(d) that the cross structure has a broader and deeper transmission dip than that of the 4C structures. The resonance from the cross structure is believed to be a bright mode, however the resonance from the C shaped structures is called a dark mode. When these two modes are allowed to couple with each other, a narrow transparency window is induced due to the destructive interference of the modes. Fig. 2.6(e) and 2.6(f) represents the PIT effect of the proposed geometry for both the x and y-linearly polarized lights. We notice an equally strong PIT effect for both the incident polarizations which indicates a polarization independent response of the proposed geometry.

Further, we examine the induced electric field profiles for the cross structure, the 4C structure and the PIT MM structure individually (see Fig. 2.7). The incident polarization is parallel to the direction of the green arrow in the figure. Figure 2.7(a) and 2.7(b) represent the electric field profiles of the cross structure at f = 1.0 THz, for x and y-linearly polarized incident light respectively. Figure 2.7(c) and 2.7(d) represent the electric field profiles of the 4C structure at f = 1.0 THz, for the x and y-linearly polarized incident lights respectively. It may be noted that for each of the incident polarizations, only the cut wire of the cross structure that is parallel to the incident light is excited, while for the C-shaped resonators whose gap is perpendicular to the incident polarization direction does not get excited in case of 4C structure. When the modes from these excitations are allowed to couple with each other, a narrow transparency window is induced due to the destructive interference of the modes. Figure 2.7(e) and 2.7(f) represent the electric field profiles of the PIT effect corresponding to this MM geometry at the PIT transmission peak frequency of f = 1.0 THz.

Finally, we explore the possibility of modulating the PIT window through this proposed terahertz MM configuration. For doing so, we examine the polarization independent PIT response for different values of $'d'$ for both x and y-linearly polarized incident terahertz light. A change in the value of $'d'$ results in the diagonal shifting of C-shaped resonators w.r.t. the cross wire. The results are shown in Fig. 2.8. Figure 2.8(a) represents the transmission for the x-polarized incident light while the transmission response for

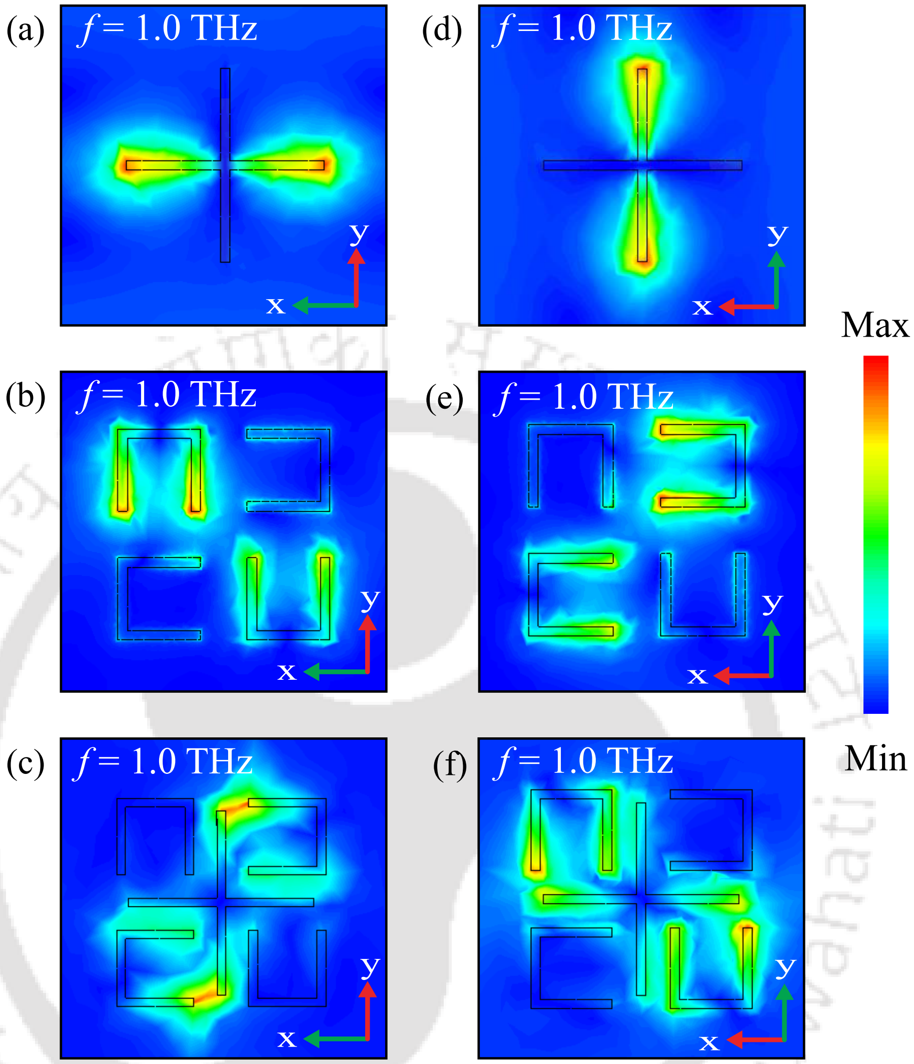

Figure 2.7: Absolute value of electric field profile for cross structure for (a) x-polarized and (b) y-polarized light at the resonance frequency $f = 1.0$ THz. Electric field profile for 4C structure for (c) x-polarized and (d) y-polarized light at the resonance frequency $f = 1.0$ THz. Electric field profile for the PIT MM structure at the PIT dip for the x-polarized and y-polarized light are depicted in (e) and (f). The incident electric field is parallel to the direction of the green arrow.

the y-polarized light is shown in Fig. 2.8(b). It is evident from the figure that the PIT effect is equally strong for both the x and y-incident polarizations. It may be further observed that the transparency window can be modulated by changing the coupling between the cross wire and the C shaped structure through the variation of $'d'$. The traces in different colors in the figure represent the transmission response for different values of $'d'$ as labeled in the figure itself. The red traces for $d = 2\ \mu m$ show the widest, while orange trances for $d = 20\ \mu m$ depict the narrowest transparency window.

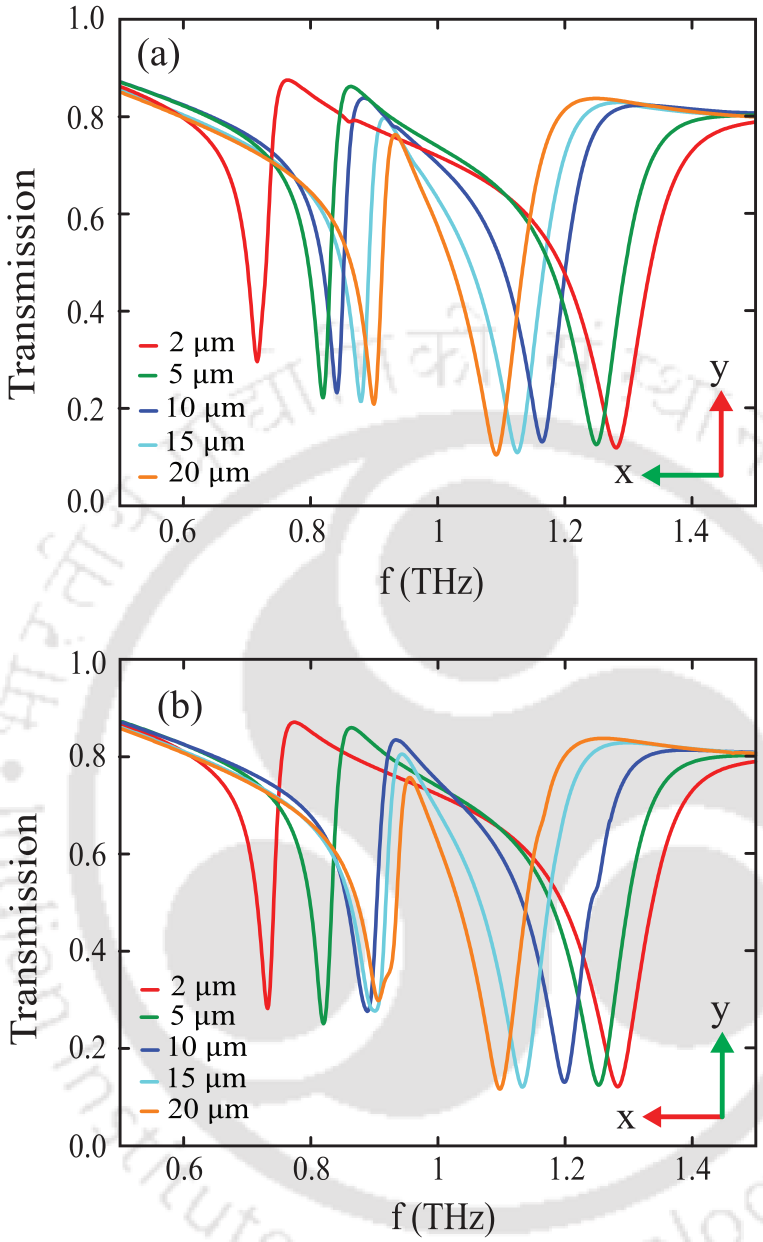

Figure 2.8: Transmission for a MM comprising of a cross and 4C resonators: (a) x-polarized light and (b) y-polarized light for different values of $'d'$. As d increases, there is a reduction in the transparency window observed due to decreased coupling.

A reduction in the transparency window observed is due to the decrease in coupling as $'d'$ increases. The efficient modulation of the PIT window suggests the prospect of developing devices operating within the broad transparency region in terahertz domain. Also, the polarization independent behavior could be significant in the improvement of sensing devices.

2.5 Conclusions

We have numerically and theoretically analyzed coupled terahertz MM comprising of two C-shaped resonators and a cut-wire (CW) structure. The PIT in the proposed configuration occurs due to the destructive interference of the resonances from the cut-wire (CW) and the two C-shaped resonators. It is observed that the transparency window can be broadened by increasing the coupling between the CW and 2C structures. A simple equivalent circuit model using coupled oscillator theory is described to validate our numerical observations. We extend our analysis to the terahertz MM configuration that comprises of a cross wire and four C-shaped (4C) resonators in order to achieve polarization independent response. Therefore PIT response of this geometry is examined for the two orthogonal polarizations of the incident terahertz beam. The identical transmission response indicates a polarization independent PIT behavior. In this geometry, the transparency window is modulated by displacing the C-shaped resonators diagonally w.r.t. the cross-wire. As the resonators are displaced away from the cross wire, the transparency window gets narrower due to a decrease in the coupling strength. The proposed study could be significant in the realization of terahertz devices for broadband applications, sensing and polarization independent slow light systems.

CHAPTER 3

PLASMON INDUCED TRANSPARENCY IN GRAPHENE BASED TERAHERTZ METAMATERIALS

3.1 Introduction

In the previous chapter, we discussed PIT effect in a planar terahertz MM structure comprising of two C-shaped resonators (2C) and a cut-wire (CW) structure made of aluminium metal. For most of the metal based MMs, the tuning of the PIT effect is achieved by altering the geometrical parameters of the structures, which limits the active tuning capability of the MM structure. In order to overcome this restraint, the PIT effect in MMs has recently been examined by incorporating nonlinear media or semiconductor material in the structure [99, 172]. But only limited tuning could be achieved in the case of metal MM structures. The quest for a better and efficient tuning of the PIT effect, led to the study of this effect using graphene based MMs. Graphene provides extreme field confinement and low propagation losses. Its Fermi energy can be varied easily by applying an external gate voltage or through chemical doping [173–176]. This has sparked a lot of interest in exploring the efficient dynamic tunabilty of the PIT effect in the graphene MMs in the mid-infrared [105, 107, 145–

The results of the work reported in this chapter has been published in *Europhysics Letters*, vol. **120**, year 2017, pages 27005; title:“Plasmon induced transparency in graphene based terahertz metamaterials”; authors: Koijam Monika Devi, Maidul Islam, Dibakar Roy Chowdhury, Amarendra K. Sarma and Gagan Kumar.

147, 153, 164] as well as terahertz frequency regions [150, 177, 178]. Tunable slow light phenomenon through PIT effect in graphene MM structures has been studied through the variation of Fermi energy [105, 107, 145]. Metal split ring resonators (SRRs) coupled to a graphene strip has also been found to exhibit the PIT effect [105, 107, 145]. Comb like structure [146, 148], as well as dipole-dipole coupling [149], a graphene ring coupled to a graphene strip [152] are some configurations that has been investigated in the recent years. Currently, the PIT effect in graphene based MMs is rigorously investigated using strategic geometries to explore the possibility of realizing dynamically tunable devices such as sensors, ultrafast switches and slow light systems [105, 150, 152]. In spite of the investigations, none of the study has been focused in exploring the PIT effect in graphene based terahertz MM structures. In this chapter, we report a novel graphene MM structure comprising of a pair of graphene SRRs placed alternately on both sides of the graphene strip. The field of graphene and terahertz MMs has grown significantly in last few years [150, 174, 177, 178]. However, there is ample scope to explore and understand the PIT effect in graphene based MMs and optimize their performance to actualize the construction of terahertz devices.

Here, we investigate the PIT effect in a graphene based MM structure whose meta-atom comprises of a pair of graphene SRRs placed alternately on both sides of the graphene strip. The PIT effect in a terahertz graphene MM structure is numerically and theoretically analyzed. The transmission characteristics of the proposed graphene MM structure are studied for different vertical configurations. Simulations reveal that the PIT effect in the graphene MM vanishes when the centers of the graphene SRRs and the graphene strip are collinear. We have also thoroughly examined the PIT effect in the graphene MM when the SRRs are displaced horizontally w.r.t. the graphene strip. Further, the PIT effect is studied for different values of Fermi energy of the graphene material. It is observed that the PIT window exhibits a blue shift as the Fermi energy gradually increases from 0.4 eV to 0.7 eV. Finally, a theoretical model based on the three level plasmonic systems is established in order to elucidate our numerical observations.

3.2 Design of graphene terahertz metamaterial

The schematic diagram for the study of the PIT effect in the graphene based terahertz metamaterial structure along with its meta-atom is depicted in Fig.3.1(a). The

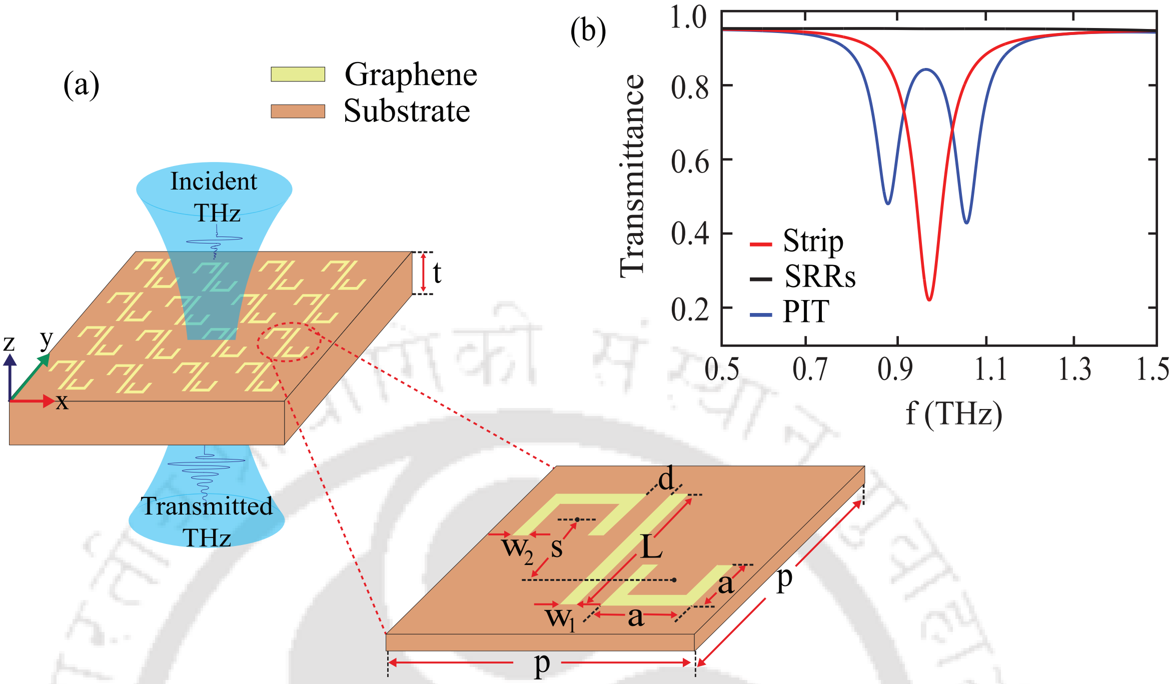

Figure 3.1: (a) Schematic illustration for the study of the PIT effect in the graphene based terahertz metamaterial structure along with the meta-atom comprising of a pair of graphene split ring resonators and a graphene strip, (b) Individual transmission profile versus frequency for the graphene strip, graphene SRRs and the graphene PIT MM structure.

transmission characteristics of the graphene MM structure are investigated using the finite-element-method-based frequency domain solver in the CST Microwave Studio. The MM structure is composed of a strip and a pair of SRRs made of graphene material having a thickness of 1 nm placed on a substrate of thickness $t = 10\ \mu m$, having a dielectric permittivity of 2.4. The graphene strip and the graphene SRRs are designed such that they have similar resonance frequency, with very little deviation, upon excitation by the incident light. The length and width of the graphene strip is $L = 19\ \mu m$ and $w_1 = 1.1\ \mu m$, respectively. The outer dimensions of each graphene SRR is $a \times a = 6.7\ \mu m \times 6.7\ \mu m$ and width is $w_2 = 0.9\ \mu m$. "d" is the distance between the graphene strip and the graphene SRRs while "s" is the distance between the centers of the two graphene SRRs. The periodicity of the structure is taken as $p = 24\ \mu m$. The MM structure is simulated under unit cell boundary conditions in the x-y plane. An adaptive mesh size of the order of $\lambda/10$, where λ is the wavelength of the incident radiation, is employed. Open boundary conditions is set along the direction of light propagation. The conductivity of graphene in the terahertz frequency range is described by a simplified Drude expression [173]:

$$\sigma(\omega) = \frac{e^2 E_f}{\pi \hbar^2} \frac{i}{\omega + i\tau^{-1}} \tag{3.1}$$

where e is the electronic charge and E_f is the Fermi energy and τ is the intrinsic relaxation time of the graphene material. The transmission results of the graphene strip, graphene SRRs and the hybrid graphene MM structures are shown in Fig.3.1(b). The red line represents the transmittance of the graphene strip while the black traces represent the transmittance of the graphene SRRs. It is evident from the figure that the graphene strip is directly excited by the incident radiation, whereas the fundamental mode of the pair of graphene SRRs is not excited by the incident radiation. Hence, the graphene strip behaves as the bright mode while the graphene SRRs behave as the dark mode. When these graphene SRRs are kept in the vicinity of the graphene strip, they couple through the induced electric field of the graphene strip. This coupling causes a PIT effect in the graphene MM structure, which is represented by the blue line in Fig. 3.1(b).

3.3 Results and Discussions

The transmission characteristics of the proposed MM structure are studied for different vertical and horizontal configurations. Figure 3.2(a) represents the transmittance of the graphene MM structure for different variations in "s" while $d = 1.5\ \mu m$ is fixed. The red line represents the transmittance of the MM structure when $s = 0\ \mu m$. The green line represents transmittance for $s = 4\ \mu m$ while the blue traces signify the transmittance for $s = 6\ \mu m$. The cyan and the orange traces represent the transmittance of the MM structure for $s = 8\ \mu m$ and $s = 11\ \mu m$, respectively. Simulations reveal that there is no PIT effect in the graphene MM when both the SRRs are collinear to each other, i.e., $s = 0\ \mu m$. However, as the graphene SRRs are displaced away from each other in the vertical direction, the graphene MM starts exhibiting the PIT effect. Next, the transmittance of the graphene MM structure for different values of "d" is shown in Fig.3.2(b). In this case, we have assumed "s" to be fixed. The orange line represents the transmittance of the MM structure when $d = 0.5\ \mu m$. The cyan line represents the transmittance for $d = 1\ \mu m$ while the blue traces signify the transmittance for $d = 1.5\ \mu m$. The green and the red traces represent the transmittance for $d = 2.5\ \mu m$ and $d = 3.5\ \mu m$, respectively. It may be noted that, as d increases, the PIT window becomes narrower due to the reduced coupling between the graphene strip and the graphene SRRs.

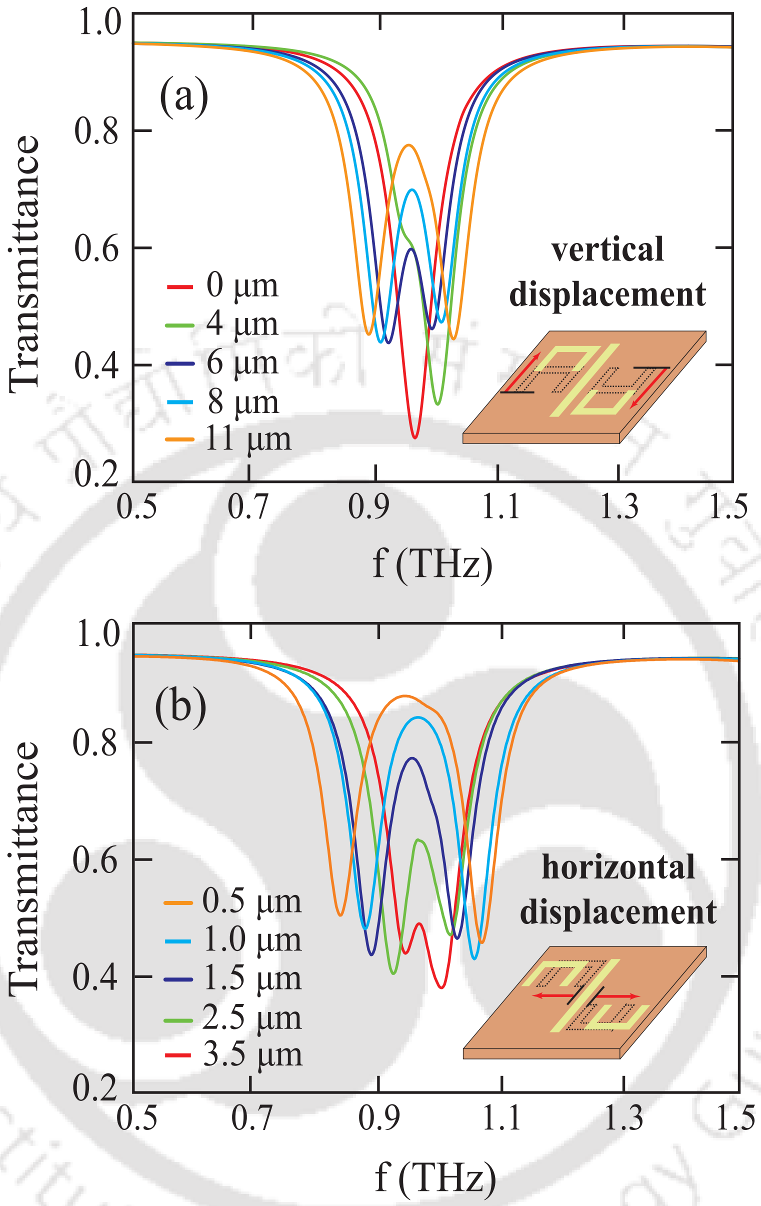

Figure 3.2: Numerically simulated transmittance of the graphene MM structure for (a) different values of vertical distance "s" by fixing the horizontal distance, $d = 1.5\ \mu m$ and (b) different values of the horizontal distance "d" for a fixed value of vertical distance, $s = 11\ \mu m$. The Fermi energy is kept fixed at a value, $E_F = 0.5\ eV$ in both the cases.

In order to get insight about the PIT effect in the graphene MM, we study the electric field profiles for various vertical and horizontal configurations. Figure 3.3(a)-(c) represents the electric field profiles of the MM structure for $s = 0\ \mu m$, 6 μm and 11 μm. It is evident from Fig.3.3(a), that the coupling between the graphene strip and the graphene SRRs is negligible for $s = 0\ \mu m$, i.e., when the centers of the graphene SRRs

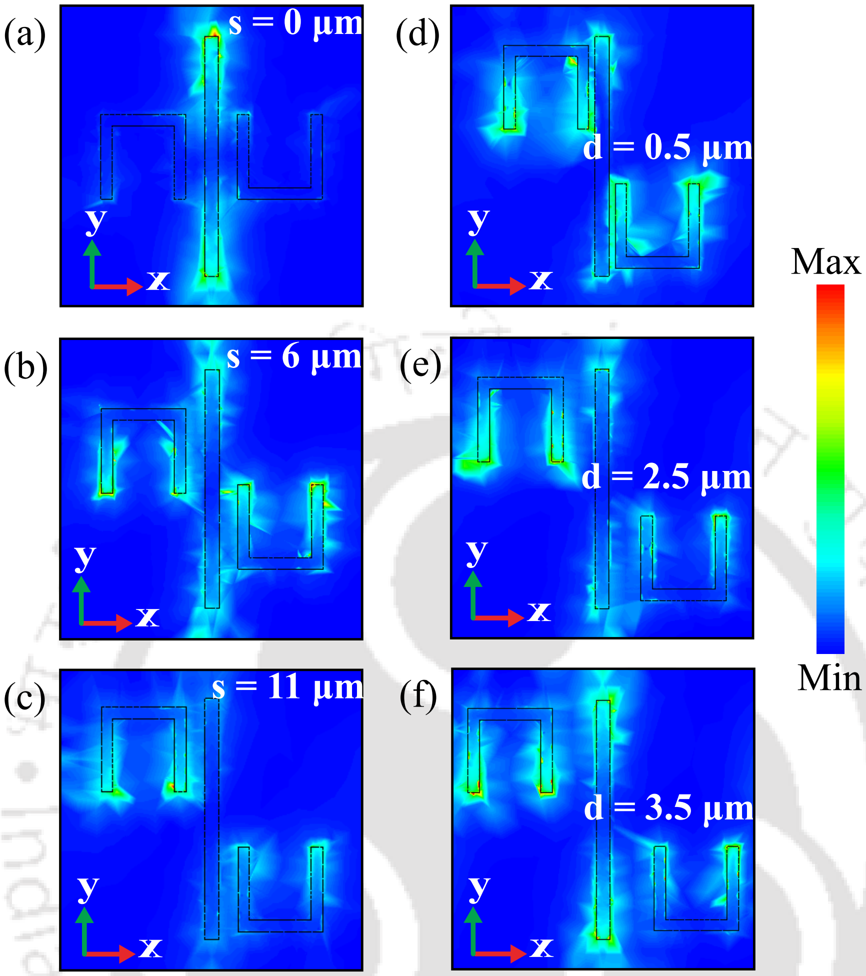

Figure 3.3: (a) Electric field profile of the graphene MM structure for different vertical configurations (a) $s = 0$ μm, (b) $s = 6$ μm, (c) $s = 11$ μm and different horizontal configurations (d) $d = 0.5$ μm, (e) $d = 2.5$ μm and (f) $d = 3.5$ μm. The incident electric field is along the direction of the green arrow.

and the graphene strip are collinear. This leads to the vanishing of the PIT effect in the MM structure. This is a very interesting feature as the PIT effect does not vanish for the similar configuration in a metal-based MM structure. In metals, when the SRRs are shifted away from the center in the vertical direction, the PIT effect occurs due to inductive coupling via the magnetic field as well as capacitive coupling via the electric field of the middle strip. When the SRRs are placed close to the center of the middle strip, the dark-mode excitation occurs due to the magnetic field of the strip, whereas when the SRRs are close to the edges of the strip, the electric field is responsible for the excitation of dark-mode resonance [141]. We believe that in graphene-based MM, the dark mode is neither excited by the electric field nor by the magnetic field of the graphene strip. However, as the SRRs are displaced away from the center in the opposite direction, the graphene MM structure starts to exhibit the PIT effect.The electric field profile for $s = 6\ \mu m$ is shown in Fig.3.3(b). As the SRRs are further displaced towards the edge of the strip, the PIT window becomes wider due to an increased coupling between the graphene strip and the graphene SRRs. Figure 3.3(c) represents the electric field profile for $s = 11\ \mu m$. In this case, the graphene SRRs is close to the edge of the graphene strip and hence the dark-mode excitation takes place through the electric field of the graphene strip. The electric field profiles for different horizontal displacements, i.e., $d = 0.5\ \mu m$, 2.5 μm and 3.5 μm are also shown in Figs. 3.3(d), 3.3(e) and 3.3(f), respectively. It is clearly evident from the Fig. 3.3(d) to 3.3(f) that the coupling between the graphene strip and the graphene SRRs is the maximum for $d = 0.5\ \mu m$. This configuration corresponds to a wider PIT window (see Fig.3.2(b)). As the graphene SRRs are displaced away from the graphene strip in the horizontal direction, the coupling between them reduces. When $d = 3.5\ \mu m$, the graphene strip and the graphene SRRs are almost uncoupled. This results in the narrowing of the PIT window and fading of the PIT effect in the MM structure.

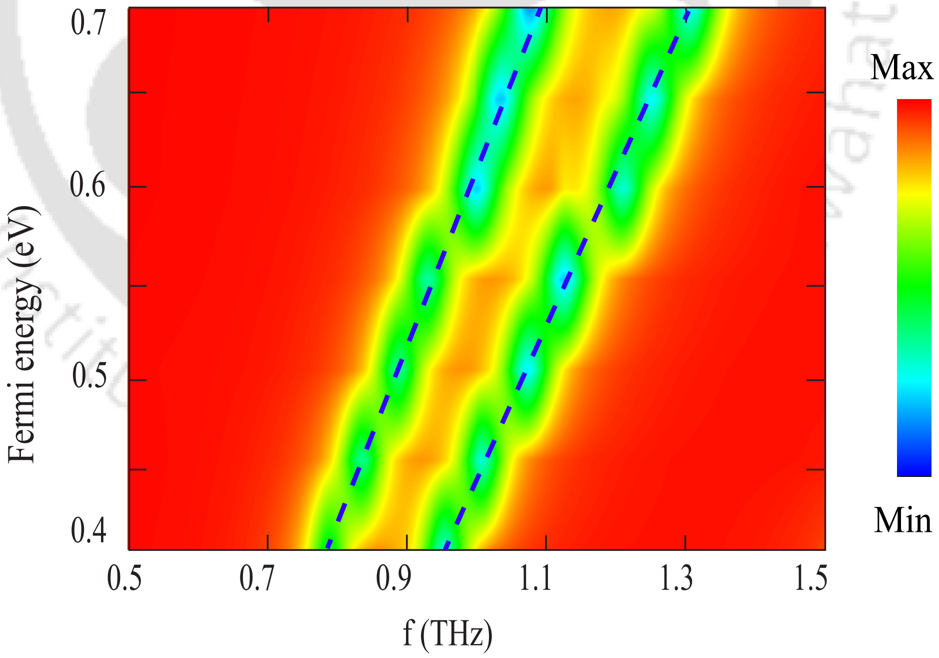

Figure 3.4: Contour plot of the transmittance of the graphene MM structure by varying the Fermi energy, E_f of graphene layer from 0.4 eV to 0.7 eV, with fixed value of vertical displacement, $s = 11\ \mu m$ and horizontal displacement, $d = 1.5\ \mu m$.

Further, to investigate the tunability of the PIT effect in our proposed near-field coupled graphene MM, the transmission characteristics were studied by varying the Fermi energy "E_f" of the graphene layer. Figure 3.4 represents the contour plot of the transmittance of the graphene MM structure for different values of E_f. When $E_f = 0.4$ eV, the PIT peak frequency is observed at $f_r = 0.87\ THz$. As the Fermi energy is increased gradually from 0.4 eV to 0.7 eV, the PIT peak frequency increases, finally reaching a value of $f_r = 1.2\ THz$. It is evident from the figure that the PIT window exhibits a blue shift with the increase of the Fermi energy. It may be worthwhile to mention that the resonance frequency of the graphene layer strongly depends upon the Fermi energy by the relation, $f_r \propto \sqrt{E_f}$ [173–176]. This dependence of the peak frequency on the Fermi energy is clearly observed in our numerical results. Hence, an efficient tuning of the PIT effect of the MM structure, without altering the geometrical parameters, can be achieved by tuning the Fermi energy of the graphene layer. This opens up the possibility of realizing reconfigurable or active MMs based on graphene structures.

3.4 Analytical model for the PIT effect

In order to better understand the physics of the PIT effect in the graphene MMs, the three-level plasmonic model [73, 105, 107] is employed. The model consists of a bright plasmonic state, which strongly couples with the incident field and a dark plasmonic state which does not couple to the incident terahertz beam. We assume the bright mode and dark mode to have nearly same resonances, i.e., ω_1 and ω_2, respectively. The field amplitude of the bright and dark modes can be expressed as

$$\frac{da_1}{dt} = -i(\omega-\omega_1+i\gamma_1)a_1 - i\kappa a_2 - ig_1E, \tag{3.2a}$$

$$\frac{da_2}{dt} = -i\kappa a_1 - i(\omega-\omega_2+i\gamma_2)a_2, \tag{3.2b}$$

where γ_1, γ_2 are the damping factors of the bright and the dark modes, respectively. ω is the incident frequency, κ is the coupling coefficient between the bright and the dark modes while g_1 is a parameter describing the coupling between the incident light and the bright resonator. Under steady state approximation, Eq.3.2 reduces to

$$(\omega-\omega_1+i\gamma_1)a_1 + \kappa a_2 = -g_1E, \tag{3.3a}$$

$$(\omega-\omega_2+i\gamma_2)a_2 + \kappa a_1 = 0. \tag{3.3b}$$

By solving the Eq.3.3, we obtain

$$a_1 = \frac{-g_1 E}{\left[(\omega - \omega_1 + i\gamma_1) - \frac{\kappa^2}{(\omega - \omega_2 + i\gamma_2)}\right]}. \tag{3.4}$$

Then, the transmission of the graphene MM can be expressed using $t(\omega) = 1 - |a_1/E|^2$ as follows:

$$t(\omega) = 1 - \left| \frac{g_1(\omega - \omega_2 + i\gamma_2)}{\kappa^2 - (\omega - \omega_1 + i\gamma_1)(\omega - \omega_2 + i\gamma_2)} \right|^2. \tag{3.5}$$

The theoretical fitting of the square of the transmission represented by Eq.3.5 for different values of "s" and "d" are shown in Figs. 3.5(a) and 3.5(b), respectively. The parameters for the theoretical fitting for different values of "s" and "d" are given in table 3.1 and table 3.2 , respectively.

Table 3.1: Parameters for the theoretical fit for various "s".

s (μm)	g_1 (THz)	γ_1 (THz)	γ_2 (THz)	κ (THz)
0	0.2	0.28	0.15	0.05
4	0.2	0.205	0.35	0.25
6	0.2	0.15	0.36	0.31
8	0.2	0.12	0.37	0.36
11	0.2	0.105	0.38	0.42

Table 3.2: Parameters for the theoretical fit for various "d".

d (μm)	g_1 (THz)	γ_1 (THz)	γ_2 (THz)	κ (THz)
0.5	0.21	0.012	0.45	0.7
1	0.21	0.045	0.43	0.54
1.5	0.21	0.11	0.36	0.42
2.5	0.21	0.145	0.34	0.34
3.5	0.21	0.185	0.33	0.26

The geometrical parameter $g_1 = 0.2$ or 0.21 is same for all the values of "s" and "d", representing a constant free space coupling between the bright mode resonator and electric field of the incident linearly polarized terahertz beam. γ_1 gradually decreases for variation of s from 0 μm to 11 μm, whereas it increases for variation of d from 0.5 μm to 3.5 μm. γ_2 increases for variation of s from 0 μm to 11 μm and decreases for variation

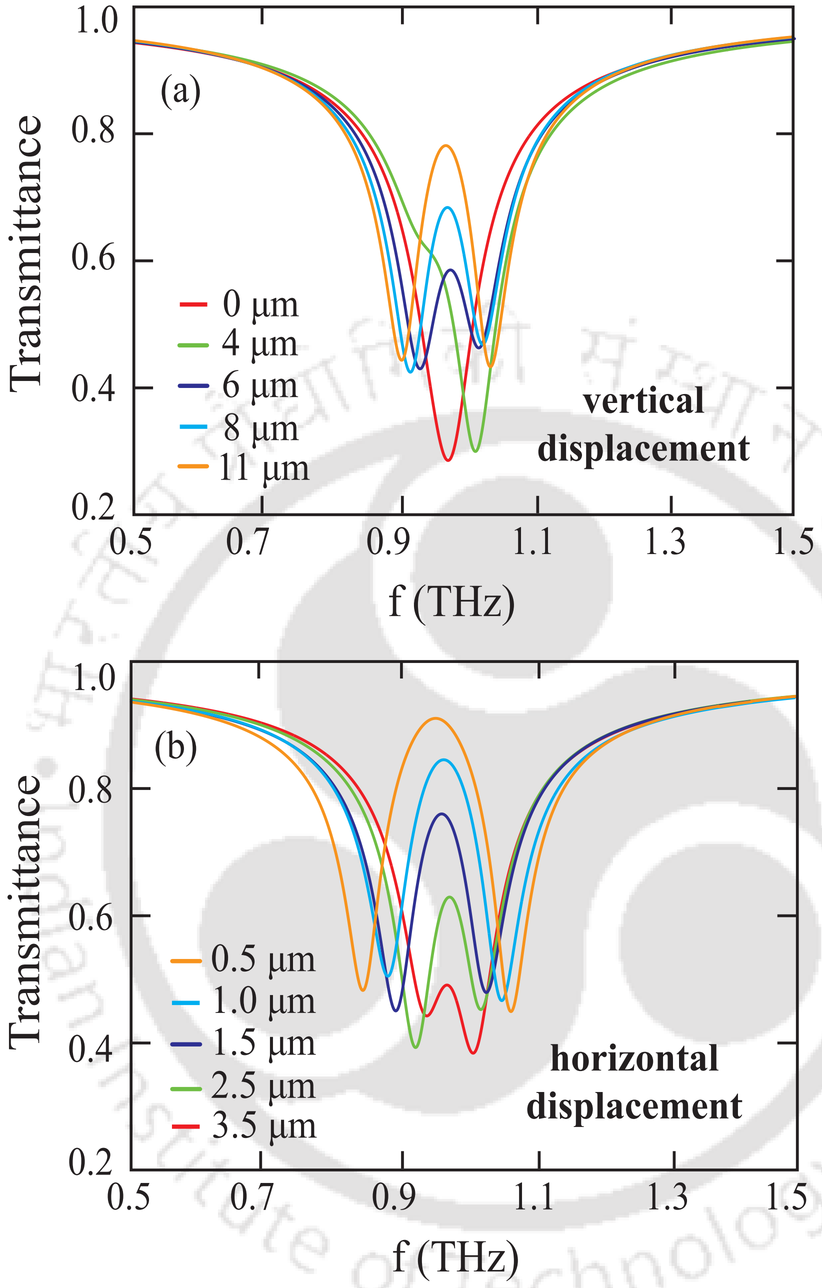

Figure 3.5: Theoretically fitted transmittance of the graphene MM structure (a) for different values of "s" with a fixed value of $d = 1.5\ \mu m$, and (b) different values of "d" with a fixed value of $s = 11\ \mu m$.

of d from 0.5 μm to 3.5 μm. As "s" increases from 0 μm to 11 μm, κ gradually increases indicating an increase in the coupling between the bright and the dark mode of the graphene MM, which results in the widening of the PIT window (Fig. 3.5(a)). κ reduces steadily as "d" increases indicating a reduction of coupling between the bright and the dark mode resulting in the narrowing of the PIT window (Fig. 3.5(b)). The theoretical transmission results are in good agreement with our numerical results.

3.5 Conclusions

In conclusion, the plasmon-induced transparency effect in a near-field coupled metamaterial comprising of a graphene strip and a pair of graphene split ring resonators is numerically and theoretically analyzed. The plasmon-induced transparency effect is modulated by varying the vertical displacement as well as horizontal displacement of the split ring resonators w.r.t. the graphene strip. As the graphene SRRs are displaced in the vertical direction, the PIT effect vanishes when the centers of both graphene SRRs and the graphene strip are collinear to each other. When the graphene SRRs are displaced in the horizontal direction, the PIT window becomes narrower due to reduced coupling between the dark and bright modes. Further, the PIT effect is studied for different values of Fermi energy of the graphene material. The PIT window exhibits a blue shift as the Fermi energy gradually increases from 0.4 eV to 0.7 eV. Finally, a theoretical model based on the three-level plasmonic system is provided in order to validate our numerical findings. The theoretical results are in good agreement with the numerical results. This study can be significant in designing frequency tunable, active and reconfigurable terahertz metamaterials in near future.

CHAPTER 4

DUAL-BAND ELECTROMAGNETICALLY INDUCED TRANSPARENCY IN A TERAHERTZ METAMATERIAL

4.1 Introduction

As discussed in the previous chapters, the EIT effect in terahertz MMs has become a prevalent area of research, owing to its numerous applications which is possible due to the presence of a tunable transparency window [94, 99, 103, 140, 141, 150–152, 157, 165, 169]. This has led to a considerable interest in realizing the dual-band EIT effect in MM structures through the careful arrangements of the resonators. In this phenomenon, two tunable transparency windows are induced as a result of the net coupling between the bright-dark-dark modes or bright-bright-dark modes of the constituent MM structures [114, 115, 153–155, 179]. Different MM configurations comprising of metal strips, split ring resonators, hybrid structures, [114, 115, 153–155, 179], etc. have been investigated for the realization of this effect. In terahertz regime, the dual-band EIT effect has been examined in a MM comprising of a central metal strip coupled to a split ring resonator (SRR) and a two-gap SRR [114]. The dual-band EIT effect and slow light behavior has also been studied in a MM structure

---

The results of the work reported in this chapter has been published in *J. Appl. Phys.*, vol. **124**, year 2018, pages 063106-063113; title: “Dual-band electromagnetically induced transparency effect in a concentrically coupled asymmetric terahertz metamaterial”; authors: Koijam Monika Devi, Dibakar Roy Chowdhury, Gagan Kumar and Amarendra K. Sarma.

comprising of three coupled meta-atoms [114], for a wide range of oblique incident angles, wherein the effect has been achieved through the simultaneous interactions of the bright mode, dark mode and quasi-dark mode. In another recent study, Xu *et al.* [115] have demonstrated the dual-band EIT effect through symmetry breaking in a terahertz MM structure comprising of two concentric square SRRs with their gaps aligned parallel to each other. Recently, the dual-band EIT phenomenon has managed to attract a lot of attention due to its potential in realizing multiband slow light systems [114, 155, 179], narrowband absorbers [115], etc. as a result of the double tunable transparency windows associated with the effect. In-spite of the significant interest, only limited amount of work has been reported to investigate and explore the applications of this effect. As such, there is ample scope to explore the dual-band EIT effect in MMs, in order to achieve an effective modulation of the transparency windows as well as to thoroughly understand the underlying physical mechanisms causing the effect.

In this chapter, we examine dual-band EIT effect in a simple terahertz MM geometry comprising of an inner CSRR concentrically coupled to an outer asymmetric two-gap circular split ring resonator (ASRR). The dual-band EIT effect in the proposed MM configuration occurs due to the coupling of the resonant mode of the CSRR structure to the EIT response of the ASRR structure. It may be noted that the effect in the proposed MM occurs due to the coupling of two meta-atoms (i.e., the CSRR and the ASRR), as opposed to earlier studies [114], where the effect occurs as a result of the coupling between three meta-atoms. Although, the dual-band EIT effect has been studied earlier, the novelty of our work lies in the modulation of the transparency windows through the rotation of the CSRR in the proposed MM structure. The circular structure of our proposed MM configuration provides an extra degree of freedom in controlling the dual-band EIT effect arising in the structure. The dual-band EIT effect diminishes with an increase in the rotation angle of the CSRR and finally vanishes with an orthogonal rotation of the CSRR. Modulation of the effect is further achieved by varying the asymmetry in the ASRR and the size of the CSRR in the proposed MM structure. A theoretical model based on a Four-Level Tripod (FLT) system clearly elucidates the coupling mechanism in the MM structure. The design, numerical results and theoretical model are discussed in the subsequent sections followed by a brief conclusion.

4.2 Design and numerical simulations

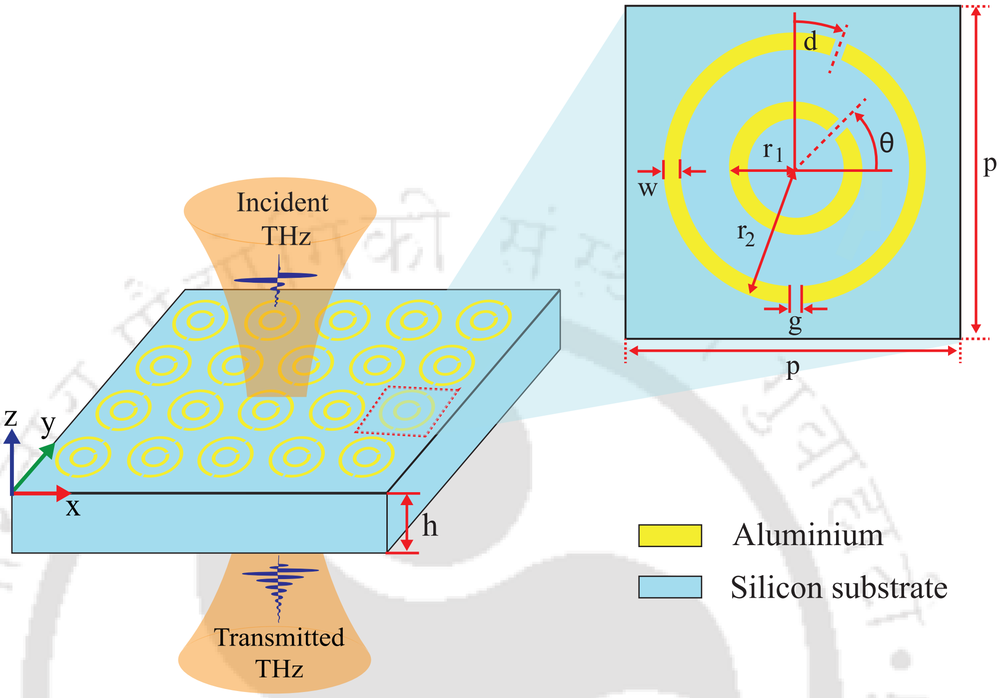

Figure 4.1: Schematic illustration for the study of the dual-band EIT effect in a planar terahertz MM geometry along with the meta-molecule comprising of an inner CSRR concentrically coupled to an ASRR.

The schematic diagram of the proposed asymmetric terahertz MM structure is illustrated in Fig. 4.1. The meta-molecule of the MM structure comprises of an outer ASRR placed concentrically with respect to an inner CSRR. The ASRR and CSRR structures, made of aluminium metal having a thickness of 200 nm, are placed on a silicon substrate of thickness $h = 10\ \mu m$, with a dielectric permittivity of 11.9. The periodicity of the MM structure is taken as $p = 80\ \mu m$. The outer radius of the CSRR and the ASRR are denoted by r_1 and r_2, respectively. 'g' represents the split gaps of the ASRR and the CSRR while 'w' represents the width of both resonators. 'θ' denotes the rotation angle of the CSRR with respect to the incident polarization, while 'd' is the asymmetry parameter of the ASRR. The parameters $r_2 = 29\ \mu m$, $g = 3\ \mu m$, $w = 5\ \mu m$ are fixed for all the numerical simulations. The numerical simulations have been performed using the finite difference frequency domain solver in CST Microwave Studio. The MM structure is simulated under unit cell boundary conditions in the x-y plane. An adaptive mesh size of the order of $\lambda/10$, where λ is the wavelength of the incident radiation, is employed. Open

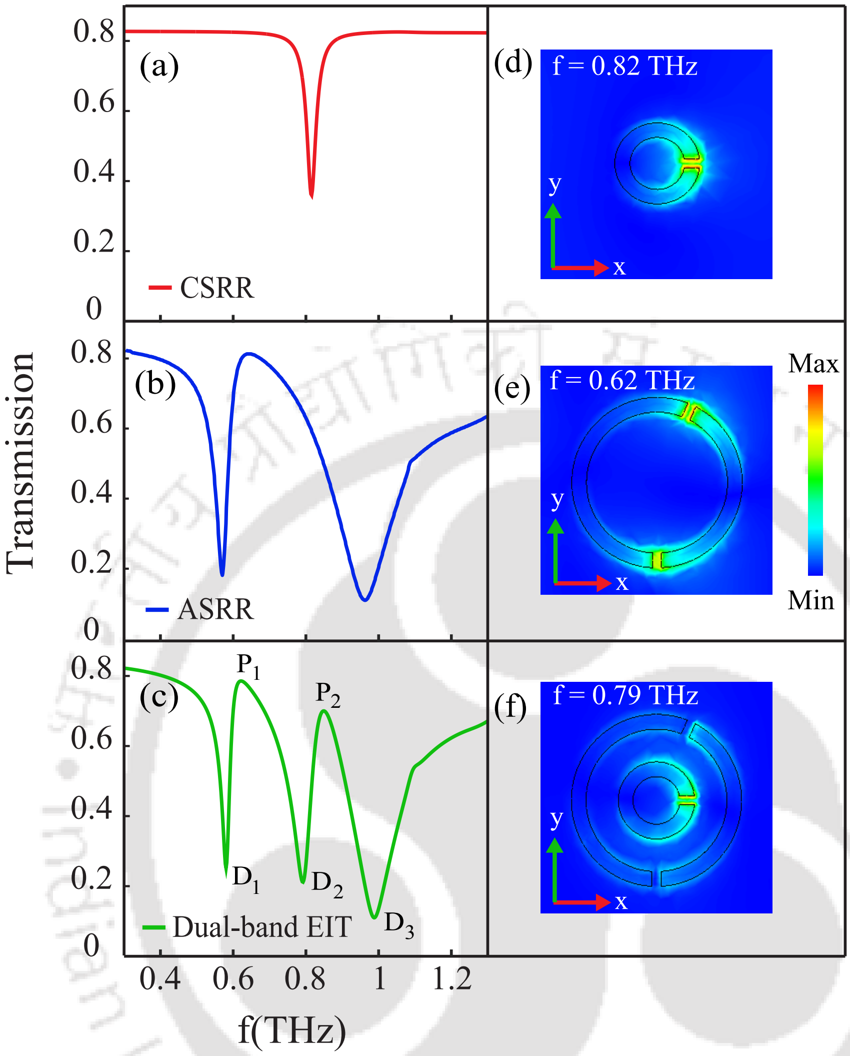

Figure 4.2: Terahertz transmission profile vs. frequency for (a) CSRR with $\theta = 0^o$ and $r_1 = 13\ \mu m$, (b) ASRR with $d = 12\ \mu m$ and (c) the coupled MM configuration for fixed values of $\theta = 0^o$, $d = 12\ \mu m$ and $r_1 = 13\ \mu m$. Electric field profiles of (d) the CSRR structures at the resonance frequency, (e) the ASRR structures at the transmission peak, and (f) the dual-band EIT MM structure at the transmission dip D_2. The green arrow signifies the direction of incident polarization.

boundary conditions were set along the direction of light propagation. The simulations are performed for the y-polarized incident terahertz wave.

The terahertz transmission response of the CSRR structure, ASRR structure and the coupled MM structure for the y-polarized incident terahertz waves are shown in Figs. 4.2(a)-(c). Figure 4.2(a) represents the transmission of the CSRR structure at $\theta = 0^o$ and $r_1 = 13\ \mu m$. It is evident from the figure that the CSRR gets excited by the linearly polarized terahertz beam and has a narrow resonance dip at a frequency, $f = 0.82\ THz$.

On the other hand, the ASRR structure exhibits an EIT-like transmission profile having a transparency window from 0.6 THz to 0.81 THz with a transmission peak frequency, $f = 0.62$ THz. The transmission profile for the ASRR structures with $d = 12$ μm, is shown in Fig. 4.2(b). When the CSRR is placed concentrically to the ASRR structure, the single transparency window of the ASRR structure splits into two transparency windows with the first transparency window ranging from 0.59 THz to 0.75 THz and the second transparency window ranging from 0.82 THz to 0.93 THz. This dual-band EIT effect occurs due to the coupling of the CSRR resonances to the EIT effect of the ASRR structures in the coupled MM structure. The terahertz transmission response of the MM for $\theta = 0^o$, $d = 12$ μm and $r_1 = 13$ μm is represented by the green solid line in Fig. 4.2(c).To further understand the coupling behavior leading to the dual-band EIT effect, we also observe the electric field profiles of the structural components of the MM structure. Figures 4.2(d)-(f) represent the electric field profiles of the CSRR, ASRR and the coupled MM structure, respectively. Figure 4.2(d) describes the electric field profile for the CSRR structures, at the resonance frequency, when its gap is parallel to the direction of the incident polarization. We may note from the figure, that the electric field in the CSRR structure is strongly confined to its gap for this configuration, which indicates the excitation of an LC resonance in the CSRR structure. The ASRR structure exhibits a single transparency EIT-like effect due to the coupling of the resonances arising from the two arms of the ASRR [180]. The electric field profile of the ASRR structures at the transmission peak P_1 is shown in Fig. 4.2(e). When the resonant mode of the CSRR is made to couple with the EIT effect of the ASRR, a transmission dip D_2 arises within the transparency window. Hence, a dual-band EIT effect is achieved in the coupled MM structure. The electric field profile for the corresponding structure at the transmission dip D_2 (i.e., $f = 0.79$ THz) is shown in Fig. 4.2(f).

4.3 Results and Discussions

The transmission characteristics of the proposed MM are studied for different rotation angle of the CSRR with respect to the incident polarization. Figure 4.3(a) represents the dual-band EIT of the proposed MM for a fixed $r_1 = 13$ μm and $d = 12$ μm by varying θ from 0^o to 90^o. The red solid line represents the transmission of the MM structure when $\theta = 0^o$. The green line represents transmission for $\theta = 20^o$ while the blue traces signify the transmission for $\theta = 40^o$. The cyan and the orange traces represent the transmission

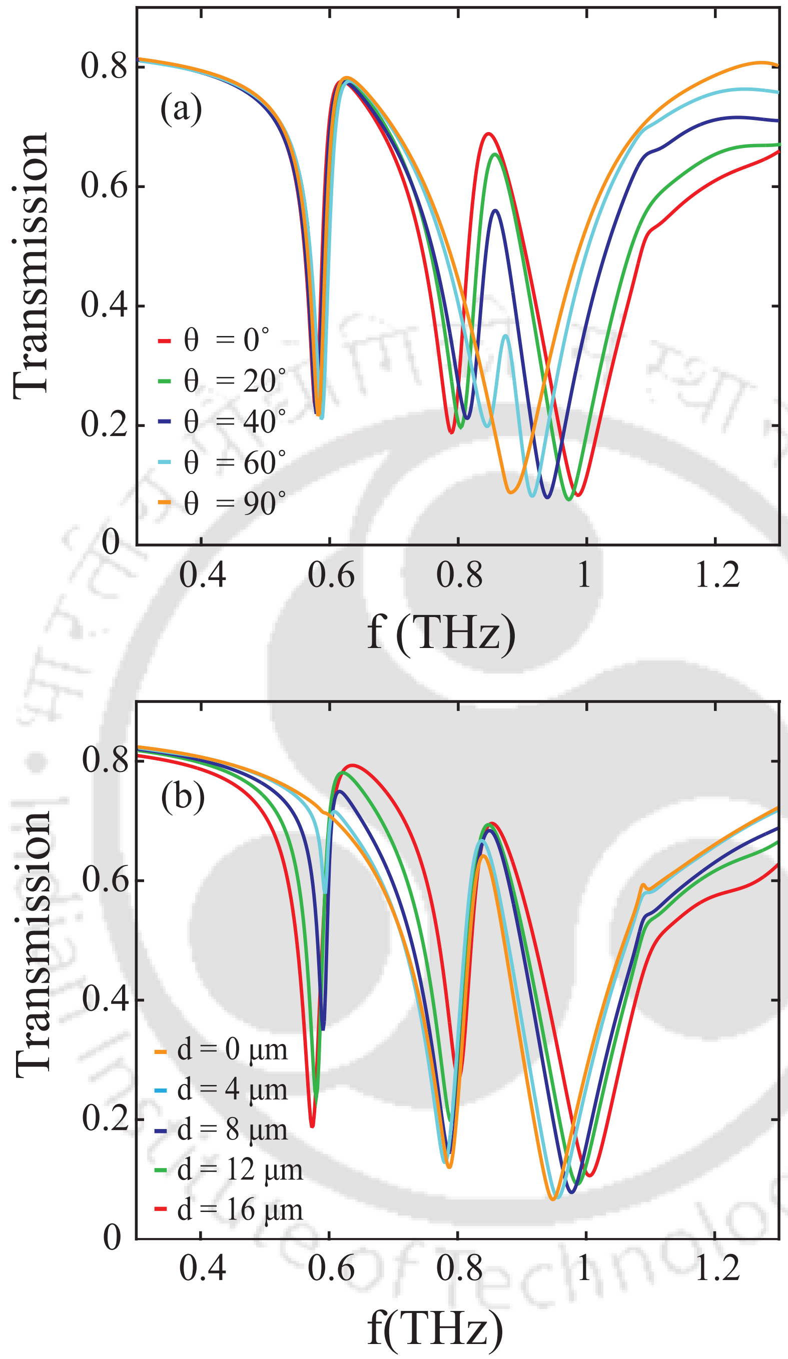

Figure 4.3: Terahertz transmission vs. frequency for (a) different values of rotation angle θ, and (b) different values of the asymmetry parameter d of the proposed MM geometry. The size of the inner CSRR is fixed at $r_1 = 13\ \mu m$ in both cases.

of the MM structure for $\theta = 60^o$ and $\theta = 90^o$, respectively. It is clearly evident from the figure that the dual-band EIT effect is most prominent for $\theta = 0^o$. The dual-band EIT effect diminishes as the inner CSRR is rotated w.r.t incident polarization. When

$\theta = 90^o$, the dual-band EIT effect vanishes in the MM structure. Hence, one can switch the dual-band EIT effect to a single EIT effect in the coupled MM structure. Modulation of the effect is further achieved by gradually varying the asymmetry of the ASRR, 'd' from 0 μm to 16 μm in the MM structure. The transmission characteristics of the MM structure for different values of 'd' with a fixed $\theta = 0^o$ and $r_1 = 13$ μm is shown in Fig. 4.3(b). The orange solid line represents the transmission for $d = 0$ μm. The cyan traces signify the transmission for $d = 4$ μm. The blue and the green traces represent the transmission of the MM structure for $d = 8$ μm and $d = 12$ μm, respectively. The red line represents the transmission of the MM structure when $d = 16$ μm. It is clearly observed from the figure that a single EIT effect occurs when the asymmetry parameter, $d = 0$ μm. However, the single EIT effect in the MM structure evolves into a dual-band EIT effect with the introduction of asymmetry (i.e., $d > 0$ μm). The dual-band EIT effect is further tuned by increasing the asymmetry of the ASRR in the proposed MM structure.

In order to get insight about the dual-band EIT effect in the MM structure, we study the electric field profiles for various rotation angle and asymmetry parameters. Figure 4.4(a)-(c) represents the electric field profiles of the MM geometry at the transmission peak P_2 of the second transparency window for $\theta = 0^o$, 40^o and 90^o, with $r_1 = 13$ μm and $d = 12$ μm fixed. It is evident from Fig. 4.4(a), that the CSRR is excited by the incident terahertz radiation when $\theta = 0^o$. In this case, the gap of the CSRR is parallel to the direction of the incident polarization resulting in an LC resonance dip at $f = 0.82$ THz (see Fig. 4.2(a)). The coupled MM structure exhibits a dual-band EIT effect for this configuration, due to the coupling of the resonant modes of the CSRR and the ASRR structures. However, as we rotate the CSRR w.r.t incident polarization, the near field coupling behavior of the MM structure is modified. The electric field profile for $\theta = 40^o$ is shown in Fig. 4.4(b). The CSRR is weakly excited by the incident terahertz radiation which results in the diminishing of the dual-band EIT effect in the MM structure. Finally, for $\theta = 90^o$, i.e., when the gap of the CSRR is perpendicular to the incident polarization, the LC resonance in the CSRR is no longer excited. With this right-angled rotation, an on-to-off resonance of the CSRR is created in the MM structure. For this configuration, the dual-band EIT effect reduces to a single EIT effect in the coupled MM structure. The electric field profile for the corresponding MM configuration is shown in Fig. 4.4(c). Hence, an efficient tuning of the dual band EIT effect is achieved as a result of this on-to-off resonance of the CSRR. Figure 4.4(d)-(f) represents the electric field profiles

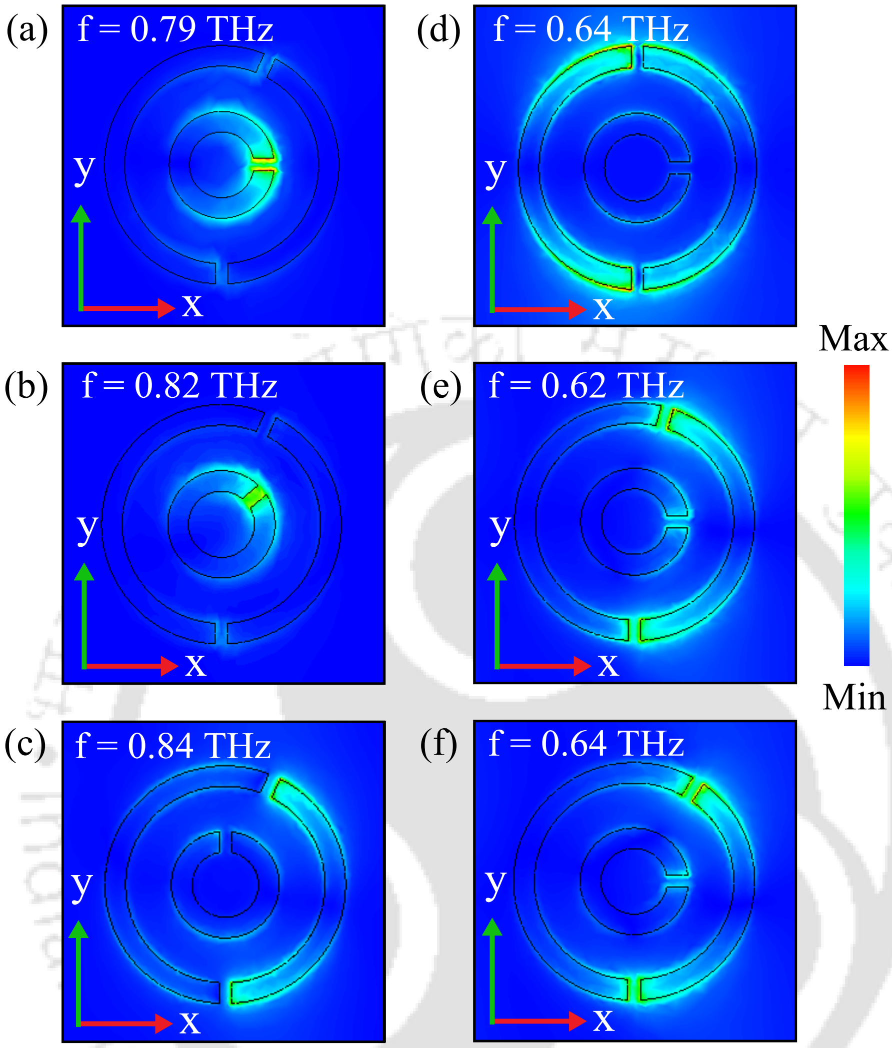

Figure 4.4: Electric field profile of the MM structure at P_2 for different rotation parameters i.e., (a) $\theta = 0^o$, (b) $\theta = 40^o$ and (d) $\theta = 90^o$ or a fixed value of $r_1 = 13\ \mu m$ and $d = 12\ \mu m$. Electric field profile of the MM structure at P_1 for different asymmetry parameters i.e., (d) $d = 0\ \mu m$, (e) $d = 8\ \mu m$ and (f) $d = 16\ \mu m$ for a fixed value of $r_1 = 13\ \mu m$ and $\theta = 0^o$. The incident electric field is along the direction of the green arrow.

of the MM structure at the transmission peak P_1 of the first transparency window for $d = 0\ \mu m$, 8 μm and 16 μm with a fixed value of $r_1 = 13\ \mu m$ and $\theta = 0^o$. The electric field profile, at P_1, corresponding to $d = 0\ \mu m$ is shown in Fig. 4(d). For $d = 0\ \mu m$, the outer ASRR is a symmetric two-gap split ring resonator (SRR). It is evident from the figure that the symmetric two-gap SRR is excited by the incident electric field. The symmetric two-gap SRR has broad dipolar resonance [180] at a frequency close to that of the CSRR. This dipolar resonance of the symmetric two-gap SRR, when coupled to

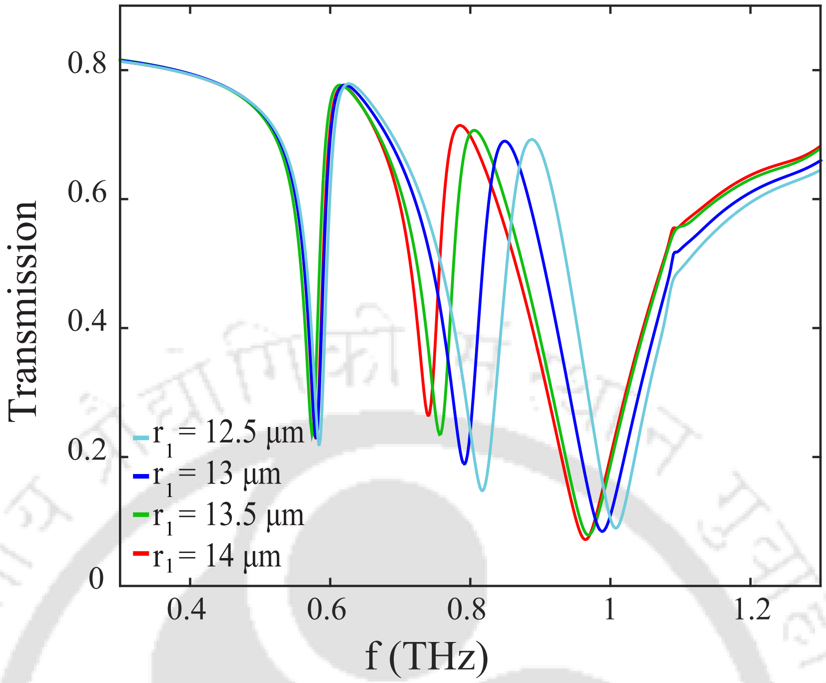

Figure 4.5: Terahertz transmission vs. frequency by varying the size of the inner CSRR, r_1 from 12.5 μm to 14 μm. The values of the rotation parameter and the asymmetry parameter is fixed at $\theta = 0$ and $d = 12$ μm, respectively.

the LC resonance of the CSRR, generates a transparency window leading to a single transparency EIT effect in the coupled MM structure. By introducing an asymmetry in the symmetric two-gap SRR, which then becomes ASRR, the dual-band EIT effect can be realized in the coupled MM structure. The symmetry breaking in the MM structure causes a difference in the resonance frequencies of the two metallic arms giving rise to an EIT response for the ASRR structures. Figure 4.4(e) represents the electric field profile corresponding to $d = 8$ μm. In this case, the ASRR structures exhibit an EIT like response due to the breaking of symmetry in the resonant mode. Consequently, the coupling of the ASRR with the CSRR structure leads to the realization of a dual-band EIT effect in the coupled MM structure. The effect can be further tuned by increasing the asymmetry of the ASRR structure. The electric field profile corresponding to $d = 16$ μm is shown in Fig. 4.4(f). It is observed that the dual-band EIT effect in the coupled MM structure is most pronounced for this configuration. Therefore, an effective tuning of the dual-band EIT effect is achieved in the MM structure.

Further modulation of the dual-band EIT effect in the proposed MM structure is achieved by varying the size of the inner CSRR, 'r_1' from 12.5 μm to 14 μm. The terahertz

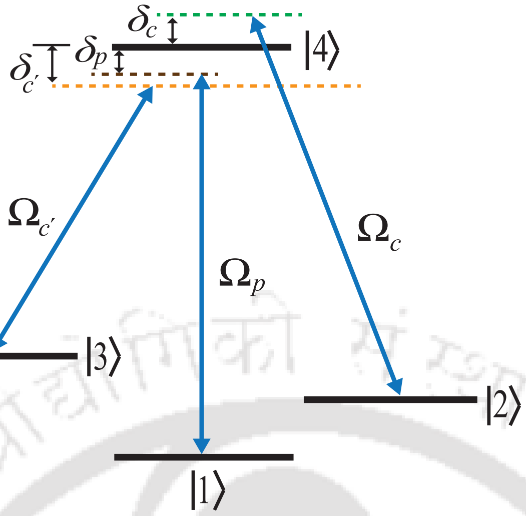

Figure 4.6: Energy level diagram of the FLT-system driven by three light fields Ω_p, Ω_c , $\Omega_{c'}$ with corresponding frequency detunings δ_p, δ_c, $\delta_{c'}$, respectively.

transmission profile for different values of r_1 with a fixed $\theta = 0^o$ and $d = 12\ \mu m$, is shown in Fig. 4.5. The cyan solid line represents the transmission of the MM structure when $r_1 = 12.5\ \mu m$. The blue line represents transmission for $r_1 = 13\ \mu m$, while the green traces signify the transmission for $r_1 = 13.5\ \mu m$. The red traces represent the transmission of the MM structure when $r_1 = 14\ \mu m$. When $r_1 = 12.5\ \mu m$, the resonance dip of the individual CSRR structure occurs at $f = 0.85\ THz$. As r_1 is increased gradually, the resonance frequency of the inner CSRR decreases steadily reaching a value of $0.76\ THz$ when $r_1 = 14\ \mu m$. Hence, the dip D_2 in the dual-band EIT effect experiences a blue shift with the increase of r_1 in the MM configuration, resulting in the red shifting of the second transparency region as well. This further adds another degree of freedom to the tuning capability of the dual-band EIT effect in the proposed MM structure.

4.4 Analytical model based on the four-level tripod (FLT) system

In order to validate our numerical findings and to better understand the dual-band EIT effect in the MM structure, a four-level tripod (FLT)-system is employed [77, 115]. The energy level diagram for the FLT-system is illustrated in Fig. 4.6. In the system, the transition between $|1\rangle \rightarrow |4\rangle$, driven by the Rabi frequency, Ω_p is termed as the probe/dark transition while the transition between $|2\rangle \rightarrow |4\rangle$, driven by the Rabi frequency, Ω_c is termed as the coupling/bright transition. The levels $|1\rangle$, $|2\rangle$ and $|4\rangle$ constitute a Λ-system exhibiting an EIT effect as a result of the destructive interference between the excitation pathways $|1\rangle \rightarrow |4\rangle$ and $|1\rangle \rightarrow |4\rangle \rightarrow |2\rangle \rightarrow |4\rangle$. With the introduction of another dark/control state $|3\rangle$, this Λ-system evolves into an FLT-system, exhibiting a dual-band EIT effect. This is because the destructive interference has changed into a constructive interference between the EIT effect of the Λ-system and the dark/control state. In our proposed MM structure, the outer symmetric two-gap SRR (corresponding to $d = 0\ \mu m$) behaves as the bright state with a broad dipolar resonance. One dark state is introduced by breaking the symmetry in the outer symmetric SRR (corresponding to $d > 0\ \mu m$), as a result of which, the outer ASRR represents a Λ-system. Another dark state is introduced by placing the inner CSRR concentrically to the ASRR in the MM structure. The coupling between the ASRR and the CSRR structure leads to the evolution of the proposed MM structure into an analog of the FLT-system.

The equation of motion of the FLT-system could be expressed as follows:

$$\frac{d\rho_{21}}{dt} = -[\gamma_{21} - i(\delta_p - \delta_c)]\rho_{21} + \frac{i}{2}\Omega_c{}^*\rho_{41} \tag{4.1a}$$

$$\frac{d\rho_{31}}{dt} = -[\gamma_{31} - i(\delta_p - \delta_{c'})]\rho_{31} + \frac{i}{2}\Omega_{c'}{}^*\rho_{41} \tag{4.1b}$$

$$\frac{d\rho_{41}}{dt} = -[\gamma_{41} - i\delta_p]\rho_{41} + \frac{i}{2}(\Omega_p + \Omega_c\rho_{21} + \Omega_{c'}\rho_{31}) \tag{4.1c}$$

where ρ_{j1} is the off-diagonal density matrix element for the transition $|j\rangle \rightarrow |1\rangle$ ($|j\rangle = |2\rangle$, $|3\rangle$, $|4\rangle$) and γ_{j1} ($j = 2,\ 3,\ 4$) is the decay rates for the transition from $|j\rangle \rightarrow |1\rangle$. The corresponding frequency detunings are defined as $\delta_p = \omega_p - \omega_{41}$, $\delta_c = \omega_c - \omega_{21}$ and $\delta_{c'} = \omega_{c'} - \omega_{31}$, where ω_{21}, ω_{31} and ω_{41} denote the energy-level transition frequencies. ω is the incident frequency and ω_p, ω_c and $\omega_{c'}$ are respectively, the resonant frequencies of the probe, the coupling and the control fields. For a steady state, Eq.(4.1) reduces to

$$\rho_{21} = \frac{i\Omega_c{}^*\rho_{41}}{2[\gamma_{21} - i(\delta_p - \delta_c)]} \tag{4.2a}$$

$$\rho_{31} = \frac{i\Omega_{c'}{}^*\rho_{41}}{2[\gamma_{31} - i(\delta_p - \delta_{c'})]} \tag{4.2b}$$

$$\rho_{41} = \frac{i(\Omega_p + \Omega_c\rho_{21} + \Omega_{c'}\rho_{31})}{2[\gamma_{41} - i\delta_p]} \tag{4.2c}$$

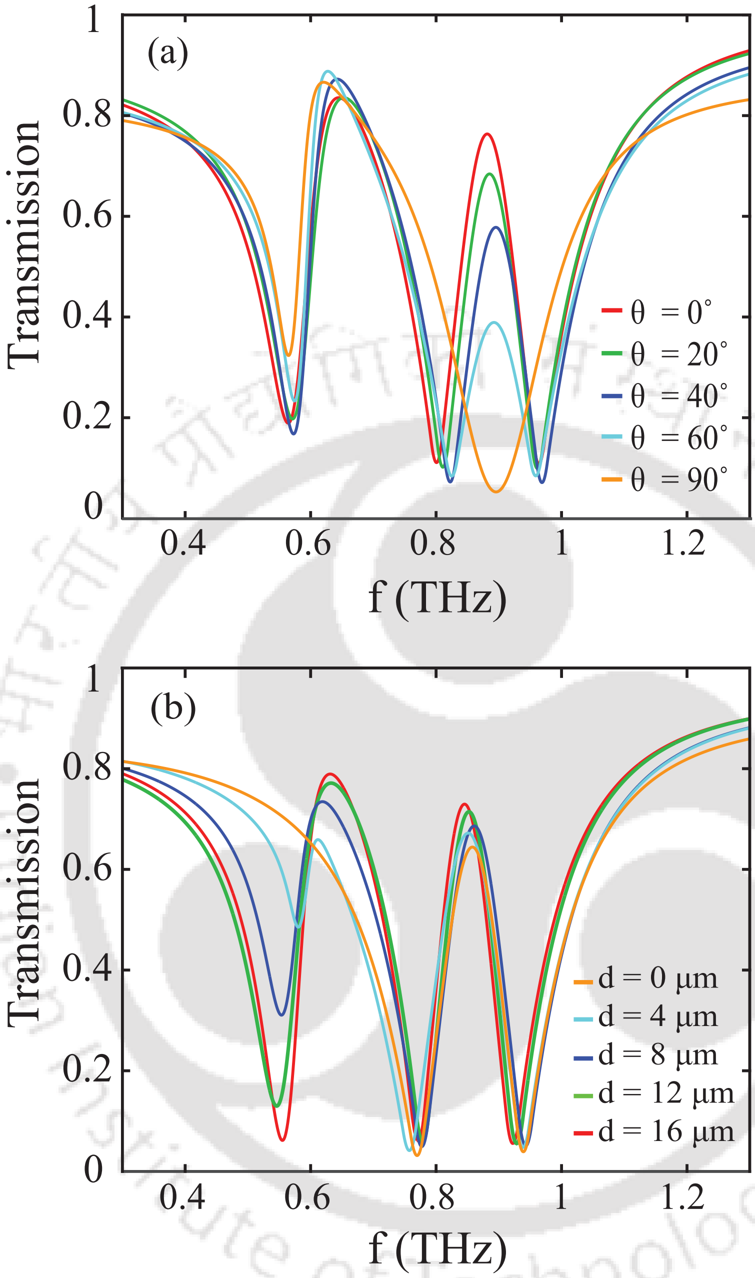

Figure 4.7: Theoretically fitted transmission for (a) different values of rotation angle θ, with fixed $d = 12\ \mu m$, $r_1 = 13\ \mu m$, and (b) different values of the asymmetry parameter 'd'', with fixed values $\theta = 0^o$ and $r_1 = 13\ \mu m$ of the proposed MM geometry.

Then, from Eq.(4.2), one can obtain the exact solution of ρ_{41} as

$$\rho_{41} = \frac{-\Omega_p}{\left[2\left(i\gamma_{41} + \delta_p\right) - \frac{|\Omega_c|^2}{2\left(i\gamma_{21}+\delta_p-\delta_c\right)} - \frac{|\Omega_{c'}|^2}{2\left(i\gamma_{31}+\delta_p-\delta_{c'}\right)}\right]} \tag{4.3}$$

The transmission amplitude for the FLT-system is given by the expression, $t(\omega) = 1 - Im(\rho_{41})$ as

$$t(\omega) = 1 - Im\left[\frac{-\Omega_p}{2\left(i\gamma_{41} + \delta_p\right) - \frac{|\Omega_c|^2}{2\left(i\gamma_{21}+\delta_p-\delta_c\right)} - \frac{|\Omega_{c'}|^2}{2\left(i\gamma_{31}+\delta_p-\delta_{c'}\right)}}\right] \tag{4.4}$$

Using the expression given by Eq.(4.4).and through carefully tuning the Rabi frequencies and the decay rates of each transition, we can obtain a theoretical fit of the numerically simulated transmission. The theoretically fitted transmission for the FLT-system, shown in Fig. 4.7, are in good agreement with our numerical results represented in Fig. 4.3. When $d > 0\ \mu m$, the ASRR structure behaves as an analog of a Λ-system. In this case, the rotation of the CSRR structure acts as the dark/control field giving rise to the dual-band EIT effect in the FLT-system. This control field evolves due to the in-plane rotation of the CSRR in the MM structure which in turn modifies the coupling behavior in the FLT-system. This results in the diminishing of the dual-band EIT-like effect in the MM structure. Finally, for an orthogonal rotation of the CSRR, the dual-band EIT effect reduces into a single EIT effect (as represented by the orange line in Fig. 4.7(a)) in our proposed MM. For this configuration, the FLT-system behaves as if the dark/control state is absent, reducing to a Λ-system. On the other hand, the Λ-system evolves into a FLT-system when the asymmetry in the ASRR is varied. The asymmetry parameter, in this case, acts as the dark/control state of the FLT-system. Figure 4.7(b) represents the transmission for different values of asymmetry parameter with fixed values of θ and r_1. When $d = 0\ \mu m$, the ASRR to the CSRR structure acts as the Λ-system. When the asymmetry is introduced in the ASRR structure, this Λ-system evolves into the FLT-system. With the help of these two control parameters, an effective tuning of the dual-band EIT effect is achieved in the proposed MM structure.

4.5 Conclusions

The dual-band EIT effect in a terahertz MM comprising of an inner circular split ring resonator (CSRR) concentrically coupled to an outer asymmetric two-gap split ring resonator (ASRR) is numerically and theoretically analyzed. The proposed MM structure exhibits the effect as a result of coupling between the resonant mode of the CSRR and the EIT response of the ASRR. The coupling behavior in the MM is modified through an in-plane rotation of the CSRR structures. A gradual orthogonal rotation of the CSRR leads to the vanishing of the dual-band EIT effect in the MM. Modulation of the effect is further achieved by gradually varying the asymmetry of the outer ASRR as well as the size of the inner CSRR. A theoretical model based on a Four Level Tripod system elucidates the coupling behavior in the proposed MM geometry. This study can be significant in realizing multi-band slow light devices, narrowband absorbers, switches, etc. in the terahertz regime.

Part-II


भारतीय प्रौद्योगिकी संस्थान गुवाहाटी
Indian Institute of Technology Guwahati

CHAPTER 5

SURFACE POLARITONIC SOLITONS AND BREATHERS IN A PLANAR PLASMONIC WAVEGUIDE STRUCTURE

5.1 Introduction

In the previous chapters, we have discussed the EIT phenomenon in different terahertz MM structures, where the modulation of the transparency window has been achieved either dynamically or by altering the geometrical parameters of the MM structures. In these chapters, we have explored the aspect of the tunable transparency window of the EIT phenomenon in the terahertz MMs [94, 99, 115, 150, 152, 157]. As discussed in section 1.3.2, the EIT phenomenon can also be employed as a means for the excitation of SPs in a prism coupler planar plasmonic structure [76, 77]. A recent theoretical study have also predicted the possibility of a coupler-free excitation of SP resonances in these structures [78]. Currently, such coupler-free scheme is being examined to explore the behavior of the SP waves in the nonlinear regime [95, 96] at the interface of a negative index metamaterial (NIMM) and a four-level EIT medium. In the nonlinear regime, the dynamics of the excited surface plasmons is governed by the so-called nonlinear Schrödinger equation (NLSE), which can assume different exact

---

The results of the work reported in this chapter has been published in *J. Opt. Soc. Am. B*, vol. **36**, year 2019, pages 2160-2166; title: "Surface polaritonic solitons and breathers in a planar plasmonic waveguide structure via electromagnetically induced transparency"; authors: Koijam Monika Devi, Gagan Kumar and Amarendra K. Sarma.

solutions (e.g. solitons and breathers). These nonlinear SP waves inherit the shape preserving properties of solitons [54, 181–183]. Hence, there is a significant potential of such nonlinear SP waves as it can be employed as a means to reduce the propagation loss inherent in SPs. Additionally, the coupler-free scheme can become a promising technique for the development of highly compact nano-optical devices for various applications in the optical regime by overcoming the limitation faced by the prism coupling technique [78]. However, only few studies on coupler-free excitation of the nonlinear SP waves has been reported so far [95, 96, 184]. Therefore, in this chapter, we propose a scheme for the coupler-free excitation of surface polaritonic solitons and breathers in a planar plasmonic waveguide structure comprising of a transparent layer, a metal layer and a three level lambda-type EIT medium. Although, similar study has been performed earlier [95, 96], the nonlinear behavior of the SPs using a coupler-free scheme with a three-level EIT medium has not been investigated. Further, we have used a metal layer in our study (unlike the earlier studies where an NIMM layer is used), as it is more favorable when it comes to practical applications. To the best of our knowledge, the excitation and propagation of the surface polaritonic solitons and breathers remain to be explored in the proposed structure.

First, we discuss the coupler-free excitation of SP resonance in the linear regime in the proposed planar plasmonic waveguide structure. Then, this coupler-free scheme is further examined for investigating the behavior of the excited SP resonances in the nonlinear regime. Here, we explore the nonlinearity aspect associated with the EIT phenomenon to investigate the generation of surface polaritonic solitons and breathers in the proposed structure. It is observed that within the EIT transparency window, a giant Kerr nonlinearity is achieved which can be efficiently controlled through proper modulation of the parameters of the incident fields. A balance between the group velocity dispersion and the Kerr nonlinearity in the system provides the necessary condition for the excitation of nonlinear SP waves. It is observed that the system yields laterally self-trapped surface polaritonic solitons which is tightly guided at the interface of the metal and the EIT medium. Further, we explore the possibility of generating surface polaritonic breathers in the proposed system. We show that the surface polaritonic solitons and breathers can have an undistorted and a stable propagation at the interface of the metal-EIT medium.

5.2 Model

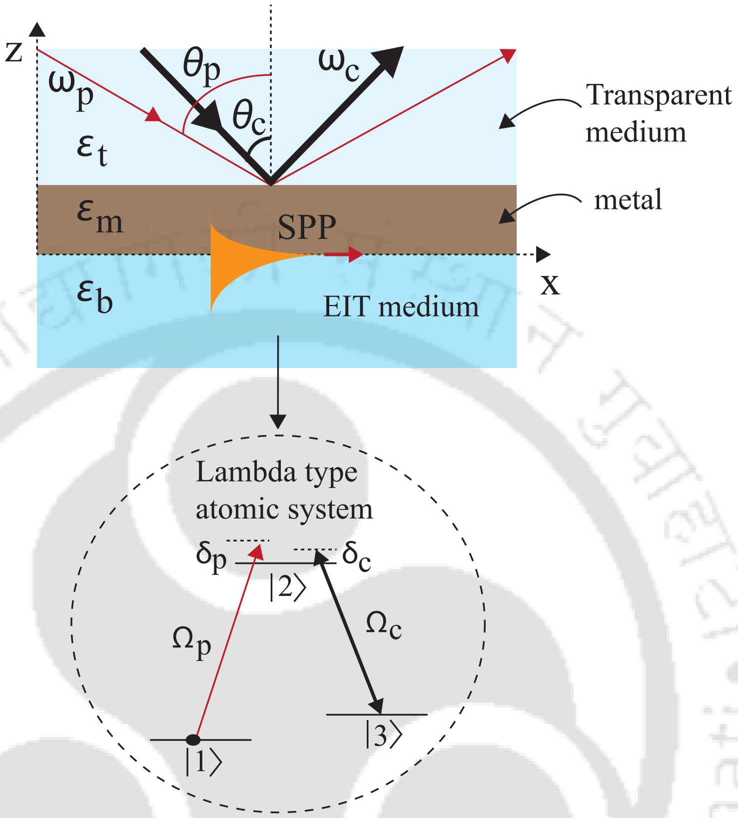

Figure 5.1: Schematic illustration for the excitation of surface polaritonic solitons and breathers in a planar plasmonic waveguide structure based on EIT. A three-level lambda-type atomic medium is considered as the EIT medium in the system. The red arrow indicates the probe field while the black arrow denotes the coupling field.

The schematic diagram of the proposed planar plasmonic waveguide structure based on EIT is illustrated in Fig. 5.1. The structure comprises of three layers namely, a top transparent layer, a middle metal layer and a bottom layer of EIT medium. The top layer is a transparent medium (vacuum or a lossless dielectric) having a refractive index, $n_t = \sqrt{\epsilon_t \mu_t / \epsilon_0 \mu_0} \approx 1$, where ϵ_t and μ_t are the electrical permittivity and magnetic permeability of the medium, respectively. The middle layer is considered to be a metal having a permittivity ϵ_m while the bottom layer is a three-level lambda type EIT medium with electric permittivity ϵ_b. The levels $|1\rangle$, $|2\rangle$ and $|3\rangle$ denotes the energy levels of the lambda-type atomic system in which the transition between the levels $|1\rangle$ and $|2\rangle$ is driven by a weak probe field of angular frequency, ω_p and the transition between the levels $|2\rangle$ and $|3\rangle$ is driven by a strong coupling field of angular frequency, ω_c. $\Omega_p = \frac{\vec{E}_p(\vec{r},t).\vec{\mu}_{21}}{2\hbar}$ and

$\Omega_c = \frac{\vec{E}_c(\vec{r},t).\vec{\mu}_{23}}{2\hbar}$ denotes the Rabi frequencies associated with the probe and coupling fields with frequency detunings $\delta_p = \omega_p - \omega_{21}$ and $\delta_c = \omega_c - \omega_{23}$, respectively. The dynamics of the three-level lambda-type atomic medium is given by the Maxwell Bloch equations [185, 186]. Using the dipole and the rotating wave approximations, the equation of motion of the medium can be described by the density matrix equations as follows:

$$\dot{\rho}_{11} = \gamma_{31}(\rho_{33} - \rho_{11}) + \gamma_{21}\rho_{22} - \frac{i}{2}\Omega_p\rho_{21} + \frac{i}{2}\Omega_p\rho_{12}, \tag{5.1a}$$

$$\dot{\rho}_{22} = -(\gamma_{31} + \gamma_{21})\rho_{22} - \frac{i}{2}\Omega_p\rho_{12} + \frac{i}{2}\Omega_p\rho_{21} - \frac{i}{2}\Omega_c\rho_{32} + \frac{i}{2}\Omega_c\rho_{23}, \tag{5.1b}$$

$$\dot{\rho}_{33} = \gamma_{31}(\rho_{11} - \rho_{33}) + \gamma_{23}\rho_{22} + \frac{i}{2}\Omega_c\rho_{32} - \frac{i}{2}\Omega_c\rho_{23}, \tag{5.1c}$$

$$\dot{\rho}_{21} = -(\gamma - i\delta_p)\rho_{21} + \frac{i}{2}\Omega_p(\rho_{22} - \rho_{11}) - \frac{i}{2}\Omega_c\rho_{31}, \tag{5.1d}$$

$$\dot{\rho}_{23} = -(\gamma - i\delta_c)\rho_{23} + \frac{i}{2}\Omega_c(\rho_{22} - \rho_{33}) - \frac{i}{2}\Omega_c\rho_{13}, \tag{5.1e}$$

$$\dot{\rho}_{31} = -[\gamma_{31} - i(\delta_p - \delta_c)]\rho_{31} + \frac{i}{2}\Omega_p\rho_{32} - \frac{i}{2}\Omega_p\rho_{21}. \tag{5.1f}$$

Under the slowly varying approximation, the evolution of the weak probe field in the system which is given by the Maxwell Equation, $\nabla^2\vec{E} - \left(\frac{1}{c^2}\right)\frac{\partial^2\vec{E}}{\partial t^2} = \left(\frac{1}{\epsilon_0 c^2}\right)\frac{\partial^2\vec{P}}{\partial t^2}$ as

$$i\left(\frac{\partial}{\partial x} + \frac{1}{n_{eff}c^2}\frac{\partial}{\partial t}\right)\Omega_p(\vec{r},t) + \kappa\rho_{21} = 0, \tag{5.2}$$

where $\kappa = 2\pi N\omega_p|\vec{\mu}_{21}|^2/\hbar c$ is the coupling coefficient, where N is the atomic density of the atomic medium, $\vec{\mu}_{ij}$ is the dipole moment of the transition $|j\rangle \to |i\rangle$ (for $i,j = 1,2,3$), ϵ_0 is the absolute electric permittivity. $n_{eff} = ck_p/\omega_p$ is the effective refractive index of the system. Here, the dielectric constant of the medium can be obtained with effective-medium theory and taking into account local fields, as

$$\epsilon_b = 1 + \frac{\chi_p}{1 - \frac{\chi_p}{3}}, \tag{5.3}$$

where, χ_p is the effective susceptibility of the medium which is expressed as follows:

$$\chi_p = \chi_p^{(1)} + \frac{3}{4}E_p^2\chi_p^{(3)}. \tag{5.4}$$

5.3 Coupler-free excitation of surface plasmons

In the linear regime, the density matrix elements and the probe field could be expanded using the perturbation method [186] as $\rho_{ij} = \rho_{ij}^{(0)} + \rho_{ij}^{(1)}$ and $\Omega_p(\vec{r},t) = \epsilon\Omega_p^{(1)}(\vec{r},t)$, respectively where $\epsilon << 1$ is the perturbation parameter. Moreover, we consider $\Omega_p^{(1)}(\vec{r},t) = Fe^{i\phi}$, and $\rho_{ij}^{(1)}(\vec{r},t) = \rho_{ij}^{(1)}(\vec{r})Fe^{i\phi}$, where F is a constant describing the pulse envelope of the SPs and $\phi = K(\omega)z - \omega t$, with ω as the frequency of the SP and the linear dispersion of the atomic medium is given by

$$K(\omega) = \frac{\omega}{n_{eff}c} + \frac{\kappa(\omega+\delta_c+i\gamma_{31})}{|\Omega_c|^2 - (\omega+\delta_p+i\gamma_{21})(\omega+\delta_c+i\gamma_{31})} \tag{5.5}$$

By assuming a weak field limit of the incident probe field, we have ${\rho_{11}}^{(0)} \approx 1$, $\rho_{22}^{(0)} \approx 0$ and $\rho_{33}^{(0)} \approx 0$. Using these conditions, we can obtain the expression for ρ_{21} to the first order as follows:

$$\rho_{21}^{(1)}(\vec{r}) = \frac{-i\Omega_p^{(1)}[\gamma_{21} - i(\delta_p - \delta_c)]}{2\Big[(\gamma - i\delta_p)[\gamma_{31} - i(\delta_p-\delta_c)] + (\Omega_c/2)^2\Big]} \tag{5.6}$$

Then, the linear susceptibility of the atomic medium is given by

$$\chi_p^{(1)} = \frac{N|\vec{\mu}_{21}|^2}{\hbar E_p}\rho_{21}^{(1)}. \tag{5.7}$$

In the proposed scheme, the excitation of surface plasmon polaritons can be explained with the help of the transmittance (T) and the reflectance (R) of the three-layer structure. The three-layer transmission and the reflection coefficients of the three-layer structure is briefly discussed in section 1.3.2, where the transmittance and the total reflection is calculated using the expressions, $T = |t_{tmb}|^2$ and $R = |r_{tmb}|^2$, respectively. The normal wave vectors is given by $k_{jz}^2 = k_0^2\epsilon_k - k_x^2$ where $j = t, m, d$ while the parallel wave vector is given by $k_x = k_0 n_t \sin\theta_p$, where $k_0 = \omega/c$ is the vacuum wave number and θ_p is the incident angle of the probe field.

The relative permittivity and the SP resonances are depicted in Fig. 5.2. Figure 5.2 (a) represents the real and imaginary part of the relative permittivity while Fig. 5.2(b) represents the transmittance and the reflectance of the proposed structure. In the proposed scheme, we consider the three-level atomic medium as the D2 line ($3^2S_{1/2} \rightarrow 3^2P_{3/2}$) of the Sodium atom, with the energy levels $|1\rangle = |3S_{1/2}, F=1\rangle$, $|2\rangle = |3P_{3/2}, F=0\rangle$ and

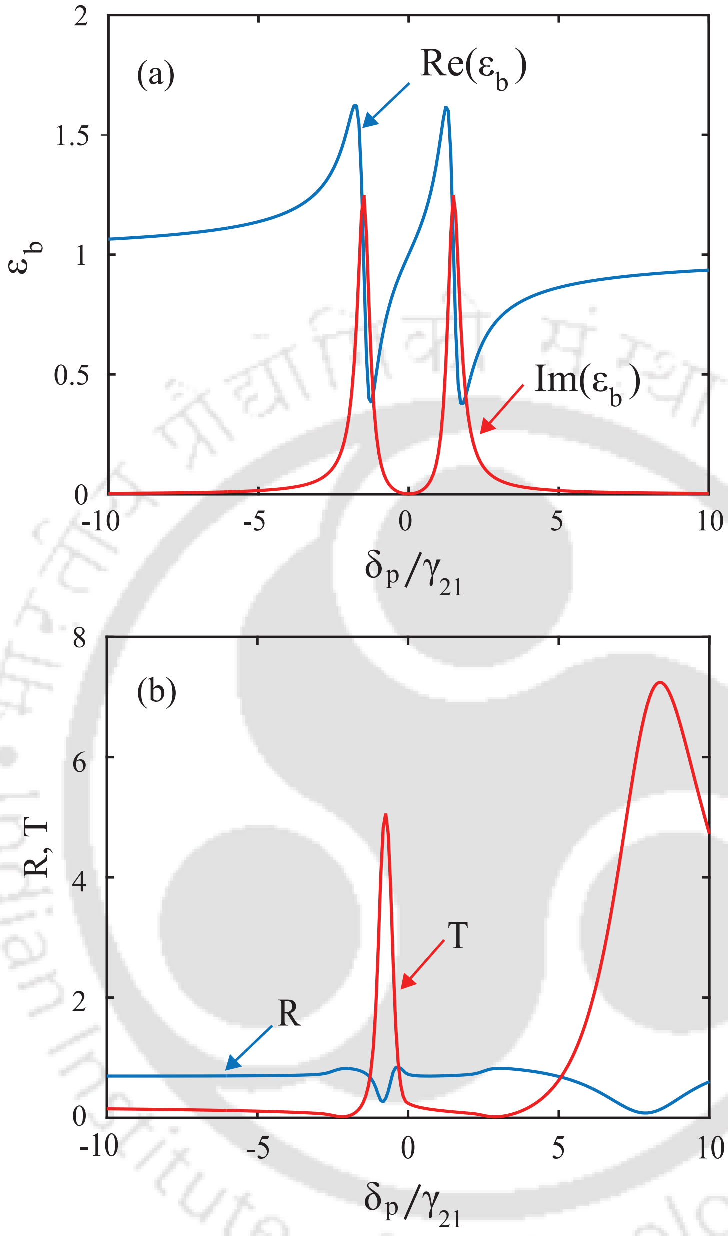

Figure 5.2: (a) The relative permittivity of the EIT medium (described by Eq. 5.3). $Re(\epsilon_b)$ is represented by blue solid line while the $Im(\epsilon_b)$ is represented by the red solid line, and (b) the transmittance (red line) and the reflectance (blue line) of the proposed three-layer structure. Here, we have taken the parameters: $\theta_p = 80^o$, $\theta_c = 0^o$, $q = 30\ nm$, $\gamma_{21} = 61.54\ MHz$, $\Omega_c = 2\gamma_{21}$ and $\lambda_p = 589.1\ nm$, $\omega_{31} = 1.8\ GHz$ and $N = 8 \times 10^{19}\ m^{-3}$ [187].

$|3\rangle = |3S_{1/2}, F = 2\rangle$ [187]. For EIT to occur, we assume that probe beam is much weaker than the pump beam. Here, we have taken the parameters [187]: $\gamma_{21} = 61.54\ MHz$, $\Omega_c = 2\gamma_{21}$, $\lambda_p = 589.1\ nm$, $\omega_{31} = 1.8\ GHz$ and $N = 8 \times 10^{19}\ m^{-3}$. Additionally, the middle layer is considred to be a layer of Silver metal having a dielectric permittivity, $\epsilon_m = -13.3 + 0.883i$ [188] which is approximated to be constant within the EIT window. Then, for a particular value of the angle of incidence of the probe and the coupling field, the atomic medium exhibits the EIT phenomenon.

It is evident from the Fig. 5.2(a), that the condition $Re(\epsilon_b) < 1$ and $Im(\epsilon_b) << 1$ is achieved when δ_p is slightly less than 0. In this case, the relative permittivity, $\epsilon_b < 1$ and as a result, the wave-number of the SPs, $\beta = k_0\sqrt{\frac{\epsilon_m \epsilon_b}{\epsilon_m + \epsilon_b}}$ can be less than the wave-number of the incident light, i.e., $\beta < k_0$. Hence, the surface plasmon resonance (SPR) condition which is given by the expression $k_0 n_t \sin\theta_p = \beta$ can be satisfied even for $n_t = 1$ for a proper set of incidence angle. At this position, it is observed that the transmittance T is greatly enhanced and the total reflection R drops to a small value such that $T >> R$ (see Fig. 5.2(b)), which is the signature of the resonant excitation of SPs. Hence, a coupler free excitation of surface plasmon polaritons at the interface of the metal and the EIT medium is possible in the proposed structure. In the proposed coupler-free planar plasmonic waveguide struture, it is natural to examine the behavior of the excited SP resonances in the nonlinear regime. In the nonlinear regime, the SPs can exhibit interesting solitonic behavior which can be of great significance in overcoming the propagation loss inherent in the case of SPs. Therefore, in the subsequent sections, we further examine the generation and evolution of the surface polaritonic solitons and the surface polaritonic breathers in the proposed structure.

5.4 Surface polaritonic solitons

The dynamics of the coupler free excited surface plasmon polaritons in the non-linear regime, can be investigated with the help of the standard multiple scales method [189], by introducing the asymptotic expansions of the density matrix equations, $\rho_{ij} - \rho_{ij}^{(0)} = \sum_l \epsilon^l \rho_{ij}^{(l)}$ and the Rabi frequency of the probe field $\Omega_p = \sum_l \epsilon^l \Omega_p^l$ where $x_l = \epsilon^l x$ $(l = 0, 1, 2)$ and $t_l = \epsilon^l t$ $(l = 0, 1)$ are the multiscale variables. By substituting these expansions in the Maxwell Bloch equations a linear and inhomogeneous set of equations for $\rho_{ij}^{(l)}$ and $\Omega_p^{(l)}$ is obtained, which can be solved for different orders. For the second order, the solvability condition leads to the propagation of the probe pulse, which can be expressed as

$$\left(\frac{\partial}{\partial x_1} + \frac{1}{V_g}\frac{\partial}{\partial t_1}\right)F = 0 \tag{5.8}$$

where V_g is the group velocity and F is the envelope function of the probe field which is yet to be determined. The group velocity is calculated using the expression, $V_g = 1/K_1$ where $K_1 = \partial K(\omega)/\partial\omega$ is the first-order dispersion. Further, the solvability condition in the third order is expressed as

$$i\frac{\partial}{\partial x_2} - \frac{1}{2}K_2\frac{\partial^2 F}{\partial {t_1}^2} - W|F|^2 F e^{-2\alpha x_2} = 0 \tag{5.9}$$

where $\alpha = \epsilon^2 Im(K(\omega))$ represents the absorption of the atomic medium, $K_2 = \partial^2 K(\omega)/\partial\omega^2$ represents the group velocity dispersion (GVD), and the Kerr nonlinearity is represented by $W \propto \chi_p^{(3)}$, where $\chi_p^{(3)}$ is the third order susceptibility given by

$$\chi_p^{(3)} = \frac{iN|\vec{\mu}_{21}|^4}{\hbar E_p}\rho_{21}^{(3)}. \tag{5.10}$$

Here, we can obtain the expression for ρ_{21} to the third order as follows

$$\rho_{21}^{(3)} = \frac{i\Omega_p^{(1)}}{2D}\left[\frac{\left(\Omega_p^{(1)}\right)^2}{2\gamma+\gamma_{21}}\left(\frac{1}{D}+\frac{1}{D^*}\right)+\frac{2\gamma_{31}}{2\gamma+\gamma_{21}}\right] \tag{5.11}$$

where $D = \left(\gamma - i\delta_p\right) - \frac{\Omega_c/2}{\left[\gamma_{31}-i\left(\delta_p-\delta_c\right)\right]}$. By choosing the parameters: $\gamma_{21} = 61.54\ MHz$, $\delta_c = 3\ MHz$, $\Omega_c = 2\gamma_{21}$, $\lambda_p = 589.1\ nm$ and $\omega_{31} = 1.8\ GHz$, we obtain the value of susceptibility, which is described by Eq. (5.10), as $\chi_p^{(3)} = (5.55 + 0.0832i) \times 10^{-7}\ m^2V^{-2}$. This nonlinearity competes with the dispersion in the system giving rise to solitonic behavior of the SPs in the system. The nonlinear Schrӧdinger equation (NLSE), describing the dynamics of the SPs in the nonlinear regime, can be obtained by combining all the equations in all the orders, as follows:

$$i\left(\frac{\partial}{\partial x}+\alpha\right)U - \frac{1}{2}K_2\frac{\partial^2 U}{\partial T^2} - W|U|^2 U = 0, \tag{5.12}$$

where $T = t - x/\tilde{V}_g$, $U = \epsilon F e^{-\alpha x}$ and $\alpha = Im(K(\omega))$. At the EIT position, there is null absorption (i.e.,$\alpha \approx 0$) and the imaginary part of the coefficients is much smaller than its real parts. Here, by neglecting the imaginary parts of the coefficients, Eq. (5.12) reduces to the normalized form:

$$i\frac{\partial u}{\partial \zeta} + \frac{1}{2}\frac{\partial^2 u}{\partial \tau^2} + \delta|u|^2 u = 0, \tag{5.13}$$

where $x = -L_D\zeta$, $T = T_0\tau$ and $u = U/U_0$. The dispersion length of the medium is given by $L_D = {T_0}^2/\tilde{K}_2$ and the nonlinear length of the medium is given by $L_{non} = 1/|{U_0}^2|\tilde{W}$.

Here, T_0 is the pulse duration, δ denotes the Kerr nonlinearity and $U_0 = \frac{1}{T_0}\sqrt{\tilde{K}_2/\tilde{W}}$ is the typical Rabi frequency of the probe field. For $\delta = +1$, Eq. (5.13) can assume the fundamental bright soliton solutions, which is given by $u_B = \mathrm{sech}(\tau)e^{i\zeta}$. The bright polaritonic soliton solution in the original variables is given by the expression: $\Omega_p^B = U\exp(i\tilde{K}_0 x)$, which can be expressed as

$$\Omega_p^B = \frac{1}{T_0}\left(\frac{\tilde{K}_2}{\tilde{W}}\right)^{1/2} \mathrm{sech}\left[\frac{1}{T_0}\left(t-\frac{x}{\tilde{V}_g}\right)\right] e^{i\left[\tilde{K}_0-\frac{1}{2L_D}\right]x}, \tag{5.14}$$

where the $\tilde{K}_2$ and $\tilde{W}$ denotes the real part of the variables K_2 and W. Then, the corresponding electric fields for the bright soliton can be expressed as

$$E_p^B = \frac{\hbar}{|\vec{\mu}_{21}|T_0}\left(\frac{\tilde{K}_2}{\tilde{W}}\right)^{1/2} \mathrm{sech}\left[\frac{1}{T_0}\left(t-\frac{x}{\tilde{V}_g}\right)\right] e^{i\left[\left(\tilde{K}_0+k_p-\frac{1}{2L_D}\right)x-\omega_p t\right]}, \tag{5.15}$$

In order to investigate the evolution and the propagation for the bright polaritonic solitons, we assume the initial condition as $E_p^B(0,t)/U_0 = \mathrm{sech}\big(T/T_0\big)exp\big(iT/T_0\big)$. It is noteworthy to mention that the proposed scheme can be observed in an experiment by choosing realistic parameter. By taking $\delta_c = 3MHz$, $T_0 = 10ps$, $\Omega_c = 2\gamma_{21}$, one can assume a stable propagation of the bright polaritonic soliton. For these specific values, we get $W = (1.47 + .069i)\times 10^{-16}\ m^{-1}s^2$. Then, for this set of parameters, the spatiotemporal dynamics of the bright polaritonic solitons within the EIT transparency window in the proposed structure can be examined as a function of distance and time. The bright polaritonic soliton propagation through the system is depicted in Fig. 5.3. It is evident from the figure that the bright polaritonic solitons can propagate through the waveguide for a long distance without encountering much distortion. The bright polaritonic soliton retains its shape and amplitude as it propagates through the system. This stable propagation is achieved as a result of the balanced dispersion with the sufficient self-focusing provided by the inherent Kerr nonlinearity within the EIT transparency of the system.

Similar investigation can be carried out for the case of dark polaritonic solitons as well. For $\delta = -1$, we obtain the fundamental dark soliton solutions which is given by $u_D = \tanh(\tau)e^{i\zeta}$. By returning to the original variables, the dark polaritonic soliton solution is given by the relation $\Omega_p^D = U\exp(i\tilde{K}_0 x)$, which can be further expressed as follows:

$$\Omega_p^D = \frac{1}{T_0}\left(\frac{\tilde{K}_2}{\tilde{W}}\right)^{1/2} \tanh\left[\frac{1}{T_0}\left(t-\frac{x}{\tilde{V}_g}\right)\right] e^{i\left[\tilde{K}_0-\frac{1}{2L_D}\right]x}, \tag{5.16}$$

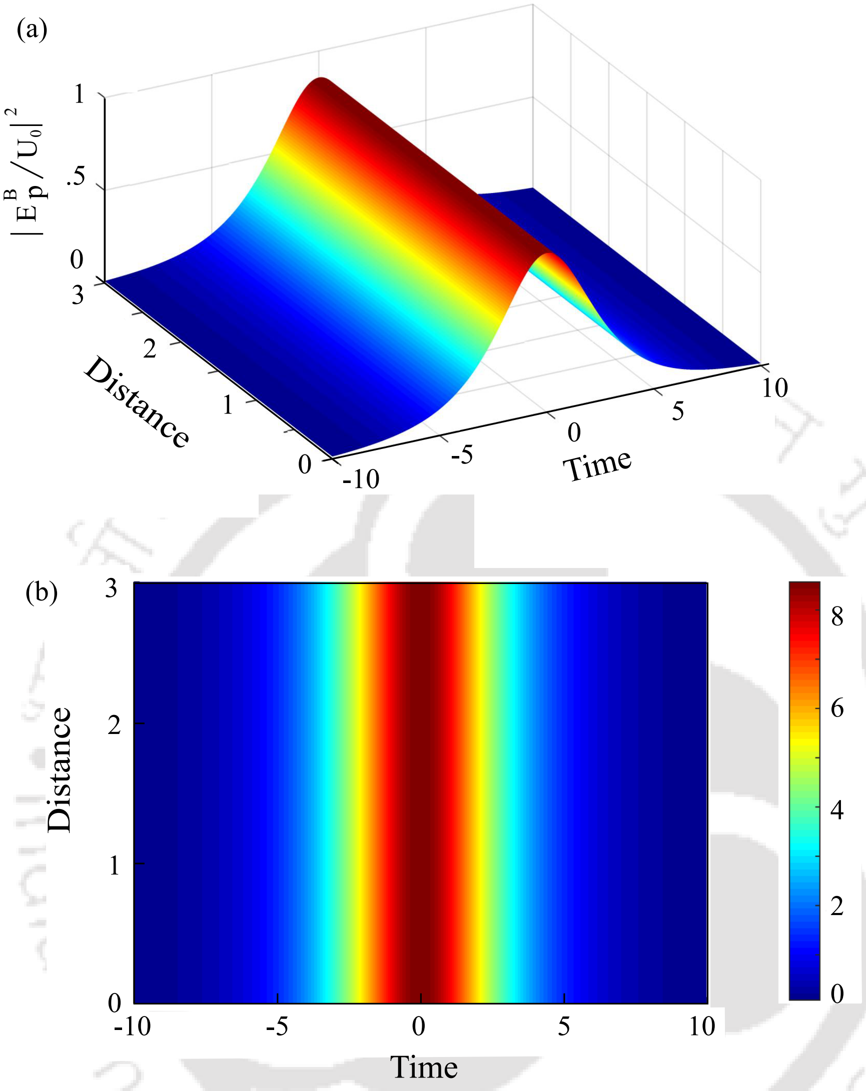

Figure 5.3: The spatiotemporal dynamics of the bright polaritonic solitons within the EIT transparency window, in the proposed structure as a function of distance and time. (a)The evolution of the probe field intensity $|E_p^B/U_0|^2$ as a function of x/L_D and T/T_0. (b) The 2D contour plot of the bright polaritonic solitons corresponding to (a) for the following parameters: $\delta_c = 3\ MHz$, $T_0 = 10\ ps$, $\Omega_c = 2\gamma_{21}$, $\omega_p = 3.19\times10^{15}\ Hz$.

For the dark polaritonic solitons, the corresponding electric fields is given by the expression

$$E_p^D = \frac{\hbar}{|\vec{\mu_{21}}|T_0}\left(\frac{\tilde{K}_2}{\tilde{W}}\right)^2 \tanh\left[\frac{1}{T_0}\left(t-\frac{x}{\tilde{V}_g}\right)\right] e^{i\left[\left(\tilde{K}_0+k_p-\frac{1}{2L_D}\right)x-\omega_p t\right]}, \qquad (5.17)$$

The propagation dynamics of the dark polaritonic soliton is numerically investigated by taking the initial condition is taken as $E_p^D(0,t)/U_0 = \tanh\left(T/T_0\right)exp\left(iT/T_0\right)$. Figure 5.4

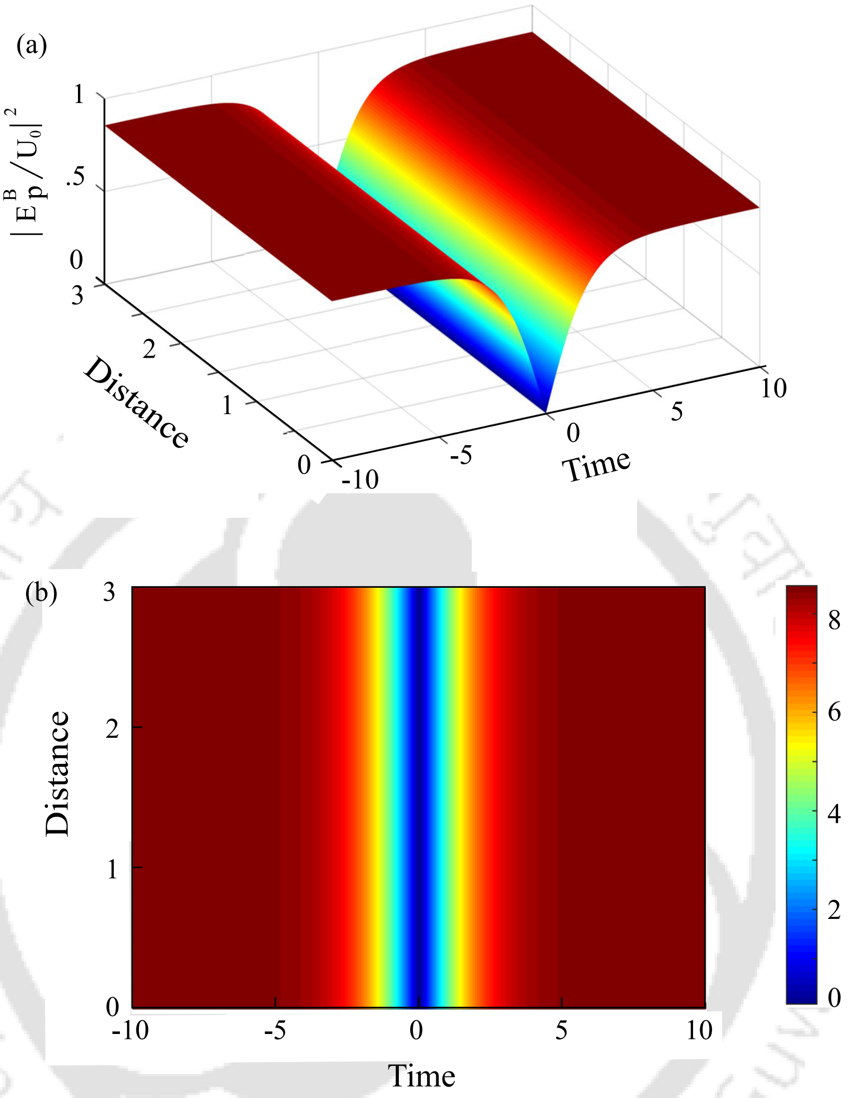

Figure 5.4: Excitation and propagation of the dark surface polaritonic solitons in the planar plasmonic waveguide structure. (a) The evolution of the probe field intensity $|E_p^D/U_0|^2$ as a function of x/L_D and T/T_0 along with (b) the corresponding contour map.

depicts the evolution of the dark polaritonic solitons in the proposed system. Similar to the case of the bright polaritonic solitons, the initial pulse retains its shape and amplitude for a long distance in the case of the dark polaritonic solitons as well, resulting in the stable propagation of the pulse in the proposed system. Such undistorted propagation of these polaritonic solitons can find immense applications in communication in the optical regime.

5.5 Surface polaritonic Akhmedeiv breathers

The standard NLSE, described by Eq. (5.12), can assume other exact solutions which are periodic in ζ and τ [183]. The Akhmediev breather is one such solution, and it is given by the expression

$$u = 1 + \frac{2[1-2a]\cosh(b\zeta) + ib\sinh(b\zeta)}{\sqrt{2a}\cos(\Omega\tau) - \cosh(b\zeta)} e^{i\zeta} \tag{5.18}$$

Then, we have

$$\Omega_p^{AB} = U_0 \left[1 + \frac{2[1-2a]\cosh(b\zeta) + ib\sinh(b\zeta)}{\sqrt{2a}\cos(\Omega\tau) - \cosh(b\zeta)} \right] e^{i\left[\vec{K}_0 x + \frac{x}{L_D}\right]} \tag{5.19}$$

Returning to the original variables we get

$$\Omega_p^{AB}(x,T) = U_0 \left[1 + \frac{[1-4a]\cosh(bx/L_D) + \sqrt{2a}\cos(\Omega T/T_0) ib\sinh(bx/L_D)}{\sqrt{2a}\cos(\Omega T/T_0) - \cosh(bx/L_D)} \right] e^{i\left[\vec{K}_0 x + \frac{x}{L_D}\right]} \tag{5.20}$$

where a is the modulation parameter, $\Omega = 2\sqrt{1-2a}$ is the spatial modulation frequency and $b = \sqrt{8a(1-2a)}$ is the parametric gain coefficient. $T = \pi/\sqrt{1-2a}$ is the time period of the periodic pulses. The evolution and propagation of the surface polaritonic Akhmediev breathers in the planar plasmonic waveguide structure for different values of a, is depicted in Fig. 5.5. In order to have a physical understanding of the evolution of the surface polaritonic Akhmediev Breather, we can assume the initial SPs to be a plane wave (corresponding to $a = 0$) which evolves into a significant pulse shape due to the parametric gain coefficient. As a result the SP's amplitude gets significantly amplified by a growth factor of b. With further modulation of the instability, the amplified SP's evolves into a train of periodic pulses along the time axis with a period of T. Hence, the first-order surface polaritonic Akhmediev breathers can be potentially excited and propagated in this waveguide.

The dynamics of the surface polaritonic Akhmediev breather in the proposed structure depends strongly on the modulation frequency. Here, for $0 < a < 0.5$, it is evident from Fig. 5.5 that the separation between the adjacent peak intensities increases with the increase of a. By taking realistic values of the modulation parameter as $a = 0.25$ (see Figs. 5.5(a), (b)), we can obtain maximum peak intensity with a time-period $T = 1.4\pi$, and $\Omega = 1.41$, $b = 1$. Figures 5.5 (c) and 5.5(d), represent the breather propagation for the modulation parameter, $a = 0.4$ with $T = 2.23\pi$, $\Omega = 0.89$ and $b = 0.8$. It is observed

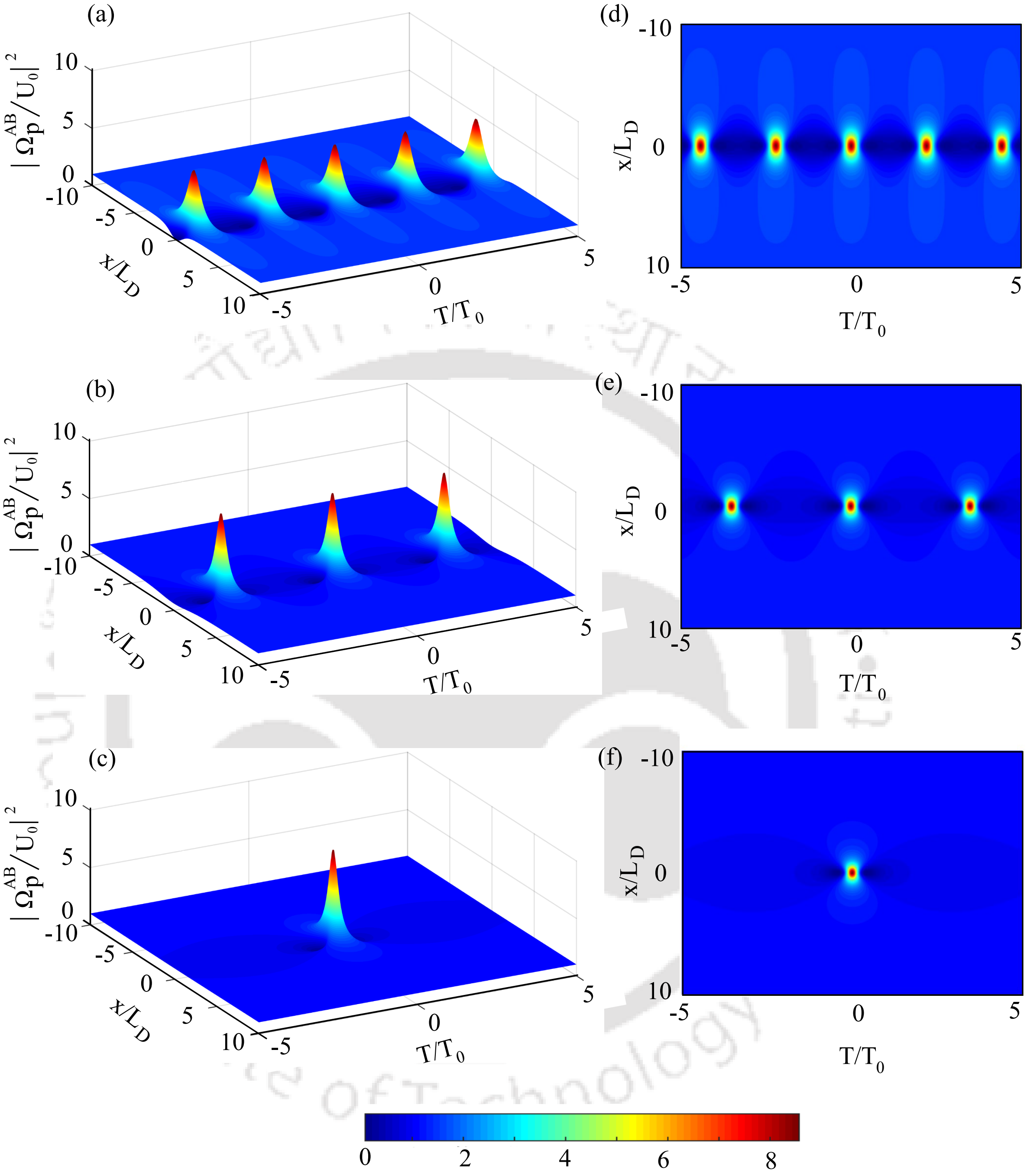

Figure 5.5: The dynamics of the surface polaritonic Akhmediev breathers in the planar plasmonic waveguide structure. (a) The evolution of the probe field intensity $|\Omega_p^{AB}/U_0|^2$ as a function of x/L_D and T/T_0 along with (b) the corresponding contour map. Here, we have used the parameters $a = 0.25$, $\Omega = 1.41$, and $b = 1$.(c) The evolution of the surface polaritonic Akhmediev breathers along with its (d) corresponding contour map for the parameters $a = 0.4$, $\Omega = 0.89$, and $b = 0.8$. (e) The Peregrine soliton along with its (f) corresponding contour map.

that the spatial width of the individual pulse increases with increasing value of the modulation parameter while the temporal width of the pulses decreases with an increase of the modulation parameter. Finally, for a limiting case of $a \rightarrow 0.5$, there is a significant spatial and temporal localization of the pulse leading to an increased localization of peak intensity. This spatiotemporally localized pulse is the so-called Peregrine soliton which is depicted in Figs. 5.5(e) and (f). Hence, a stable propagation of the surface polaritonic Akhmediev Breather is possible in the structure with judicious choice of parameters. The effective localization of these surface polaritonic breathers can lead to the generation of extremely short pulses in such coupler-free planar plasmonic structure.

5.6 Conclusion

In conclusion, we investigate the excitation of surface polaritonic solitons and breathers in a coupler-free planar plasmonic waveguide structure comprising of a transparent layer, a metal layer and a three-level lambda-type atomic medium. In the linear regime, it is observed that the coupler-free excitation of SP resonances is possible in the proposed structure. Further, a giant Kerr nonlinearity is achieved in the system as a result of electromagnetically induced transparency in the bottom atomic layer, which can be controlled through proper modulation of the parameters of the driving laser fields. The self-phase modulation caused by the Kerr nonlinearity balances the group velocity dispersion in the system hence providing the necessary condition for the excitation of surface polaritonic solitons within the narrow transparency window of the electromagnetically induced transparency. It is observed that the system yields laterally self-trapped bright and dark surface polaritonic solitons which is tightly guided at the interface of the metal and the EIT medium. Finally, we show that a stable propagation and an effective localization of the surface polaritonic Akhmediev breathers can be achieved with proper choice of parameters in the proposed planar plasmonic waveguide structure. This study can be significant in the development of highly compact nano-optical and photonic devices in the optical regime.

CHAPTER 6

SUMMARY AND FUTURE WORK

In this thesis, we have discussed different aspects of the electromagnetically induced transparency (EIT) phenomenon such as tunable transparency window, steep dispersion and enhanced nonlinearity in the context of terahertz metamaterials (MMs) and planar plasmonic waveguide structures. In chapter 1, we introduce EIT effect and present a comprehensive literature survey of this effect, and its significance at optical and terahertz frequencies. In chapter 2, we discuss plasmon induced transparency (PIT) effect in a coupled terahertz MM whose meta-atom comprises of two C-shaped (2C) resonators placed alternately on both sides of a cut-wire (CW) structure. Modulation of the PIT transparency window is achieved by varying the horizontal displacement between the CW and 2C structures. As the horizontal displacement is increased, the transparency window becomes narrower in the proposed MM structure. In order to corroborate our numerical observations, a simple equivalent circuit model using coupled oscillator theory is discussed. We establish that the PIT effect in the proposed MM occurs due to capacitive coupling between the CW and the 2C resonators. We further discuss a polarization independent PIT effect in a terahertz MM configuration that comprises of an array of cross-wire and four C-shaped (4C) resonators. Simulations reveal that an identical transmission response could be achieved through this new MM geometry for two orthogonal polarizations of the incident terahertz beam, which indicates a polarization independent PIT behavior in the structure. For this geometry, the transparency window is modulated by displacing the C-shaped resonators diagonally with respect to the cross-wire. The transparency window gets narrower as the resonators are displaced away from the cross wire due to a decrease in the coupling strength.

In chapter 3, the PIT effect in a near field coupled terahertz MM structure comprising of an array of graphene strips and a pair of graphene split ring resonators (SRRs) is discussed. The PIT in the proposed configuration occurs due to the destructive interference of the resonances from the graphene strip and the graphene SRRs. The PIT effect in the MM structure is modulated by varying the vertical displacement as well as horizontal displacement of the graphene SRRs with respect to the graphene strip. As the graphene SRRs are displaced in the vertical direction, it is observed that the PIT effect vanishes for a configuration when the centers of the SRRs are collinear to the center of the graphene strip. In the case of horizontal displacement, it is observed that the PIT transparency window becomes narrower due to reduced coupling between the graphene strip and graphene SRRs. Further, the PIT effect is studied for different values of Fermi energy of the graphene material. The PIT transparency window exhibits a blue shift as the Fermi energy gradually increases from 0.4 eV to 0.7 eV, establishing a dynamic tuning capability of the proposed MM structure. Finally, an analytical model based on a three-level plasmonic system is discussed to elucidate our numerical findings. The transmission results obtained using the analytical model is in good agreement with the numerical results.

In chapter 4, we discuss dual-band electromagnetically induced transparency (EIT) effect in a planar terahertz MM structure, comprising of an inner circular split ring resonator (CSRR) concentrically coupled to an outer asymmetric two-gap circular split ring resonator (ASRR). The MM structure exhibits the effect as a result of coupling between the resonant mode of the CSRR and the EIT response of the ASRR. Modulation of the dual-band EIT effect in the MM structure is achieved by varying the rotation parameter of the CSRR structure. The coupling behavior in the proposed MM structure is modified through an in-plane rotation of the CSRR structures. We show that a gradual orthogonal rotation of the CSRR leads to the vanishing of the dual-band EIT effect in the MM. Modulation of the effect is further achieved by gradually varying the asymmetry of the outer ASRR as well as the size of the inner CSRR. It is observed that the dual band EIT effect becomes more prominent as the asymmetry parameter is increased, while a red shift is experienced by the second transparency region as the size of the inner CSRR is increased. Finally, a theoretical model based on a Four-Level Tripod system explaining the coupling behavior in the proposed MM structure is discussed.

In chapter 5, we discuss a coupler-free scheme for the excitation of surface polaritonic solitons and breathers in a planar plasmonic waveguide structure based on the EIT phenomenon. The proposed structure comprises of a transparent layer, a metal layer and a three-level lambda-type atomic medium. A giant Kerr nonlinearity is achieved in the system as a result of EIT in the bottom atomic layer, which is controlled through proper modulation of the parameters of the driving laser fields. In the proposed scheme, the competition between the normal dispersion and Kerr nonlinearity yields laterally self-trapped polaritonic solitons which is tightly guided at the interface of the metal and the EIT medium. Within the narrow transparency window of the EIT effect, the excitation of surface polaritonic breathers is also discussed. Further, we discuss a stable propagation of the surface polaritonic solitons and breathers in the proposed structure.

Future aspects

The EIT effect in terahertz MMs and plasmonic structures has proven to be a promising area of research due to its abundant applications in the development of devices. For instance, the tunable transparency window achieved in the PIT effect in the terahertz MM structures can be significant in designing devices for a range of applications in the broadband [103, 104] as well as narrowband regime. For a strong coupling between the resonant structures, the coupled MM structure exhibits a broad transparency window, which eventually gets narrower with the reduction of coupling between the resonators. A narrow transparency window indicates a steeper dispersion which can be exploited for tailoring slow light devices in the terahertz regime [94, 109, 157]. For most applications, a strong response is essential irrespective of the incident polarization. Consequently, the polarization independent PIT behavior achieved in our study enhances the efficiency of the devices and can lead to the development of devices for polarization independent broadband, slow light and sensing applications. The dynamic tunability achieved in the case of the graphene based terahertz MM can be significant in the realization of frequency agile actively tunable devices [105, 159]. The narrow region of absorption associated with the dual-band EIT effect in our study could be exploited for the development of narrowband absorbers. Also, the double tunable transparency region of the dual-band EIT effect can be significant in the development of multiband slow light devices [115]. Finally, the coupler free scheme for the excitation of polaritonic solitons and breathers can be of great significance for the development of highly compact photonic structures [78]. The shape preserving polaritonic solitons achieved in the scheme can find immense applications in optical communication and related devices.

Benefitting from the rapid advancement of fabrication techniques and the numerous accessible simulation tools, new experimental demonstrations and theoretical studies are coming up, to explore the possibility of realizing various applications of the EIT effect in terahertz MMs and planar plasmonic waveguide structures. For instance, there is a possibility of exploring the dynamic tunability of dual-band EIT effect in graphene based MM structures which would have tremendous applications in the development of actively tunable multiband devices in the terahertz frequency regime. A polarization independent dual-band EIT effect in terahertz metamaterials can be possibly explored for the development of polarization independent narrowband absorbers, polarization independent multiband slow light devices. Furthermore, the excitation of polaritonic solitons and breathers can be possibly explored in the context of terahertz MMs. Therefore, in view of the recent trends in this area of research, there are endless possibilities in exploring the potential applications of the EIT effect in terahertz MMs and planar plasmonic waveguide structures.

BIBLIOGRAPHY

[1] William L Barnes, Alain Dereux, and Thomas W Ebbesen. Surface plasmon subwavelength optics. *nature*, 424(6950):824, 2003.

[2] Robert Halir, Przemek J Bock, Pavel Cheben, Alejandro Ortega-Moñux, Carlos Alonso-Ramos, Jens H Schmid, Jean Lapointe, Dan-Xia Xu, J Gonzalo Wangüemert-Pérez, Íñigo Molina-Fernández, et al. Waveguide sub-wavelength structures: a review of principles and applications. *Laser & Photonics Reviews*, 9(1):25–49, 2015.

[3] B Wood, JB Pendry, and DP Tsai. Directed subwavelength imaging using a layered metal-dielectric system. *Physical Review B*, 74(11):115116, 2006.

[4] Rupert F Oulton, Volker J Sorger, Thomas Zentgraf, Ren-Min Ma, Christopher Gladden, Lun Dai, Guy Bartal, and Xiang Zhang. Plasmon lasers at deep subwavelength scale. *Nature*, 461(7264):629, 2009.

[5] Mark L Brongersma and Pieter G Kik. *Surface plasmon nanophotonics*, volume 131. Springer, 2007.

[6] Harry A Atwater and Albert Polman. Plasmonics for improved photovoltaic devices. *Nature materials*, 9(3):205, 2010.

[7] Vladimir M Shalaev and Satoshi Kawata. *Nanophotonics with surface plasmons*. Elsevier, 2006.

[8] Sergey I Bozhevolnyi, A Universitet, and VM Shalaev. Nanophotonics with surface plasmons-part i. *Photonics spectra*, 40(1):58, 2006.

[9] Yongmin Liu and Xiang Zhang. Metamaterials: a new frontier of science and technology. *Chemical Society Reviews*, 40(5):2494–2507, 2011.

[10] Nader Engheta and Richard W Ziolkowski. *Metamaterials: physics and engineering explorations*. John Wiley & Sons, 2006.

[11] Dmitri K Gramotnev and Sergey I Bozhevolnyi. Plasmonics beyond the diffraction limit. *Nature photonics*, 4(2):83, 2010.

[12] Stefan Alexander Maier. *Plasmonics: fundamentals and applications*. Springer Science & Business Media, 2007.

[13] Vladimir M Shalaev, Wenshan Cai, Uday K Chettiar, Hsiao-Kuan Yuan, Andrey K Sarychev, Vladimir P Drachev, and Alexander V Kildishev. Negative index of refraction in optical metamaterials. *Optics letters*, 30(24):3356–3358, 2005.

[14] David R Smith, John B Pendry, and Mike CK Wiltshire. Metamaterials and negative refractive index. *Science*, 305(5685):788–792, 2004.

[15] Wenshan Cai and Vladimir M Shalaev. *Optical metamaterials*, volume 10. Springer, 2010.

[16] DR Smith, DC Vier, Th Koschny, and CM Soukoulis. Electromagnetic parameter retrieval from

inhomogeneous metamaterials. *Physical review E*, 71(3):036617, 2005.

[17] Victor Georgievich Veselago. The electrodynamics of substances with simultaneously negative values of $= \epsilon$ and μ. *Physics-Uspekhi*, 10(4):509–514, 1968.

[18] John Brian Pendry. Negative refraction makes a perfect lens. *Physical review letters*, 85(18):3966, 2000.

[19] David R Smith, Willie J Padilla, DC Vier, Syrus C Nemat-Nasser, and Seldon Schultz. Composite medium with simultaneously negative permeability and permittivity. *Physical review letters*, 84(18):4184, 2000.

[20] Richard A Shelby, David R Smith, and Seldon Schultz. Experimental verification of a negative index of refraction. *science*, 292(5514):77–79, 2001.

[21] S Foteinopoulou. Photonic crystals as metamaterials. *Physica B: Condensed Matter*, 407(20):4056–4061, 2012.

[22] Andrea Alù, Alessandro Salandrino, and Nader Engheta. Negative effective permeability and left-handed materials at optical frequencies. *Optics express*, 14(4):1557–1567, 2006.

[23] Andrea Alù and Nader Engheta. Dynamical theory of artificial optical magnetism produced by rings of plasmonic nanoparticles. *Physical Review B*, 78(8):085112, 2008.

[24] Andrea Alu and Nader Engheta. The quest for magnetic plasmons at optical frequencies. *Optics express*, 17(7):5723–5730, 2009.

[25] G Dolling, C Enkrich, M Wegener, JF Zhou, Costas M Soukoulis, and S Linden. Cut-wire pairs and plate pairs as magnetic atoms for optical metamaterials. *Optics letters*, 30(23):3198–3200, 2005.

[26] Jiangfeng Zhou, Lei Zhang, Gary Tuttle, Thomas Koschny, and Costas M Soukoulis. Negative index materials using simple short wire pairs. *Physical Review B*, 73(4):041101, 2006.

[27] Nicholas Fang and Xiang Zhang. Imaging properties of a metamaterial superlens. In *Proceedings of the 2nd IEEE Conference on Nanotechnology*, pages 225–228. IEEE, 2002.

[28] Vladimir M Shalaev. Optical negative-index metamaterials. *Nature photonics*, 1(1):41, 2007.

[29] David Schurig, JJ Mock, BJ Justice, Steven A Cummer, John B Pendry, AF Starr, and DR Smith. Metamaterial electromagnetic cloak at microwave frequencies. *Science*, 314(5801):977–980, 2006.

[30] Hongsheng Chen, Bae-Ian Wu, Baile Zhang, and Jin Au Kong. Electromagnetic wave interactions with a metamaterial cloak. *Physical Review Letters*, 99(6):063903, 2007.

[31] Tao Chen, Suyan Li, and Hui Sun. Metamaterials application in sensing. *Sensors*, 12(3):2742–2765, 2012.

[32] Na Liu, Martin Mesch, Thomas Weiss, Mario Hentschel, and Harald Giessen. Infrared perfect absorber and its application as plasmonic sensor. *Nano letters*, 10(7):2342–2348, 2010.

[33] AV Kabashin, P Evans, S Pastkovsky, W Hendren, GA Wurtz, R Atkinson, R Pollard, VA Podolskiy, and AV Zayats. Plasmonic nanorod metamaterials for biosensing. *Nature materials*, 8(11):867, 2009.

[34] Michael Ricci, Nathan Orloff, and Steven M Anlage. Superconducting metamaterials. *Applied Physics Letters*, 87(3):034102, 2005.

[35] Steven M Anlage. The physics and applications of superconducting metamaterials. *Journal of Optics*, 13(2):024001, 2010.

[36] Jianqiang Gu, Ranjan Singh, Zhen Tian, Wei Cao, Qirong Xing, Mingxia He, Jingwen W Zhang,

Jiaguang Han, Hou-Tong Chen, and Weili Zhang. Terahertz superconductor metamaterial. *Applied Physics Letters*, 97(7):071102, 2010.

[37] Stefan A Maier and Harry A Atwater. Plasmonics: Localization and guiding of electromagnetic energy in metal/dielectric structures. *Journal of applied physics*, 98(1):10, 2005.

[38] JB Pendry, L Martin-Moreno, and FJ Garcia-Vidal. Mimicking surface plasmons with structured surfaces. *Science*, 305(5685):847–848, 2004.

[39] FJ Garcia-Vidal, L Martin-Moreno, and JB Pendry. Surfaces with holes in them: new plasmonic metamaterials. *Journal of optics A: Pure and applied optics*, 7(2):S97, 2005.

[40] Luis Martin-Moreno, FJ Garcia-Vidal, HJ Lezec, KM Pellerin, Tineke Thio, JB Pendry, and TW Ebbesen. Theory of extraordinary optical transmission through subwavelength hole arrays. *Physical review letters*, 86(6):1114, 2001.

[41] HF Ghaemi, Tineke Thio, DE e al Grupp, Thomas W Ebbesen, and HJ Lezec. Surface plasmons enhance optical transmission through subwavelength holes. *Physical review B*, 58(11):6779, 1998.

[42] Thomas W Ebbesen, Henri J Lezec, HF Ghaemi, Tineke Thio, and Peter A Wolff. Extraordinary optical transmission through sub-wavelength hole arrays. *Nature*, 391(6668):667, 1998.

[43] FF Lu, T Li, J Xu, ZD Xie, L Li, SN Zhu, and YY Zhu. Surface plasmon polariton enhanced by optical parametric amplification in nonlinear hybrid waveguide. *Optics express*, 19(4):2858–2865, 2011.

[44] Rupert F Oulton, Volker J Sorger, DA Genov, DFP Pile, and X Zhang. A hybrid plasmonic waveguide for subwavelength confinement and long-range propagation. *nature photonics*, 2(8):496, 2008.

[45] Yi Song, Jing Wang, Qiang Li, Min Yan, and Min Qiu. Broadband coupler between silicon waveguide and hybrid plasmonic waveguide. *Optics express*, 18(12):13173–13179, 2010.

[46] Maziar P Nezhad, Kevin Tetz, and Yeshaiahu Fainman. Gain assisted propagation of surface plasmon polaritons on planar metallic waveguides. *Optics Express*, 12(17):4072–4079, 2004.

[47] Tobias Holmgaard and Sergey I Bozhevolnyi. Theoretical analysis of dielectric-loaded surface plasmon-polariton waveguides. *Physical Review B*, 75(24):245405, 2007.

[48] JA Dionne, LA Sweatlock, HA Atwater, and A Polman. Planar metal plasmon waveguides: frequency-dependent dispersion, propagation, localization, and loss beyond the free electron model. *Physical Review B*, 72(7):075405, 2005.

[49] Jon A Schuller, Edward S Barnard, Wenshan Cai, Young Chul Jun, Justin S White, and Mark L Brongersma. Plasmonics for extreme light concentration and manipulation. *Nature materials*, 9(3):193, 2010.

[50] Martti Kauranen and Anatoly V Zayats. Nonlinear plasmonics. *Nature photonics*, 6(11):737, 2012.

[51] Monisha Kumar, K Porsezian, P Tchofo-Dinda, Ph Grelu, T Mithun, and T Uthayakumar. Spatial modulation instability of coupled surface plasmon polaritons in a dielectric–metal–dielectric structure. *JOSA B*, 34(1):198–206, 2017.

[52] Koijam Monika Devi, K Porsezian, and Amarendra K Sarma. Surface plasmon polariton akhmediev breather in a dielectric-metal-dielectric geometry with subwavelength thickness. *Superlattices and Microstructures*, 117:392–398, 2018.

[53] DA Korobko, SG Moiseev, and IO Zolotovskii. Induced modulation instability of surface plasmon

polaritons. *Optics letters*, 40(20):4619–4622, 2015.

[54] Eyal Feigenbaum and Meir Orenstein. Plasmon-soliton. *Optics letters*, 32(6):674–676, 2007.

[55] Arthur R Davoyan, Ilya V Shadrivov, and Yuri S Kivshar. Self-focusing and spatial plasmon-polariton solitons. *Optics express*, 17(24):21732–21737, 2009.

[56] Andrea Marini, Dmitry V Skryabin, and Boris Malomed. Stable spatial plasmon solitons in a dielectric-metal-dielectric geometry with gain and loss. *Optics express*, 19(7):6616–6622, 2011.

[57] Konstantin Y Bliokh, Yury P Bliokh, and Albert Ferrando. Resonant plasmon-soliton interaction. *Physical Review A*, 79(4):041803, 2009.

[58] Jennifer M Brockman, Bryce P Nelson, and Robert M Corn. Surface plasmon resonance imaging measurements of ultrathin organic films. *Annual review of physical chemistry*, 51(1):41–63, 2000.

[59] Benno Rothenhäusler and Wolfgang Knoll. Surface–plasmon microscopy. *Nature*, 332(6165):615, 1988.

[60] Satoshi Kawata, Yasushi Inouye, and Prabhat Verma. Plasmonics for near-field nano-imaging and superlensing. *Nature Photonics*, 3(7):388, 2009.

[61] Ting Xu, Yi-Kuei Wu, Xiangang Luo, and L Jay Guo. Plasmonic nanoresonators for high-resolution colour filtering and spectral imaging. *Nature communications*, 1:59, 2010.

[62] Jeffrey N Anker, W Paige Hall, Olga Lyandres, Nilam C Shah, Jing Zhao, and Richard P Van Duyne. Biosensing with plasmonic nanosensors. In *Nanoscience And Technology: A Collection of Reviews from Nature Journals*, pages 308–319. World Scientific, 2010.

[63] Xuyen D Hoa, AG Kirk, and M Tabrizian. Towards integrated and sensitive surface plasmon resonance biosensors: a review of recent progress. *Biosensors and bioelectronics*, 23(2):151–160, 2007.

[64] Junxi Zhang, Lide Zhang, and Wei Xu. Surface plasmon polaritons: physics and applications. *Journal of Physics D: Applied Physics*, 45(11):113001, 2012.

[65] KR Catchpole and A Polman. Design principles for particle plasmon enhanced solar cells. *Applied Physics Letters*, 93(19):191113, 2008.

[66] FJ Beck, A Polman, and KR Catchpole. Tunable light trapping for solar cells using localized surface plasmons. *Journal of Applied Physics*, 105(11):114310, 2009.

[67] Vivian E Ferry, Luke A Sweatlock, Domenico Pacifici, and Harry A Atwater. Plasmonic nanostructure design for efficient light coupling into solar cells. *Nano letters*, 8(12):4391–4397, 2008.

[68] KR Catchpole, , and Albert Polman. Plasmonic solar cells. *Optics express*, 16(26):21793–21800, 2008.

[69] Pierre Berini and Israel De Leon. Surface plasmon–polariton amplifiers and lasers. *Nature photonics*, 6(1):16, 2012.

[70] Alessandro Tredicucci, Claire Gmachl, Federico Capasso, Albert L Hutchinson, Deborah L Sivco, and Alfred Y Cho. Single-mode surface-plasmon laser. *Applied physics letters*, 76(16):2164–2166, 2000.

[71] Martin T Hill, Milan Marell, Eunice SP Leong, Barry Smalbrugge, Youcai Zhu, Minghua Sun, Peter J Van Veldhoven, Erik Jan Geluk, Fouad Karouta, Yok-Siang Oei, et al. Lasing in metal-insulator-metal sub-wavelength plasmonic waveguides. *Optics express*, 17(13):11107–11112, 2009.

[72] Frerik van Beijnum, Peter J van Veldhoven, Erik Jan Geluk, Michiel JA de Dood, W Gert, and Martin P van Exter. Surface plasmon lasing observed in metal hole arrays. *Physical review letters*, 110(20):206802, 2013.

[73] Shuang Zhang, Dentcho A Genov, Yuan Wang, Ming Liu, and Xiang Zhang. Plasmon-induced transparency in metamaterials. *Physical review letters*, 101(4):047401, 2008.

[74] Nikitas Papasimakis, Vassili A Fedotov, NI Zheludev, and SL Prosvirnin. Metamaterial analog of electromagnetically induced transparency. *Physical Review Letters*, 101(25):253903, 2008.

[75] Michael Fleischhauer, Atac Imamoglu, and Jonathan P Marangos. Electromagnetically induced transparency: Optics in coherent media. *Reviews of modern physics*, 77(2):633, 2005.

[76] Chunguang Du. Quantum surface plasmon resonance system based on electromagnetically induced transparency. *Applied Physics A*, 109(4):797–803, 2012.

[77] Jian Qi Shen. Electromagnetically-induced-transparency plasmonics: Quantum-interference-assisted tunable surface-plasmon-polariton resonance and excitation. *Physical Review A*, 90(2):023814, 2014.

[78] Chunguang Du, Qingli Jing, and Zhengfeng Hu. Coupler-free transition from light to surface plasmon polariton. *Physical Review A*, 91(1):013817, 2015.

[79] Stephen E Harris, JE Field, and A Imamoğlu. Nonlinear optical processes using electromagnetically induced transparency. *Physical Review Letters*, 64(10):1107, 1990.

[80] K-J Boller, A Imamoğlu, and Stephen E Harris. Observation of electromagnetically induced transparency. *Physical Review Letters*, 66(20):2593, 1991.

[81] JE Field, KH Hahn, and SE Harris. Observation of electromagnetically induced transparency in collisionally broadened lead vapor. *Physical review letters*, 67(22):3062, 1991.

[82] Min Xiao, Yong-qing Li, Shao-zheng Jin, and Julio Gea-Banacloche. Measurement of dispersive properties of electromagnetically induced transparency in rubidium atoms. *Physical Review Letters*, 74(5):666, 1995.

[83] S Baluschev, Norbert Leinfellner, EA Korsunsky, and Laurentius Windholz. Electromagnetically induced transparency in a sodium vapour cell. *The European Physical Journal D-Atomic, Molecular, Optical and Plasma Physics*, 2(1):5–10, 1998.

[84] H Schmidt and A Imamoglu. Giant kerr nonlinearities obtained by electromagnetically induced transparency. *Optics letters*, 21(23):1936–1938, 1996.

[85] Yong-qing Li and Min Xiao. Enhancement of nondegenerate four-wave mixing based on electromagnetically induced transparency in rubidium atoms. *Optics letters*, 21(14):1064–1066, 1996.

[86] Ying Wu, Joseph Saldana, and Yifu Zhu. Large enhancement of four-wave mixing by suppression of photon absorption from electromagnetically induced transparency. *Physical Review A*, 67(1):013811, 2003.

[87] Danielle A Braje, Vlatko Balić, Sunil Goda, GY Yin, and SE Harris. Frequency mixing using electromagnetically induced transparency in cold atoms. *Physical review letters*, 93(18):183601, 2004.

[88] MD Lukin and Ataç Imamoğlu. Controlling photons using electromagnetically induced transparency. *Nature*, 413(6853):273, 2001.

[89] DF Phillips, A Fleischhauer, A Mair, RL Walsworth, and Mikhail D Lukin. Storage of light in atomic vapor. *Physical Review Letters*, 86(5):783, 2001.

[90] Jonathan P Marangos. Electromagnetically induced transparency. *Journal of Modern Optics*, 45(3):471–503, 1998.

[91] D Budker, DF Kimball, SM Rochester, and VV Yashchuk. Nonlinear magneto-optics and reduced group velocity of light in atomic vapor with slow ground state relaxation. *Physical review letters*, 83(9):1767, 1999.

[92] Edward S Fry, Xingfu Li, Dmitri Nikonov, GG Padmabandu, Marlan O Scully, Arlie V Smith, Frank K Tittel, Ching Wang, Steve R Wilkinson, and Shi-Yao Zhu. Atomic coherence effects within the sodium d 1 line: lasing without inversion via population trapping. *Physical review letters*, 70(21):3235, 1993.

[93] Marlan O Scully, Shi-Yao Zhu, and Athanasios Gavrielides. Degenerate quantum-beat laser: Lasing without inversion and inversion without lasing. *Physical review letters*, 62(24):2813, 1989.

[94] Manukumara Manjappa, Sher-Yi Chiam, Longqing Cong, Andrew A Bettiol, Weili Zhang, and Ranjan Singh. Tailoring the slow light behavior in terahertz metasurfaces. *Applied Physics Letters*, 106(18):181101, 2015.

[95] Saeed Asgarnezhad-Zorgabad, Rasoul Sadighi-Bonabi, and Chao Hang. Coupler-free surface polariton excitation and propagation with cold four-level atomic medium. *JOSA B*, 34(9):1787–1795, 2017.

[96] Saeid Asgarnezhad-Zorgabad, Rasoul Sadighi-Bonabi, and Barry C Sanders. Excitation and propagation of surface polaritonic rogue waves and breathers. *Physical Review A*, 98(1):013825, 2018.

[97] Zhengyang Bai, Guoxiang Huang, Lixiang Liu, and Shuang Zhang. Giant kerr nonlinearity and low-power gigahertz solitons via plasmon-induced transparency. *Scientific reports*, 5:13780, 2015.

[98] Zhengyang Bai and Guoxiang Huang. Plasmon dromions in a metamaterial via plasmon-induced transparency. *Physical Review A*, 93(1):013818, 2016.

[99] Jianqiang Gu, Ranjan Singh, Xiaojun Liu, Xueqian Zhang, Yingfang Ma, Shuang Zhang, Stefan A Maier, Zhen Tian, Abul K Azad, Hou-Tong Chen, et al. Active control of electromagnetically induced transparency analogue in terahertz metamaterials. *Nature communications*, 3:1151, 2012.

[100] Xing Ri Jin, Ying Qiao Zhang, Shou Zhang, YoungPak Lee, and Joo Yull Rhee. Polarization-independent electromagnetically induced transparency-like effects in stacked metamaterials based on fabry–perot resonance. *Journal of Optics*, 15(12):125104, 2013.

[101] Xueqian Zhang, Quan Li, Wei Cao, Jianqiang Gu, Ranjan Singh, Zhen Tian, Jiaguang Han, and Weili Zhang. Polarization-independent plasmon-induced transparency in a fourfold symmetric terahertz metamaterial. *IEEE Journal of Selected Topics in Quantum Electronics*, 19(1):8400707–8400707, 2013.

[102] Sang-Eun Mun, Kyookeun Lee, Hansik Yun, and Byoungho Lee. Polarization-independent plasmon-induced transparency in a symmetric metamaterial. *IEEE Photonics Technology Letters*, 28(22):2581–2584, 2016.

[103] Zhihua Zhu, Xu Yang, Jianqiang Gu, Jun Jiang, Weisheng Yue, Zhen Tian, Masayoshi Tonouchi, Jiaguang Han, and Weili Zhang. Broadband plasmon induced transparency in terahertz metamate-

rials. *Nanotechnology*, 24(21):214003, 2013.

[104] Mingli Wan, Yueli Song, Liufang Zhang, and Fengqun Zhou. Broadband plasmon-induced transparency in terahertz metamaterials via constructive interference of electric and magnetic couplings. *Optics express*, 23(21):27361–27368, 2015.

[105] Hua Cheng, Shuqi Chen, Ping Yu, Xiaoyang Duan, Boyang Xie, and Jianguo Tian. Dynamically tunable plasmonically induced transparency in periodically patterned graphene nanostrips. *Applied Physics Letters*, 103(20):203112, 2013.

[106] Prakash Pitchappa, Manukumara Manjappa, Chong Pei Ho, Ranjan Singh, Navab Singh, and Chengkuo Lee. Active control of electromagnetically induced transparency with dual dark mode excitation pathways using mems based tri-atomic metamolecules. *Applied Physics Letters*, 109(21):211103, 2016.

[107] Guang-Lai Fu, Xiang Zhai, Hong-Ju Li, Sheng-Xuan Xia, and Ling-Ling Wang. Dynamically tunable plasmon induced transparency in graphene metamaterials. *Journal of Optics*, 19(1):015001, 2016.

[108] Xiaoyang Duan, Shuqi Chen, Hua Cheng, Zhancheng Li, and Jianguo Tian. Dynamically tunable plasmonically induced transparency by planar hybrid metamaterial. *Optics letters*, 38(4):483–485, 2013.

[109] Vassilios Yannopapas, Emmanuel Paspalakis, and Nikolay V Vitanov. Electromagnetically induced transparency and slow light in an array of metallic nanoparticles. *Physical Review B*, 80(3):035104, 2009.

[110] Philippe Tassin, Lei Zhang, Th Koschny, EN Economou, and Costas M Soukoulis. Low-loss metamaterials based on classical electromagnetically induced transparency. *Physical review letters*, 102(5):053901, 2009.

[111] Zheng-Gao Dong, Hui Liu, Jing-Xiao Cao, Tao Li, Shu-Ming Wang, Shi-Ning Zhu, and Xiang Zhang. Enhanced sensing performance by the plasmonic analog of electromagnetically induced transparency in active metamaterials. *Applied Physics Letters*, 97(11):114101, 2010.

[112] BX Li, HJ Li, LL Zeng, SP Zhan, ZH He, ZQ Chen, and H Xu. High-sensitivity sensing based on plasmon-induced transparency. *IEEE Photonics Journal*, 7(5):1–7, 2015.

[113] Na Liu, Thomas Weiss, Martin Mesch, Lutz Langguth, Ulrike Eigenthaler, Michael Hirscher, Carsten Sonnichsen, and Harald Giessen. Planar metamaterial analogue of electromagnetically induced transparency for plasmonic sensing. *Nano letters*, 10(4):1103–1107, 2009.

[114] Kun Zhang, Cheng Wang, Ling Qin, Ru-Wen Peng, Di-Hu Xu, Xiang Xiong, and Mu Wang. Dual-mode electromagnetically induced transparency and slow light in a terahertz metamaterial. *Optics letters*, 39(12):3539–3542, 2014.

[115] Ningning Xu, Manukumara Manjappa, Ranjan Singh, and Weili Zhang. Tailoring the electromagnetically induced transparency and absorbance in coupled fano–lorentzian metasurfaces: A classical analog of a four-level tripod quantum system. *Advanced Optical Materials*, 4(8):1179–1185, 2016.

[116] PW Milonni and JH Eberly. Laser resonators and gaussian beams. *Laser Physics, 1st ed.; John Wiley and Sons, Inc.: Hoboken, NJ, USA*, 2010.

[117] Xi-Cheng Zhang and Jingzhou Xu. *Introduction to THz wave photonics*, volume 29. Springer, 2010.

[118] Michael C Kemp, PF Taday, Bryan E Cole, JA Cluff, Anthony J Fitzgerald, and William R Tribe.

Security applications of terahertz technology. In *Terahertz for Military and Security Applications*, volume 5070, pages 44–53. International Society for Optics and Photonics, 2003.

[119] Masayoshi Tonouchi. Cutting-edge terahertz technology. *Nature photonics*, 1(2):97, 2007.

[120] William R Tribe, David A Newnham, Philip F Taday, and Michael C Kemp. Hidden object detection: security applications of terahertz technology. In *Terahertz and Gigahertz Electronics and Photonics III*, volume 5354, pages 168–177. International Society for Optics and Photonics, 2004.

[121] DM Mittleman, M Gupta, Ramesh Neelamani, RG Baraniuk, JV Rudd, and M Koch. Recent advances in terahertz imaging. *Applied Physics B*, 68(6):1085–1094, 1999.

[122] John F Federici, Brian Schulkin, Feng Huang, Dale Gary, Robert Barat, Filipe Oliveira, and David Zimdars. Thz imaging and sensing for security applications—explosives, weapons and drugs. *Semiconductor Science and Technology*, 20(7):S266, 2005.

[123] Wai Lam Chan, Jason Deibel, and Daniel M Mittleman. Imaging with terahertz radiation. *Reports on progress in physics*, 70(8):1325, 2007.

[124] Binbin B Hu and Martin C Nuss. Imaging with terahertz waves. *Optics letters*, 20(16):1716–1718, 1995.

[125] Peter H Siegel. Terahertz technology in biology and medicine. *IEEE transactions on microwave theory and techniques*, 52(10):2438–2447, 2004.

[126] Calvin Yu, Shuting Fan, Yiwen Sun, and Emma Pickwell-MacPherson. The potential of terahertz imaging for cancer diagnosis: A review of investigations to date. *Quantitative imaging in medicine and surgery*, 2(1):33, 2012.

[127] Daniel Mittleman. *Sensing with terahertz radiation*, volume 85. Springer, 2013.

[128] M Nagel, M Först, and H Kurz. Thz biosensing devices: fundamentals and technology. *Journal of Physics: Condensed Matter*, 18(18):S601, 2006.

[129] Wenshan Cai, Uday K Chettiar, Alexander V Kildishev, and Vladimir M Shalaev. Optical cloaking with metamaterials. *Nature photonics*, 1(4):224, 2007.

[130] Francesco Monticone and Andrea Alù. The quest for optical magnetism: from split-ring resonators to plasmonic nanoparticles and nanoclusters. *Journal of Materials Chemistry C*, 2(43):9059–9072, 2014.

[131] Ta-Jen Yen, WJ Padilla, Nicholas Fang, DC Vier, DR Smith, JB Pendry, DN Basov, and Xiang Zhang. Terahertz magnetic response from artificial materials. *Science*, 303(5663):1494–1496, 2004.

[132] Nikolay I Zheludev and Yuri S Kivshar. From metamaterials to metadevices. *Nature materials*, 11(11):917, 2012.

[133] Hou-Tong Chen, John F O'hara, Abul K Azad, Antoinette J Taylor, Richard D Averitt, David B Shrekenhamer, and Willie J Padilla. Experimental demonstration of frequency-agile terahertz metamaterials. *Nature Photonics*, 2(5):295, 2008.

[134] Hou-Tong Chen, Willie J Padilla, Joshua MO Zide, Arthur C Gossard, Antoinette J Taylor, and Richard D Averitt. Active terahertz metamaterial devices. *Nature*, 444(7119):597, 2006.

[135] Hu Tao, Nathan I Landy, Christopher M Bingham, Xin Zhang, Richard D Averitt, and Willie J Padilla. A metamaterial absorber for the terahertz regime: design, fabrication and characterization. *Optics express*, 16(10):7181–7188, 2008.

[136] Nathaniel K Grady, Jane E Heyes, Dibakar Roy Chowdhury, Yong Zeng, Matthew T Reiten, Abul K Azad, Antoinette J Taylor, Diego AR Dalvit, and Hou-Tong Chen. Terahertz metamaterials for linear polarization conversion and anomalous refraction. *Science*, 340(6138):1304–1307, 2013.

[137] Dibakar Roy Chowdhury, Ranjan Singh, Antoinette J Taylor, Hou-Tong Chen, and Abul K Azad. Ultrafast manipulation of near field coupling between bright and dark modes in terahertz metamaterial. *Applied Physics Letters*, 102(1):011122, 2013.

[138] Dibakar Roy Chowdhury, Xiaofang Su, Yong Zeng, Xiaoshuang Chen, Antoinette J Taylor, and Abul Azad. Excitation of dark plasmonic modes in symmetry broken terahertz metamaterials. *Optics express*, 22(16):19401–19410, 2014.

[139] Ranjan Singh, Carsten Rockstuhl, Falk Lederer, and Weili Zhang. Coupling between a dark and a bright eigenmode in a terahertz metamaterial. *Physical Review B*, 79(8):085111, 2009.

[140] Sher-Yi Chiam, Ranjan Singh, Carsten Rockstuhl, Falk Lederer, Weili Zhang, and Andrew A Bettiol. Analogue of electromagnetically induced transparency in a terahertz metamaterial. *Physical Review B*, 80(15):153103, 2009.

[141] Xiaojun Liu, Jianqiang Gu, Ranjan Singh, Yingfang Ma, Jun Zhu, Zhen Tian, Mingxia He, Jiaguang Han, and Weili Zhang. Electromagnetically induced transparency in terahertz plasmonic metamaterials via dual excitation pathways of the dark mode. *Applied Physics Letters*, 100(13):131101, 2012.

[142] Mohammad Parvinnezhad Hokmabadi, Elizabath Philip, Elmer Rivera, Patrick Kung, and Seongsin M Kim. Plasmon-induced transparency by hybridizing concentric-twisted double split ring resonators. *Scientific reports*, 5:15735, 2015.

[143] Philippe Tassin, Lei Zhang, Thomas Koschny, EN Economou, and Costas M Soukoulis. Planar designs for electromagnetically induced transparency in metamaterials. *Optics express*, 17(7):5595–2605, 2009.

[144] CL Garrido Alzar, MAG Martinez, and P Nussenzveig. Classical analog of electromagnetically induced transparency. *American Journal of Physics*, 70(1):37–41, 2002.

[145] Xi Shi, Xiaopeng Su, and Yaping Yang. Enhanced tunability of plasmon induced transparency in graphene strips. *Journal of Applied Physics*, 117(14):143101, 2015.

[146] Xi Shi, Dezhuan Han, Yunyun Dai, Zongfu Yu, Yong Sun, Hong Chen, Xiaohan Liu, and Jian Zi. Plasmonic analog of electromagnetically induced transparency in nanostructure graphene. *Optics express*, 21(23):28438–28443, 2013.

[147] Xiaolei Zhao, Cai Yuan, Wenhua Lv, Shilin Xu, and Jianquan Yao. Plasmon-induced transparency in metamaterial based on graphene and split-ring resonators. *IEEE Photonics Technology Letters*, 27(12):1321–1324, 2015.

[148] Zhengren Zhang, Liwei Zhang, Hongqiang Li, and Hong Chen. Plasmon induced transparency in a surface plasmon polariton waveguide with a comb line slot and rectangle cavity. *Applied Physics Letters*, 104(23):231114, 2014.

[149] Xiong-jun Shang, Xiang Zhai, Xiao-fei Li, Ling-ling Wang, Ben-xin Wang, and Gui-dong Liu. Realization of graphene-based tunable plasmon-induced transparency by the dipole-dipole coupling. *Plasmonics*, 11(2):419–423, 2016.

[150] Gang Yao, Furi Ling, Jin Yue, Qin Luo, and Jianquan Yao. Dynamically tunable graphene plasmon-induced transparency in the terahertz region. *Journal of Lightwave Technology*, 34(16):3937–3942, 2016.

[151] S Izadshenas, A Zakery, and Z Vafapour. Tunable slow light in graphene metamaterial in a broad terahertz range. *Plasmonics*, 13(1):63–70, 2018.

[152] Huiyun Zhang, Yanyan Cao, Yuanzhong Liu, Yue Li, and Yuping Zhang. A novel graphene metamaterial design for tunable terahertz plasmon induced transparency by two bright mode coupling. *Optics Communications*, 391:9–15, 2017.

[153] Chen Sun, Zhewei Dong, Jiangnan Si, and Xiaoxu Deng. Independently tunable dual-band plasmonically induced transparency based on hybrid metal-graphene metamaterials at mid-infrared frequencies. *Optics express*, 25(2):1242–1250, 2017.

[154] Xun-jun He, Jian-min Wang, Xiao-hua Tian, Jiu-xing Jiang, and Zhao-xin Geng. Dual-spectral plasmon electromagnetically induced transparency in planar metamaterials based on bright–dark coupling. *Optics Communications*, 291:371–375, 2013.

[155] Sen Hu, Helin Yang, Song Han, Xiaojun Huang, and Boxun Xiao. Tailoring dual-band electromagnetically induced transparency in planar metamaterials. *Journal of Applied Physics*, 117(4):043107, 2015.

[156] Junqiao Wang, Baohe Yuan, Chunzhen Fan, Jinna He, Pei Ding, Qianzhong Xue, and Erjun Liang. A novel planar metamaterial design for electromagnetically induced transparency and slow light. *Optics Express*, 21(21):25159–25166, 2013.

[157] Qiang Bai, Cong Liu, Jing Chen, Chen Cheng, Ming Kang, and Hui-Tian Wang. Tunable slow light in semiconductor metamaterial in a broad terahertz regime. *Journal of Applied Physics*, 107(9):093104, 2010.

[158] Guoxi Wang, Wenfu Zhang, Yongkang Gong, and Jian Liang. Tunable slow light based on plasmon-induced transparency in dual-stub-coupled waveguide. *IEEE Photonics Technology Letters*, 27(1):89–92, 2015.

[159] Quan Xu, Xiaoqiang Su, Chunmei Ouyang, Ningning Xu, Wei Cao, Yuping Zhang, Quan Li, Cong Hu, Jianqiang Gu, Zhen Tian, et al. Frequency-agile electromagnetically induced transparency analogue in terahertz metamaterials. *Optics letters*, 41(19):4562–4565, 2016.

[160] Andreas Otto. Excitation of nonradiative surface plasma waves in silver by the method of frustrated total reflection. *Zeitschrift für Physik A Hadrons and nuclei*, 216(4):398–410, 1968.

[161] Herman L Offerhaus, B Van Den Bergen, M Escalante, Franciscus B Segerink, Jeroen P Korterik, and NF Van Hulst. Creating focused plasmons by noncollinear phasematching on functional gratings. *Nano letters*, 5(11):2144–2148, 2005.

[162] Arif E Çetin, Alp Artar, Mustafa Turkmen, Ahmet Ali Yanik, and Hatice Altug. Plasmon induced transparency in cascaded π-shaped metamaterials. *Optics express*, 19(23):22607–22618, 2011.

[163] Jianjun Chen, Zhi Li, Song Yue, Jinghua Xiao, and Qihuang Gong. Plasmon-induced transparency in asymmetric t-shape single slit. *Nano letters*, 12(5):2494–2498, 2012.

[164] Yu Zhu, Xiaoyong Hu, Hong Yang, and Qihuang Gong. On-chip plasmon-induced transparency based on plasmonic coupled nanocavities. *Scientific reports*, 4:3752, 2014.

[165] Zhongyang Li, Yingfang Ma, Ran Huang, Ranjan Singh, Jianqiang Gu, Zhen Tian, Jiaguang Han, and Weili Zhang. Manipulating the plasmon-induced transparency in terahertz metamaterials. *Optics express*, 19(9):8912–8919, 2011.

[166] Na Liu, Lutz Langguth, Thomas Weiss, Jürgen Kästel, Michael Fleischhauer, Tilman Pfau, and Harald Giessen. Plasmonic analogue of electromagnetically induced transparency at the drude damping limit. *Nature materials*, 8(9):758, 2009.

[167] Longqing Cong, Manukumara Manjappa, Ningning Xu, Ibraheem Al-Naib, Weili Zhang, and Ranjan Singh. Fano resonances in terahertz metasurfaces: a figure of merit optimization. *Advanced Optical Materials*, 3(11):1537–1543, 2015.

[168] Yang Bai, Kejian Chen, Hong Liu, Ting Bu, Bin Cai, Jian Xu, and Yiming Zhu. Optically controllable terahertz modulator based on electromagnetically-induced-transparency-like effect. *Optics Communications*, 353:83–89, 2015.

[169] Yuancheng Fan, Tong Qiao, Fuli Zhang, Quanhong Fu, Jiajia Dong, Botao Kong, and Hongqiang Li. An electromagnetic modulator based on electrically controllable metamaterial analogue to electromagnetically induced transparency. *Scientific reports*, 7:40441, 2017.

[170] Dean A Frickey. Conversions between s, z, y, h, abcd, and t parameters which are valid for complex source and load impedances. *IEEE Transactions on microwave theory and techniques*, 42(2):205–211, 1994.

[171] David M Pozar. *Microwave engineering*. John Wiley & Sons, 2009.

[172] Wei Cao, Ranjan Singh, Caihong Zhang, Jiaguang Han, Masayoshi Tonouchi, and Weili Zhang. Plasmon-induced transparency in metamaterials: Active near field coupling between bright superconducting and dark metallic mode resonators. *Applied Physics Letters*, 103(10):101106, 2013.

[173] F Javier Garcia de Abajo. Graphene plasmonics: challenges and opportunities. *Acs Photonics*, 1(3):135–152, 2014.

[174] Long Ju, Baisong Geng, Jason Horng, Caglar Girit, Michael Martin, Zhao Hao, Hans A Bechtel, Xiaogan Liang, Alex Zettl, Y Ron Shen, et al. Graphene plasmonics for tunable terahertz metamaterials. *Nature nanotechnology*, 6(10):630, 2011.

[175] Shenyang Huang, Chaoyu Song, Guowei Zhang, and Hugen Yan. Graphene plasmonics: physics and potential applications. *Nanophotonics*, 6(6):1191–1204, 2016.

[176] AN Grigorenko, Marco Polini, and KS Novoselov. Graphene plasmonics. *Nature photonics*, 6(11):749, 2012.

[177] Shuyuan Xiao, Tao Wang, Tingting Liu, Xicheng Yan, Zhong Li, and Chen Xu. Active modulation of electromagnetically induced transparency analogue in terahertz hybrid metal-graphene metamaterials. *Carbon*, 126:271–278, 2018.

[178] Xiaolei Zhao, Cai Yuan, Lin Zhu, and Jianquan Yao. Graphene-based tunable terahertz plasmon-induced transparency metamaterial. *Nanoscale*, 8(33):15273–15280, 2016.

[179] A Keshavarz and A Zakery. A novel terahertz semiconductor metamaterial for slow light device and dual-band modulator applications. *Plasmonics*, 13(2):459–466, 2018.

[180] Ranjan Singh, Ibraheem AI Al-Naib, Yuping Yang, Dibakar Roy Chowdhury, Wei Cao, Carsten Rockstuhl, Tsuneyuki Ozaki, Roberto Morandotti, and Weili Zhang. Observing metamaterial

induced transparency in individual fano resonators with broken symmetry. *Applied Physics Letters*, 99(20):201107, 2011.

[181] Philip G Drazin and Robin S Johnson. *Solitons: an introduction*, volume 2. Cambridge university press, 1989.

[182] AD Boardman, GS Cooper, AA Maradudin, and TP Shen. Surface-polariton solitons. *Physical review B*, 34(12):8273, 1986.

[183] Robert W Boyd. *Nonlinear optics*. Elsevier, 2003.

[184] Saeid Asgarnezhad-Zorgabad, Pierre Berini, and Barry C Sanders. Polaritonic frequency-comb generation and breather propagation in a negative-index metamaterial with a cold four-level atomic medium. *arXiv preprint arXiv:1902.04536*, 2019.

[185] Hai Wang, David Goorskey, and Min Xiao. Enhanced kerr nonlinearity via atomic coherence in a three-level atomic system. *Physical review letters*, 87(7):073601, 2001.

[186] Le Van Doai, Dinh Xuan Khoa, and Nguyen Huy Bang. Eit enhanced self-kerr nonlinearity in the three-level lambda system under doppler broadening. *Physica Scripta*, 90(4):045502, 2015.

[187] Daniel A Steck. Sodium d line data. *Report, Los Alamos National Laboratory, Los Alamos*, 124:74, 2000.

[188] Edward D Palik. *Handbook of optical constants of solids*, volume 3. Academic press, 1998.

[189] Guoxiang Huang, Lu Deng, and MG Payne. Dynamics of ultraslow optical solitons in a cold three-state atomic system. *Physical Review E*, 72(1):016617, 2005.

CONFERENCES/SCHOOLS ATTENDED

- **[Poster presentation]** *XXVII IUPAP Conference on Computational Physics*, Dec. 2-5, 2015, IIT Guwahati. Topic: Enhanced terahertz transmission through a periodic array of tapered rectangular apertures.

- **[Participation]** *South Asian Workshop on Optics Photonics, 'SAWOP-2015'*, 17-18 November, 2015, IIT Guwahati, India.

- **[Participation]** *TEQIP symposium on International Year of Light and Light based Technologies*, 31 October, 2015, IIT Guwahati, India.

- **[Poster presentation]** *International Conference on Fiber Optics and Photonics*, Dec. 04-08, 2016. IIT Kanpur, India. Topic: Surface Plasmon Polariton Akhmediev Breather in a dielectric-metal-dielectric multilayer structure.

- **[Attended]** *DST-SERB School on Frontiers in Quantum Optics*, 1-19 December, 2017, IIT Guwahati, India.

- **[Poster presentation]** *Workshop on Recent Trends on Photonics (WRAP)* at MEC, 20-22 December, 2017, Hyderabad, India. Topic: Exploring Plasmon Induced Transparency in Graphene Based Terahertz Metamaterials.

- **[Poster presentation]** *Research Conclave*, 2018, IIT Guwahati, India. Topic: Plasmon induced transparency in terahertz metamaterials.

- **[Poster presentation]** *International Conference on Fiber Optics and Photonics*, Dec. 12-15, 2018. IIT Delhi, India. Topic: Modulating dual-band electromagnetically induced transparency in terahertz metamaterials.

BIODATA

Personal Details

NAME	Koijam Monika Devi
DOB	2nd April, 1989
EMAIL	koijam@iitg.ac.in, koijam.iitg@gmail.com

Education

2010 - 2012	**Masters of Sience**, University of Hyderabad, (CGPA: 7.3/10)
2007 - 2010	**Bachelor of Science**, St. Anns' Degree College for Women *Percentage:* 78%
2007	**12th standard**, Tamphasana Girls' Higher Secondary School *Percentage:* 65%
2005	**10th standard**, Ibotonsana Girls' Higher Secondary School *Percentage:* 68%

National Exams Qualified

2014	GATE PHYSICS **AIR-319**
2014	JEST **AIR-509**

Teaching Experience

2014 - 2018	**Teaching assistant** for General Physics and Advanced Physics Lab for B.Tech and M.Sc. students in IIT Guwahati.

Others

At present	**Member**: SPIE, IEEE Student Chapter IIT Guwahati
2017	**Secretary**: SPIE Student Chapter IIT Guwahati